TRIBHUVAN UNIVERSITY
INSTITUTE OF ENGINEERING
PULCHOWK CAMPUS
Lalitpur, Nepal

THESIS NO: PUL/079/MSPDE/001

DESIGN AND CONTROL OF SOLAR POWERED BRUSHLESS DC MOTOR DRIVE FOR LIGHT ELECTRIC VEHICLES

by

Aashish Acharya

A Thesis
Submitted to the Department of Electrical Engineering
in Partial Fulfilment of the Requirements for the Degree of
Master of Science in Power Electronics and Drives Engineering

DEPARTMENT OF ELECTRICAL ENGINEERING

April, 2025

COPYRIGHT©

Head
Department of Electrical Engineering
Pulchowk Campus, Institute of Engineering, Tribhuvan University
Lalitpur, Nepal

DECLARATION

I hereby declare that this thesis entitled **“Design and Control of Solar Powered Brushless DC Motor Drive for Light Electric Vehicles”** is based on my original research work. Related works on the topic by other researchers have been duly acknowledged. I owe all the liabilities relating to the accuracy and authenticity of the data and any other information included hereunder.

Aashish Acharya (PUL079MSPDE001)
Date: 20th April, 2025

त्रिभुवन विश्वविद्यालय
TRIBHUVAN UNIVERSITY
इन्जिनियरिङ्ग अध्ययन संस्थान
INSTITUTE OF ENGINEERING
पुल्चोक क्याम्पस
PULCHOWK CAMPUS
DEPARTMENT OF ELECTRICAL ENGINEERING
Pulchowk, Lalitpur

Accredited by University Grants Commission (UGC) Nepal 2020

RECOMMENDATION

The undersigned certify that they have read and recommended to the **Department of Electrical Engineering, Pulchowk Campus, Institute of Engineering, Tribhuvan University, Lalitpur, Nepal** for acceptance, a dissertation entitled "**Design and Control of Solar Powered Brushless DC Motor Drive for Light Electric Vehicles**", submitted by **Aashish Acharya** in partial fulfilment of the requirements for the degree of **Master of Science in Power Electronics and Drives Engineering**.

……………………………
Supervisor
Jeetendra Chaudhary
Associate Professor
Pulchowk Campus, IOE, TU
Lalitpur, Nepal

……………………………
Co-Supervisor
Dr. Devara Vijaya Bhaskar
Associate Professor
IIT (ISM) Dhanbad
Jharkhand, India

……………………………
External Examiner
Lalit Bikram Rana
Associate Professor
School of Engineering, PoU
Pokhara, Nepal

Date of Recommendation: 2025/04/20

Accredited by University Grants
Commission (UGC) Nepal 2020

त्रिभुवन विश्वविद्यालय
TRIBHUVAN UNIVERSITY
इन्जिनियरिङ्ग अध्ययन संस्थान
INSTITUTE OF ENGINEERING
पुल्चोक क्याम्पस
PULCHOWK CAMPUS
DEPARTMENT OF ELECTRICAL ENGINEERING
Pulchowk, Lalitpur

APPROVAL

The thesis entitled “**Design and Control of Solar Powered Brushless DC Motor Drive for Light Electric Vehicles**” submitted by **Aashish Acharya** in partial fulfilment of the requirements for the degree of **Master of Science in Power Electronics and Drives Engineering** has been approved as a bona fide record of work independently carried out by him in the department.

Basanta Gautam
....

Assoc. Prof. Dr. Basanta Kumar Gautam
Head
Department of Electrical Engineering
Pulchowk Campus, Institute of Engineering, Tribhuvan University
Lalitpur, Nepal

Date of Approval: 2025/04/20

ACKNOWLEDGEMENT

First and foremost, I would like to extend my sincere thanks to my supervisor Jeetendra Chaudhary, associate professor at Pulchowk Campus, for his valuable guidance and encouragement to complete this project. My special thanks go to my co-supervisor Dr. Devara Vijaya Bhaskar, associate professor at IIT (ISM) Dhanbad, who continuously guided me with constructive suggestions and feedback throughout my research work. I am also highly indebted to all the members associated with the respective colleges' electrical departments and my colleagues who constantly motivated and supported me throughout the project. Without their cooperation, this thesis would not have been possible. Thank you for your encouragement, support, and belief in my abilities.

Aashish Acharya (PUL079MSPDE001)

ABSTRACT

This thesis presents the design architecture and control methods of an energy-efficient solar-powered brushless DC motor drive, focussing on its application in low-power electric vehicles. The motor is primarily driven by a battery in conjunction with a solar photovoltaic array that serves as the secondary source of power. For the extraction of optimal solar power, a perturb and observe maximum power point tracking algorithm using virtual resistance as a control parameter is used. This allows for better adaptation to the dynamic conditions and suppresses the frequent power oscillations observed in power point tracking. The other aim of this research is to propose and realise a position sensorless speed control technique for the brushless DC motor based on zero-crossing detection of motor back-electromotive forces. The stabilisation and control of the DC link voltage is achieved through a closed-loop speed controller and a closed-loop voltage controller acting together. Simulations are performed in MATLAB Simulink environment to validate the proposal under diverse circumstances, and the results obtained are examined to justify the effectiveness of the overall system model. The key contribution of this research is to reduce redundancy in the design of the motor drive, thereby improving the reliability of its commutation system by replacing the physical position sensors with virtual ones. The other importance of the work lies in contributing to saving energy bills through optimal use of available solar power applying the proposed maximum power point tracking algorithm.

Keywords:- Brushless DC Machine, Solar Photovoltaic Array, Maximum Power Point Tracking, Perturb and Observe Algorithm, Back Electromotive Force, Sensorless Control, Zero Crossing Points

CONTENTS

LIST OF FIGURES

LIST OF TABLES

LIST OF ACRONYMS

ANN artificial neural network. 22, 25

BEMF back-electromotive force. 26–28, 30, 45, 46, 49, 50, 67, 72

BLDC brushless DC. 15–20, 25, 29, 30, 45, 50, 54, 58, 62, 72

DoD depth of discharge. 31, 42

EKF extended Kalman filter. 27

EV electric vehicle. 14, 16, 17, 20, 23, 73

FLC fuzzy logic controller. 22, 25

GA genetic algorithm. 23, 25

IGBT insulated gate bipolar transistor. 29, 38, 42, 44, 45

IncCond incremental conductance. 22, 25

LPEV low-power electric vehicle. 14–19

MISO multiple input single output. 29, 34

MPP maximum power point. 21–24, 38–41, 55, 59, 69, 71

MPPT maximum power point tracking. 21–24, 29, 34, 41, 55, 59, 61, 69, 72

P&O perturb and observe. 21, 23–25, 39, 40, 55, 72

PI proportional integral. 43, 51, 55, 58, 72

PMSM permanent magnet synchronous machine. 15

PSO particle swarm optimization. 23, 25

PWM pulse width modulation. 28, 43–45, 55, 57

SoC state of charge. 42–44, 55, 66, 68, 69

SPV solar photovoltaic. 16–19, 24, 29, 33–36, 39, 42, 54, 55, 59, 60, 65, 68–70

VA Volt-Ampere. 38

VOR virtual optimal resistance. 23, 24, 39, 40, 55

VSI voltage source inverter. 19, 29–31, 38, 54

ZCP zero-crossing point. 26, 28, 30, 57, 64, 72

LIST OF UNITS

A	Ampere. 31, 33, 34, 36, 38, 63
Ah	Ampere-hour. 32
Nm	Newton-meter. 30
Nms/rad	Newton-meter-second per radian. 30
V	Volt. 29–38, 43, 56, 69
Vs/rad	Volt-second per radian. 30
Wm^{-2}	Watt per square meter. 22, 33, 55, 59, 60
Ω	Ohm. 30
μF	microFarad. 37, 38
$^{\circ}$	degree. 45, 46, 63, 64, 66
$^{\circ}C$	degree Celsius. 22, 31, 33, 55, 59, 60
kHz	kiloHertz. 35, 36
kVA	kiloVolt-Ampere. 38
kW	kiloWatt. 29–31, 33
kWh	kiloWatt-hour. 31, 32
kgm^2	kilogram-square meter. 30
mH	milliHenry. 30, 35–37
rad/s	radian per second. 66
rpm	revolutions per minute. 30, 50, 62, 66
s	seconds. 59, 60, 66, 69

CHAPTER ONE: INTRODUCTION

1.1 Background

The extraction and exploitation of non-renewable energy sources has been increasing exponentially every year with an increase in world population. This not only has led to the rapid depletion of such energy sources but also has resulted in undeniable impacts on the environment and society. The carbon-based fuels, like the fossil fuels that are widely used today, are unsustainable and unsafe because they contribute to greenhouse gas emissions, air pollution, water and soil contamination, climate change, global warming, and many other adverse impacts, thereby causing a serious threat to the modernising world. The transportation sector has been reported to have one of the largest carbon footprints, contributing significantly to greenhouse gas emissions and causing several environmental problems [1].

The extensive use of non-renewable energy sources, majorly coal and petroleum in the transportation sector despite their limited availability and high cost, has forced several countries to think of their best alternative in the near future. It is now high time to reduce the carbon footprints of the transportation sector due to pressing concerns such as pollution, global warming, depletion of the ozone layer, and the health risks these issues pose [2]. The search for a perpetual, safer, cleaner, environmentally friendly, and affordable fuel is never-ending. The possible alternatives to conventional fossil fuels are renewable energy sources such as the sun, wind, tides, hydropower, and biomass. Among these alternatives, solar power is the most preferred since it is the cleanest and most easily accessible sustainable form of energy with minimum operating costs.

1.1.1 Trend in Low-Power Electric Vehicles

Efforts are being made to transform the transportation sector from fossil fuel-based technology to clean and green technology with the integration of several renewable energy sources. Governments in some countries with expanding automotive markets have made some promising attempts to address the issues discussed above by promoting more efficient and decarbonised electric vehicle (EV) [3]. Various research studies are conducted all over the world every year to identify the optimal energy source that can be integrated with EV to meet the desired performance criteria and power requirements. On the other hand, the drive system of the EVs, including motor type, topology, design structure, control scheme, etc. are being modified to harness the energy available at the source end to the fullest extent so as to maximise the overall efficiency and reliability of the vehicles. In recent years, most well-developed countries have experienced a steady growth in the number of EVs being used. According to global statistics, by now more than 10 million EVs are on the road, and 47 % of these vehicles are only from China [4]. Similarly, in several other countries, more than 1 % of its market share are contributed by these vehicles.

The increasing trend of low-power electric vehicle (LPEV), such as electric scooters, electric bikes, and small electric urban cars, is driven by several factors. Some of these factors are as follows:

- **Urbanization and Traffic Congestion:** Growing urban populations have created the demand for compact, efficient, and manoeuvrable vehicles that can navigate crowded streets.

- **Environmental Concerns:** Rising awareness of climate change and air pollution has encouraged the adoption of cleaner, emission-free transportation options.

- **Cost-Effectiveness:** LPEVs are generally more affordable to purchase, operate, and maintain compared to traditional vehicles, which makes them appealing to cost-conscious consumers.

- **Technological Advancements:** Improvements in battery technology have extended the range and reduced the charging time of LPEVs, increasing their practicality.

- **Government Incentives:** Many governments are offering subsidies, tax benefits, and infrastructure development (e.g. charging stations) to promote the use of EVs.

- **Convenience for Short Trips:** LPEVs are ideal for short-distance commutes and last-mile connectivity, which aligns with the needs of many urban residents.

This trend reflects a shift towards more sustainable and efficient transportation solutions in response to modern social and environmental challenges. The demand for light commercial vehicles has grown rapidly in recent years, forcing manufacturers to compete to maximise their performance and minimise costs. The use of permanent magnet electric machines is growing every year in these vehicles due to their higher efficiency, power density, and ability to improve vehicle range and performance in contrast to conventional full-winding-based electric machines [5]. The permanent magnet machines commonly used in such vehicles include brushless DC (BLDC) motors, permanent magnet synchronous machine (PMSM) motors, synchronous reluctance motors, hybrid PMSM motors, etc. Although challenges related to the cost of permanent magnets, their availability, and sustainability still prevail, ongoing advancements in motor technology and manufacturing processes are expected to overcome these barriers soon, thereby paving the path for wider adoption across the globe.

1.1.2 Solar Powered Electric Vehicles

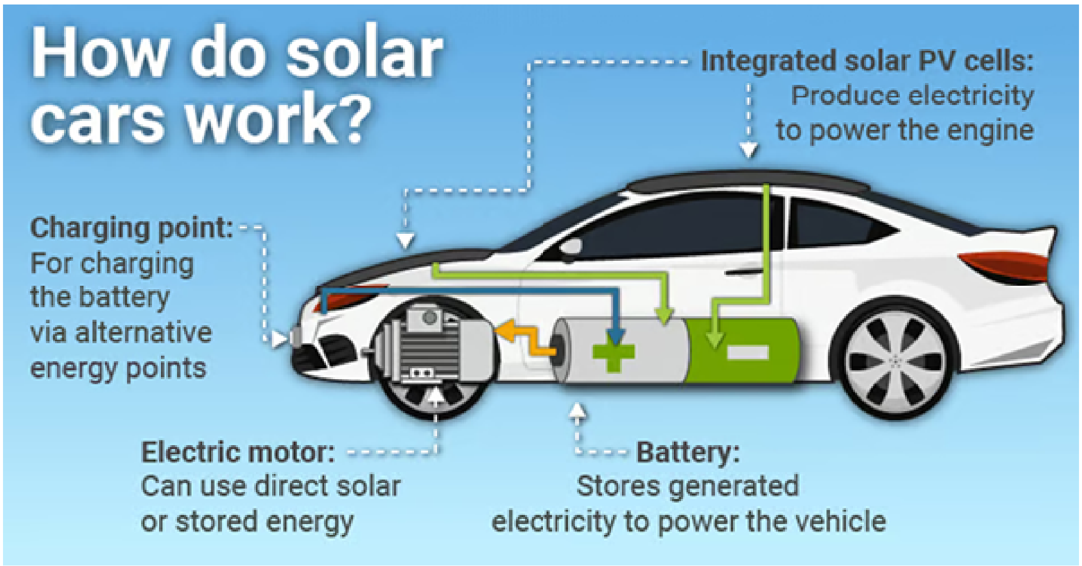

Figure 1.1: Basic topology of a solar electric car (greenmatch.co.uk)

Solar-powered EVs are a sustainable form of transportation that integrate solar panels to harness the energy of the sun and use it to power the vehicle. The concept combines renewable energy with EVs, offering a greener, more eco-friendly alternative to traditional fossil fuel vehicles. Solar-powered EVs typically have solar panels installed on their roofs or other surfaces. These panels capture sunlight and convert it into electricity, which can be used either to charge the vehicle's battery or directly power the embedded electric motor. This, in turn, loosens the reliance on conventional charging stations, which is beneficial in reducing energy bills. However, the power generated from the panels used might not be sufficient to fully power the vehicles used for long trips. So, conventional charging is still required for longer distances. Figure 1.1 shows a typical topology of an electric car with integrated solar photovoltaic panels on the roof.

With the latest developments in permanent magnet machines, the manufacturers of EVs are rapidly shifting towards the adoption of permanent magnet motors as the key element in the electric propulsion system of vehicles. The integration of renewable energy sources such as solar photovoltaic arrays into these vehicles has led to an improvement in the performance and energy efficiency of the vehicles and therefore contributed significantly to saving energy bills. BLDC motor being powered by a solar photovoltaic (SPV) system is one of the compelling alternatives to improving the efficiency of such EVs with minimal emissions [6]. Despite the limited literature available on SPV-integrated BLDC motors, many researchers have shown interest in extending the application of SPV systems in LPEVs [7–9]. This can potentially be the best substitute for the induction motor, the giant in the industrial market, which will indeed reduce the size and weight of the vehicle [10].

1.2 Statement of Problem

The implementation of a SPV system-driven BLDC motor drive must face several technical challenges. The first challenge is the irradiance and temperature dependence of solar power, leading to fluctuations in power generation. The irradiance and temperature depend further on the altitude, geographical, and climatic conditions of the place. Moreover, in an EV, conditions such as shading and non-uniform irradiance on PV panels cannot be ignored due to several reasons such as vehicle orientation with respect to sunlight, design constraints, nearby trees and buildings, cloud coverage, smoke and fog, etc. In a conventional single-input single-output (SISO) DC-DC converter-based system, the extraction of power from PV units is effective only when uniform irradiance is available throughout the panel surface. In such a system, solar power generation, while even working at MPPT, is significantly reduced by partial shading and impedance mismatching of series and parallel connected PV modules. Therefore, in the context where there are frequent changes in the working conditions of the SPV array, a significant drop in drive performance cannot be overlooked. Thus, to overcome this challenge, a rapidly converging maximum power point tracking (MPPT) control algorithm for the SPV array, along with a suitable converter topology to interface the array with the DC bus is required.

The second challenge is stabilisation and control of the DC bus voltage in the SPV system-driven BLDC motor drive against varying source (SPV array and battery) power generation and load requirements. In BLDC motors, controlling the speed above its base value is cumbersome and requires sophisticated control techniques only to achieve a slightly higher speed. However, controlling the speed below the base speed is easy and can be achieved by controlling the armature voltage directly without affecting motor health in the long run. However, the robustness and flexibility in speed control, in turn, depend on the electrical characteristics of the components, such as the battery and the DC-link capacitor. The inherent shortcomings of electrolytic capacitors include their poor lifespan, low-frequency operation and overweight. Most conventional EVs are still found to operate using these capacitors as a DC link, because of their low cost. In addition, to improve vehicle performance, a battery with a higher energy density, longer cycle life, fast charging capability, and more resistant to temperature must be preferred, which should also meet the desired safety standards. A combination of a film capacitor and a Lithium-ion battery is treated as a good choice to meet both the dynamic and steady-state requirements for LPEVs. However, an accurate study of the electrical characteristics of the battery as well as the characteristics of the motor drive is required before designing an appropriate control system to adjust the DC link voltage.

The third challenge is associated with the sensors used in BLDC motors that affect their design complexity and reliability. There are several inherent shortcomings associated with the BLDC motors that are based on position and speed sensors. Adding such sensors increases the design complexity and cost of the motor. Most of these sensors are sensitive to temperature, vibrations, and electromagnetic interference (EMI) and can lead to device failure, thereby reducing the reliability of the machine. They may require frequent maintenance when operating in harsh environments. Constraints such as the volume and weight of the machine could be a big challenge for sensor-based motors, especially when used in critical applications. Thus, the omission of these sensors contributes to reducing redundancy and thus improving the reliability of the BLDC motor drive. This, however, is feasible solely when the output from these physical sensors can be obtained through another method, by leveraging the electrical and mechanical properties of the motor.

In summary, the major problems to be addressed in the design and control of solar-powered BLDC motor drive can be listed as follows:

1. fluctuating input power from SPV array due to shading effect, varying irradiance and temperature
2. stabilisation and control of DC bus voltage against varying source power and load requirement
3. shortcomings of sensor-based motor drive such as poor reliability, increased cost, more space and weight requirements, etc

1.3 Objectives of Research

The general objective of this research is to propose, design, and simulate an energy-efficient and position sensorless model of solar-powered BLDC motor drive for LPEVs. The control approaches to be implemented will focus on overcoming the challenges/problems discussed in Section 1.2. The ultimate goal is to contribute to improving the efficiency and reliability of the overall system and reducing its redundancy through the careful selection and design of all the major components that make up the system.

The specific objectives of the project are listed below:

1. to extract optimal power available from SPV array through MPPT at any weather and temperature conditions

2. to stabilise DC-link voltage at all load conditions irrespective of battery state of charge (SoC) and solar power input

3. to realise sensorless commutation and speed control of BLDC motor

1.4 Overview and Scope of Research

The research work undergoes a comprehensive design of a solar-powered BLDC motor drive especially meant for LPEV applications such as e-rickshaws, electric cars, electric scooters, and e-bikes, followed by its control based on load requirements and available input power. The study starts with a detailed literature survey (presented in chapter TWO) on the existing MPPT techniques for extracting maximum solar input power and position sensorless control methods for a BLDC motor. Chapter THREE describes the overall system framework and detailed steps involved in selecting and designing major system components, accompanying calculations of several critical parameters that justify the design requirements. The major components involved in the design process include the BLDC motor, battery bank, SPV arrays, DC-DC converters, voltage source inverter (VSI) and DC-link capacitor. The control approaches of different components being used, such as MPPT control, DC-link voltage control and sensorless speed control of BLDC motor are described sequentially in detail including preliminary theoretical concepts wherever required. Chapter FOUR deals with the MATLAB Simulink model of the overall system. It explains various circumstances under which the simulations are performed and the parameters selected for different components while conducting the simulations. The results of these simulations are showcased and discussed in chapter FIVE. Finally, chapter SIX presents the conclusion of the research describing the effectiveness of the proposed model, its limitations, and potential extension.

The findings of this research provide critical insight into the selection of appropriate components, their sizes and capacities used in the topology design of solar powered BLDC motor drives. The research work demonstrates robust and safe control techniques used in controlling the battery charge, DC link voltage, motor speed, and solar power, which can be a helpful guide for researchers and engineers in improving the control system models applied in relevant applications. By demonstrating an adaptive and fast-converging MPPT technique, the work is supposed to contribute to improving the energy efficiency and performance of solar-driven EVs. Moreover, the proposed model in the research can pave new paths in improving the reliability of the BLDC drive system, since it introduces and validates a position sensorless commutation mechanism for the motor. Last but not least, the research will also help identify opportunities for further innovation by illustrating the limitations of the proposed models and the potential room for improvement.

CHAPTER TWO: LITERATURE REVIEW

2.1 Maximum Power Point Tracking Control

Solar power generation is mainly dependent on two parameters, irradiance and temperature. These parameters further rely on conditions such as the altitude and geography of the place, air quality, orientation of the panel with respect to sunlight, weather conditions, etc. For a particular working temperature and available irradiance, the power drawn from the panel varies with the input impedance seen by the terminal. This input impedance decides the slope of the load line, and the point of intersection of this line with the current-voltage (i-v) characteristics curve, in turn, gives the working point in terms of current, voltage, and power. Adjusting the slope of the load line so that the power being extracted can be maximised for a given temperature and irradiance conditions is called the maximum power point tracking (MPPT) control. Several algorithms for the MPPT control have been proposed and implemented in different works of literature over time. Each of these algorithms has its own benefits and limitations, which are discussed here.

The perturb and observe (P&O) algorithm is the most widely used and oldest algorithm. The method involves making small perturbations in voltages and monitoring the change in power (positive or negative) unless the change reduces to an acceptable degree close to zero. With an increase in voltage, if the change in power is positive, then the maximum power point (MPP) lies to the right of the current operating point, and therefore the effect is to further increase the voltage. However, if the change in power is negative, then the MPP lies to the left of the current operating point, and thus the effect is to reduce the voltage. Similarly, with the decrement in voltage, if the change in power is negative, then the MPP lies to the left of the current operating point, and thus the next step is to further decrease the voltage. However, if the change in power is positive, then the MPP lies to the right of the current operating point, and thus the effect is to increase the voltage. The perturbation in voltages is done at fixed time intervals indirectly using the duty ratio of the interface converter as a control variable. The conventional P&O method as described in [11, 12] uses a fixed perturbation size. The downside of fixed perturbation step size is slow convergence if the predetermined size is very small and higher oscillations if the size is too large. This challenge of optimal trade-off between power oscillation and convergence speed is overcome using modified P&O techniques discussed in [13] through adaptation of the perturbation size with the degree of change in the controlled power. Although the method is easy to implement and facilitates fast tracking of the MPP, the method still has an inherent inability to track global MPP under partial shading conditions where multiple MPPs arise.

The problem of oscillations around the MPP, as seen in P&O is mitigated in the incremental conductance (IncCond) algorithm as proposed in [14, 15]. The algorithm suits better in dynamic working conditions and performs well under partial shading. The technique employs the calculation of incremental conductance, which is the ratio of change in current to change in voltage of the SPV array. This value (di/dv) is compared with the negative of the measured current and voltage ratio, i.e. $-i/v$ at the same time instant. If $di/dv < -i/v$, then the current operating point lies to the right of the MPP; therefore, the voltage must be reduced in the next step. However, if $di/dv > -i/v$, then the current operating point lies to the left of the MPP; therefore, the voltage requires an increment in the following step. Condition $di/dv \approx 0$ implies near-to-MPP operation. The method requires more computational resources for the precise measurement of current and voltages and calculation of derivatives.

The simplest and lowest-cost method, called the constant voltage method [16, 17], is often used for its simplicity and the least-cost requirement. The method uses a fixed voltage value as the MPP voltage, which is usually between 70% and 80% of the open circuit voltage of the SPV array based on standard test conditions (1000 Wm^{-2} irradiance and 25 $°C$ temperature). The method can be realised using both analogue and digital circuits. The demerit is that the method is not suitable for dynamic conditions since it assumes a fixed MPP voltage and offers less accuracy under non-standard working conditions.

Apart from the aforementioned classical algorithms, various intelligent MPPT control techniques harnessing machine learning principles have been proposed. The most common of these algorithms are fuzzy logic controller (FLC) based [18, 19] and artificial neural network (ANN) based [20, 21]. Both algorithms offer a high degree of accuracy at the expense of computational resources such as training data and experiments. They can better adapt to varying irradiance and temperature conditions, resulting in a reduced oscillation of the operating point. The differences between these methods are that the former uses a predefined rule-based lookup table to make decisions on the output, whereas the latter requires training a model based on input and output data sets. In addition, the former can be less accurate at times despite offering a faster response, whereas the latter is relatively more accurate once trained.

In recent times, the applications of evolutionary algorithms have been extended to the MPPT control, inspired by their ability to optimise complex mathematical objective functions involving multiple optimal points. These algorithms are generally used in integration with the intelligent control algorithms discussed earlier to extend their strength. The most dominant ones are based on genetic algorithm (GA) [22, 23] and particle swarm optimization (PSO) [24, 25]. Unlike other methods that often fail to track the global MPP arising during partial shading conditions, these methods are very reliable in tracking the global or actual MPP and are less affected by noise. However, the setback of GA and PSO-based MPPT algorithms is that they take relatively more time to converge to the global optimum, offering a slower response. Besides, they require higher computational resources for real-time applications. The study of various evolutionary algorithms proves the superiority of PSO over GA in terms of the speed of convergence. In [26], a hybrid method has been proposed combining the conventional PSO with the P&O method to harness the higher accuracy offered by the PSO method and the fast response feature of the P&O method.

A summary of the MPPT techniques discussed is presented in Table 2.1. The solar panel mounted on the roof of an EV experiences fluctuating irradiance due to several reasons such as vehicle direction of motion and its orientation relative to sunlight, design constraints, nearby trees and buildings, cloud coverage, smoke and fog, etc. Thus, the vehicle operates most of the time under dynamic conditions and therefore requires an adaptive and fast convergent MPPT algorithm to stabilise the operating point at or close to the actual MPP suppressing power oscillations. As mentioned in [27], a virtual optimal resistance (VOR)-based P&O algorithm seems to be highly effective under such dynamic working conditions. The resistance is simply the voltage to current ratio seen by the SPV array that can be used as a hidden control parameter to indirectly adjust the operating point to the actual MPP by generating an appropriate duty ratio. The study shows that the change in array's current rather than the array's voltage is more sensitive to the shift in the MPP due to fluctuation in temperature and irradiance. Hence, unlike in the conventional P&O MPPT technique where voltage is used as the perturbation parameter, optimisation of solar output power can be better achieved by perturbing the ratio of current to voltage (i.e. the inverse of VOR).

Table 2.1: Summary of MPPT control algorithms

Refs.	**Control Techniques**	**Description**	**Key Features**	**Limitations**
[11–13]	Perturb and Observe (P&O)	perturbs voltage and observes power changes	simple implementation, fast tracking of the MPP	• struggles under partial shading • trade-off between power oscillations and convergence
[14, 15]	Incremental Conductance (IncCond)	uses incremental conductance to determine MPP direction	• better for dynamic conditions • good performance under partial shading	• requires more computational resources • precise measurement needed
[16, 17]	Constant Voltage Method	uses a fixed voltage (70%-80% of open-circuit voltage) as MPP voltage	simple and low-cost implementation	• not suitable for dynamic conditions • less accurate in non-standard conditions
[18, 19]	Fuzzy Logic Controller (FLC)	uses predefined rule-based lookup table for decision making	• fast response • adapts to varying conditions	requires expert knowledge for rule formulation
[20, 21]	Artificial Neural Network (ANN)	requires training with input-output datasets for MPPT tracking	• high accuracy • adapts well to varying conditions	• needs training data and experiments • computationally expensive
[22, 23]	Genetic Algorithm (GA)	evolutionary optimization technique applied to MPPT	effective in finding global MPP under partial shading	• slower response • high computational demand
[24, 25]	Particle Swarm Optimization (PSO)	inspired by swarm intelligence to optimize MPP tracking	• faster convergence than GA • reliable under partial shading	• higher computational requirements • may take more time to converge
[26]	Hybrid PSO - P&O	combines PSO's accuracy with P&O's fast response	optimized tracking with better speed and accuracy	computational complexity increases

2.2 Position Sensorless Motor Control

To overcome the challenges associated with sensor-based operation discussed in Section 1.2, many methods have been proposed in the literature that describe and validate the operation of BLDC motors without any position or speed sensors. These methods can be broadly classified as:- back-electromotive force (BEMF) estimation methods [28–30], BEMF integration methods [31, 32], free-wheeling diode current detection methods [33], and third-harmonic voltage component detection methods [34, 35].

The BEMF estimation methods depend on the detection of zero-crossing instants of the BEMF across each phase, harnessing the measured stator phase or line voltages. In [28], terminal voltages are measured with respect to a virtual neutral point, and low-pass filters have been used to eliminate higher-order harmonics. The limitations of this approach are the oscillation of the neutral point during PWM switching and delays introduced by the filters, which does not make this approach suitable for a wide speed range. In [29], a method to estimate BEMF indirectly without using the true neutral or virtual neutral potential has been proposed. The technique used in [30] is defining a function to indicate the switching instants, that depends on measured voltages, currents and the derivatives of the currents. Although the EMF is sensed without the need for the true or virtual neutral point, the technique still relies on the complex computation of derivatives and could be affected by sensor noise.

The BEMF integration method used in [31] and [32] is based on integrating the BEMF of the open phase. The integration starts right at zero-crossing point (ZCP) of BEMF and is stopped when the integration result reaches a preset threshold value that indicates the commutation instant. The benefit of this method is that it is less sensitive to noise and offers good performance at high speeds. The downside is that the method still requires neutral potential and may result in accumulated error, especially at low speeds due to the integration operation.

The free-wheeling diode current detection methods [33] involve sensing the current in a free-wheeling diode connected across the open phase, which facilitates in knowing the position of the rotor. The method is well suited for wide operating regions. However, the implementation of this method requires six comparators, each with its own power source, to detect the free-wheeling currents. Thus, the implementation of this method demands a complex and more costly control circuitry.

The third harmonic component of the BEMF is obtained by adding all three terminal voltages [34,35]. Integrating this component gives the third harmonic flux linkage whose zero crossing corresponds to the commutation instants. The limitation of this approach is that it requires the neutral point of the stator winding, which is normally not provided by the manufacturer. Besides, the amplitude and phase of harmonic components could be affected by magnetic saturation, thereby preventing the detection of true zero-crossing instants.

Apart from these methods, an extended Kalman filter (EKF)-based estimation method has also been proposed in [36]. Though this method being based on machine learning, is very little affected by the noise in measurement and processing data, it requires a precise mathematical model of the motor to work with. The major challenge in applying this method is the initialisation of the covariance matrices, which indicate uncertainties in the measured and estimated parameters. Poorly initialised values can often lead to divergence and instability. In addition, the method does not fit well, especially under low-speed conditions because of low estimating accuracy.

Table 2.2 presents the summary of the methods discussed. The choice of the best sensorless control technique depends on various factors such as applicable speed range, safety standards, commutation accuracy, noise tolerance, components requirements, etc. Taking into account all these factors, the most robust and easy-to-implement control method is still based on zero crossing detection of BEMFs. The method is the optimal choice for engineers when constraints like commutation accuracy, speed range, hardware requirements, and cost are to be kept in view while maximising performance. However, the method as proposed in [37], demands filter circuits to mitigate false zero-crossings of the BEMF waveforms, which would then require compensation for the delays introduced by these circuits to maintain the accuracy of the estimated zero-crossing points. On the other side, tuning the clock frequency of the delay counters as per the motor speed, discussed in the proposed method, is not a hassle-free task. Thus, the method requires seeking an alternative way to eliminate the need for filters and counters and thereby enhance the accuracy and ease of control.

Table 2.2: Summary of sensorless motor control methods

Refs.	Control Techniques	Description	Key Features	Limitations
[28]	Direct BEMF estimation methods	direct detection of ZCPs of phase BEMFs	stator terminal voltages measured w.r.t virtual neutral point	• oscillation of the neutral point during pulse width modulation (PWM) switching • not suitable for a wide speed range due to delays introduced by the filters
[29,30]	Indirect BEMF estimation methods	indirect detection of ZCPs of phase BEMFs	• stator terminal voltages measured without using true/virtual neutral point • computation of derivatives of current	• noise-sensitive method may lead to false commutation and instability • not suitable for high-speed operation
[31,32]	BEMF integration methods	integration of BEMF of open phase from ZCP to commutation point	• less noise-sensitive • offers good performance at high speeds	• requires neutral potential • not suitable for low-speed operation due to accumulated error in integration
[33]	Freewheeling diode current detection methods	sensing of current in free-wheeling diode connected across the open phase	• requires six comparator circuits • suitable for wide speed range	inherent design complexity
[34,35]	Third harmonic voltage component detection methods	detection of ZCPs of third harmonic flux linkages obtained by adding and integrating measured terminal voltages	requires access to stator neutral potential	affected by magnetic saturation
[36]	extended Kalman filter	speed estimation using mathematical model of motor and real-time data	• less affected by measurement noise • two step iterative algorithm: prediction and update	• poorly initialized covariance matrices leads to divergence and instability • not suitable for low speed operation

CHAPTER THREE: METHODOLOGY

3.1 System Architecture

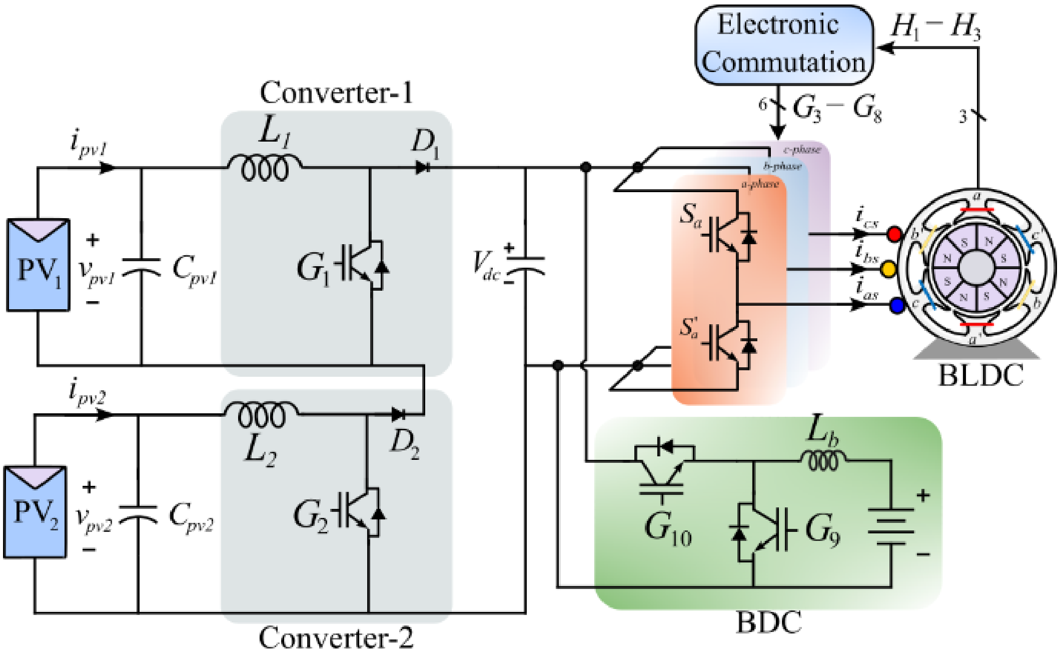

Figure 3.1: Schematic of the proposed model

A topology of the proposed model to drive a 2.5 kW, 240 V BLDC motor is shown in Figure 3.1. The system comprises two SPV array units and a battery bank connected to a common DC link capacitor via a multiple input single output (MISO) boost converter and a bidirectional buck-boost converter respectively. The BLDC motor is powered through the insulated gate bipolar transistor (IGBT) based three-phase two-level VSI serving as an electrical commutator circuit for the motor. The switching pulses for the buck converter are generated from the MPPT control algorithm for the SPV arrays to ensure the extraction of the maximum solar power available. The switching pulses for the bidirectional converter are derived from the battery DC-link voltage controller. The bidirectional converter facilitates the charging of the battery from the SPV arrays when the motor is disconnected from the DC bus and its discharging to feed the load when the motor is connected to the DC bus. The DC-link voltage controller acts to establish a fairly constant voltage level as per the speed requirement by adjusting the duty ratio of the bidirectional converter. The reference voltage required for the voltage controller is provided by the speed controller. The position sensorless electronic commutation logic is implemented, where the switching pulses required for the VSI are synthesised by detecting the ZCPs of the measured line voltage differences. The frequency of these switching pulses is controlled by the speed controller so as to acquire the desired speed level.

3.2 System Design

3.2.1 Selection of BLDC Motor

Table 3.1: BLDC motor specifications

Parameters	**Values**
Number of phases	3
Number of poles (p)	2
Rated Voltage (V_{rated})	$240\ V$
Rated Speed (N_{rated})	$1500\ rpm$
Rated Torque (τ_{rated})	$15.9\ Nm$
Stator Resistance (R)	$1.2\ \Omega$
Stator Inductance (L)	$8.5\ mH$
Moment of Inertia (J)	$0.08\ kgm^2$
Damping Coefficient (B)	$0.001\ Nms/rad$
Back-EMF constant (k_m)	$1.346\ Vs/rad$

A $240\ V$, $2.5\ kW$, $1500\ rpm$ BLDC motor with 85 % efficiency (η) is selected for the proposed model. The detailed specification of the motor is presented in Table 3.1. For the motor BEMF constant of $1.346\ Vs/rad$, the BEMF at full load is calculated as:

$$E_{FL} = k_m \times N_{rated} = 1.346 \times 1500 \times \frac{\pi}{30} = 211.43\,V \tag{3.1}$$

Ignoring friction and windage losses in the motor, the peak value of motor armature current at full load can be computed as:

$$I_{mot(FL)} = \frac{P_{rated}}{E_{FL}} = \frac{2500}{211.43} = 11.82\,A \tag{3.2}$$

Also, the power consumed by the motor at full load is calculated as:

$$P_{mot(FL)} = \frac{P_{rated}}{\eta} = 2.94\,kW \tag{3.3}$$

3.2.2 Selection of Battery

Table 3.2: Battery specifications

Parameters	Values
Nominal Voltage (V_{bat})	48 V
Nominal Capacity (Wh_{bat})	15.5 kWh
Maximum Full-Charge Voltage (V_{max})	51.2 V
Discharge Cut-off Voltage (V_{min})	40 V
Maximum Discharge Current ($I_{dis(max)}$)	100 A
Maximum Charge Current ($I_{chg(max)}$)	50 A
Cycle Life (at 80 % DoD)	>2000 cycles
Operating Temperature	-20 °C to 60 °C

Considering the losses in the VSI, converters and the DC bus to be around 5 % of the full load motor input power ($P_{mot(FL)}$), the power injected into the DC bus becomes approximately 3.1 kW. The battery size is determined such that the motor can run at full load for around 3 hours. With permissible depth of discharge (DoD) of 60 %, the required battery capacity is given by the following equation.

$$Wh_{bat} = \frac{3.1 \times 3}{0.6} = 15.5\, kWh \tag{3.4}$$

To achieve such capacity, a Lithium-ion ($LiFePO_4$) battery bank with nominal voltage (V_{bat}) of 48 V (16 cells each of 3 V connected in series) is chosen. Thus, the Ampere-hour capacity of the battery bank becomes 323 Ah. Other specifications of the battery are presented in Table 3.2. Care should be taken to ensure that the maximum charging and discharging currents of the battery are well within the safe limits specified by the manufacturers. The purpose of choosing a lithium-ion battery is due to its superior characteristics, such as fast charging/discharging, long life, and high energy density, which are favourable for electric vehicles [38]. Moreover, these batteries exhibit charge and discharge properties with the most consistent flat region, as demonstrated in Figure 3.2. Thus, such batteries operate at constant voltage most of the time throughout the charging and discharging processes, allowing them to form a stiff DC bus.

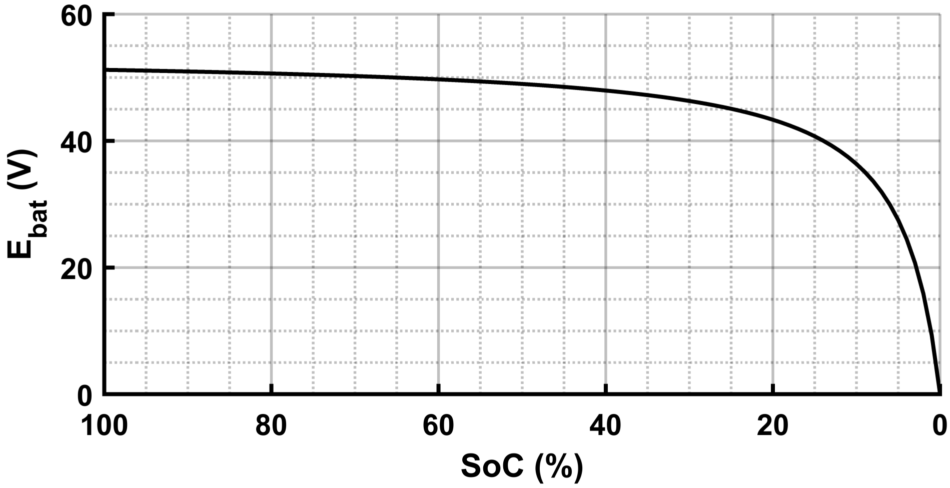

Figure 3.2: Charge/discharge characteristics of a Li-ion battery

3.2.3 Design of SPV Array

Table 3.3: PV module specifications at standard test conditions

Parameters	Values
No. of Cells ($N_{c(mod)}$)	60
Open-Circuit Voltage ($V_{(mod)oc}$)	36.5 V
Short-Circuit Current ($I_{(mod)sc}$)	8.78 A
Voltage at Maximum Power ($V_{(mod)m}$)	29.5 V
Current at Maximum Power ($I_{(mod)m}$)	8.1 A
Temperature Coefficient of $V_{(mod)oc}$ ($\mu_{(mod)oc}$)	-0.3305 %/ $°C$
Temperature Coefficient of $I_{(mod)sc}$ ($\mu_{(mod)sc}$)	0.0638 %/ $°C$

The size of the SPV array is constrained by the available space in the vehicle and its geometry, load requirements, and cost of the array units. Two SPV array units of different sizes are proposed - the larger unit is to be mounted on the roof and the smaller one on the rear side of the vehicle. The split distribution of array panels allows for reducing the drop in power generation due to shading, vehicle motion, and orientation with respect to incident sunlight. The peak power capacity of the larger array unit ($P_{pv1(m)}$) is chosen to be 0.48 kW and that of the smaller unit ($P_{pv2(m)}$) is selected to be half of the larger unit's capacity, considering standard test conditions (i.e. 1000 Wm^{-2} Irradiance; 25 $°C$ cell temperature; 1.5 air mas (AM) spectrum). Thus, the total capacity of the array units is approximately 0.72 kW. This is achieved using PV modules belonging to the TATA Power Solar Systems TP240 MBZ model with specifications as shown in Table 3.3.

For the larger unit (unit 1), the maximum array voltage ($V_{pv1(m)}$) is set to 59 V. The maximum current of the unit ($I_{m(pv1}$) can be estimated as:

$$I_{pv1(m)} = \frac{P_{pv1(m)}}{V_{pv1(m)}} = \frac{480}{59} = 8.1\,A \tag{3.5}$$

If N_{s1} and N_{p1} represent the number of series-connected PV modules per string and number of such strings connected in parallel, respectively, to form the array unit of desired power rating, then their values can be approximated as:

$$\begin{aligned} N_{s1} &= \frac{V_{pv1(m)}}{V_{mod(m)}} = \frac{59}{29.5} = 2 \\ N_{p1} &= \frac{I_{pv1(m)}}{I_{mod(m)}} = \frac{8.1}{8.1} = 1 \end{aligned} \tag{3.6}$$

Therefore, a string containing 2 series-connected PV modules is required to form the larger SPV array unit.

Similarly, for the smaller unit (unit 2), the maximum array voltage ($V_{pv2(m)}$) is set to 29.5 V. The maximum unit current ($I_{m(pv2}$) can be computed as:

$$I_{pv2(m)} = \frac{P_{pv2(m)}}{V_{pv2(m)}} = \frac{240}{29.5} = 8.1\,A \tag{3.7}$$

Also, the number of series-connected PV modules per string and number of such strings connected in parallel can be approximated as:

$$\begin{aligned} N_{s2} &= \frac{V_{pv2(m)}}{V_{mod(m)}} = \frac{29.5}{29.5} = 1 \\ N_{p2} &= \frac{I_{pv2(m)}}{I_{mod(m)}} = \frac{8.1}{8.1} = 1 \end{aligned} \tag{3.8}$$

Therefore, a string containing only one PV module is required to form the smaller array unit.

3.2.4 Design of Boost Converter

As proposed in some works of literature [39,40], MISO DC-DC converter-based systems help in overcoming the sudden drop in power generation due to non-uniform irradiance and impedance mismatching of SPV arrays operating in parallel. Since each array unit will have its own MPPT controller, optimal power extraction from one array unit is unaffected by the change in operating conditions (irradiance and temperature) of the other units. Thus, a MISO topology comprising of two boost converters, each interfacing one SPV array unit to the DC bus, is proposed. The duty ratios to control these converters are derived and fed from separate MPPT controllers.

For both converters (converter 1 and converter 2), the output voltage is the DC bus voltage ($V_{dc} = 240\ V$). Let d_1 and d_2 represent the duty ratios for converter 1 and converter 2 respectively. Setting their input voltages to be the maximum respective array unit voltages, the corresponding duty ratios can be computed using the following equations [41]:

$$d_1 = 1 - \frac{V_{pv1(m)}}{V_{dc}} = 0.754 \tag{3.9}$$

$$d_2 = 1 - \frac{V_{pv2(m)}}{V_{dc}} = 0.877 \tag{3.10}$$

Let, L_1 and L_2 denote the value of the inductors to be used in converter 1 and converter 2 respectively. For each converter unit, taking inductor ripple current (ΔI_L) to be 20 % of the maximum average current drawn from the respective SPV array unit ($I_{m(pv)}$), switching frequency (f_s) of 5 kHz, the sizes of the inductors are then calculated as follows [42]:

$$L_1 = \frac{d_1 \times V_{pv1(m)}}{f_s \times \Delta I_{L_1}} = \frac{0.754 \times 59}{5000 \times 0.2 \times 8.1} = 5.49\ mH \tag{3.11}$$

$$L_2 = \frac{d_2 \times V_{pv2(m)}}{f_s \times \Delta I_{L_2}} = \frac{0.877 \times 29.5}{5000 \times 0.2 \times 8.1} = 3.19\ mH \tag{3.12}$$

3.2.5 Design of Bidirectional Buck-Boost Converter

The bidirectional converter, as shown in Figure 3.1, operates in boost mode during discharging of the battery and in buck mode throughout the battery charging period with current direction reversed. However, during buck mode operation, the motor is disconnected and the array units feed the battery. Hence, the converter control is triggered by two different duty ratios based on its operating mode. The values of these duty ratios depend on the magnitude of the DC-link voltage (V_{dc}) and the battery's nominal voltage (V_{bat}). During boost mode operation, the input to the converter is the battery voltage and the output is the DC link voltage, whereas during buck mode operation, the input and output are reversed.

Firstly, the duty ratio for its boost mode operation $d_{3(boost)}$ is computed using the following relation:

$$d_{3(boost)} = 1 - \frac{V_{bat}}{V_{dc}} = 1 - \frac{48}{240} = 0.8 \tag{3.13}$$

Secondly, the duty ratio for its buck mode operation $d_{3(buck)}$ is computed using the following relation [41]:

$$d_{3(buck)} = \frac{V_{bat}}{V_{dc}} = \frac{48}{240} = 0.2 \tag{3.14}$$

Whether the converter is operating in buck mode or in boost mode, the average inductor current is equal to the average battery current. The average current fed by the battery operating in parallel with the two SPV array units (at standard operating conditions) while the motor being fully loaded is obtained using (3.2), (3.5), (3.7), (3.9), (3.10) and (3.13) as:

$$I_{bat(FL)} = \frac{I_{mot(FL)} - I_{pv1(m)} \times (1 - d_1) - I_{pv2(m)} \times (1 - d_2)}{1 - d_{3(boost)}} = 44.07\,A \tag{3.15}$$

Again we choose the inductor ripple current (ΔI_{L_b}) to be 20 % of the average battery discharge current at full load ($I_{bat(FL)}$), and the switching frequency (f_s) of 5 kHz. Then, the value of inductor L_b for boost mode operation can be calculated using the following relation [42]:

$$L_{3(boost)} = \frac{d_{3(boost)} \times V_{bat}}{f_s \times \Delta I_{L_b}} = \frac{0.8 \times 48}{5000 \times 0.2 \times 44.07} = 0.87\,mH \tag{3.16}$$

During buck mode operation, the DC link voltage is always set to 240 V despite a rise in battery voltage due to the charging action or fluctuation of solar power. The average current input to the bidirectional converter, considering the standard SPV operating conditions, is obtained using (3.5), (3.7), (3.9) and (3.10) as:

$$I_{dc(pv)} = I_{pv1(m)} \times (1 - d_1) + I_{pv2(m)} \times (1 - d_2) = 3\,A \tag{3.17}$$

Using the same current ripple criteria and switching frequency parameter as in (3.16), the value of inductor L_b for buck mode operation can be obtained using the relation described in [42] as:

$$L_{3(buck)} = \frac{(1 - d_{3(buck)}) \times V_{bat}}{f_s \times 0.2 \times I_{dc(pv)}} = \frac{(1 - 0.2) \times 48}{5000 \times 0.2 \times 3} = 12.8\, mH \tag{3.18}$$

The size of an inductor is inversely proportional to the magnitude of the current ripple that it handles. The inductor ripple currents for the boost mode and buck mode operations are different. The actual size of the inductor to be chosen for the design is decided by the lowest magnitude ripple current and is thus given by the following equation:

$$L_3 = max\{L_{3(boost)}, L_{3(buck)}\} = 12.8\, mH \tag{3.19}$$

Now, for selecting the size of the capacitor C_b connected across the battery bank, a capacitor voltage ripple (ΔV_{C_b}) of 2 % of the battery nominal voltage V_{bat} is considered. The value of the capacitor is computed using [41] as:

$$C_b = \frac{0.2 \times I_{dc(pv)}}{8 \times f_s \times \Delta V_{C_b}} = \frac{0.2 \times 3}{8 \times 5000 \times 0.02 \times 48} = 15.6\, \mu F \tag{3.20}$$

3.2.6 Selection of DC-link Capacitor

A film capacitor is selected as the DC-link capacitor because of its superior electrical and thermal characteristics. Since the boost converters and the bidirectional buck-boost converters all share the common DC-link capacitor, the selection of its appropriate size relies on the minimisation of the ripple voltage. Due to the inverse relationship between the capacitor size and the magnitude of the voltage ripple across it, the capacitor size is maximised if the voltage ripple is minimised.

The common consideration in computing the capacitor size for any converter is the percentage of ripple voltage, which is 2 % of the standard DC bus voltage 240 V. For the boost converter 1, the size of the capacitor is given by [41],

$$C_1 = \frac{d_1 \times (1 - d_1) \times I_{pv1(m)}}{f_s \times 0.02 \times V_{dc}} = \frac{0.754 \times (1 - 0.754) \times 8.1}{5000 \times 0.02 \times 240} = 62.6\, \mu F \tag{3.21}$$

For the boost converter 2, the size of the capacitor is given by,

$$C_2 = \frac{d_2 \times (1 - d_2) \times I_{pv2(m)}}{f_s \times 0.02 \times V_{dc}} = \frac{0.877 \times (1 - 0.877) \times 8.1}{5000 \times 0.02 \times 240} = 36.40\, \mu F \tag{3.22}$$

Again, considering the bidirectional converter's boost mode operation, the capacitor size is computed as:

$$C_3 = \frac{d_{3(boost)} \times (1 - d_{3(boost)}) \times I_{bat(FL)}}{f_s \times 0.02 \times V_{dc}} = \frac{0.8 \times (1 - 0.8) \times 44.07}{5000 \times 0.02 \times 240} = 293.8\, \mu F \tag{3.23}$$

Hence, as discussed before, the actual size of the DC-link capacitor is given by,

$$C_{dc} = max\{C_1, C_2, C_3\} = 293.8\, \mu F \tag{3.24}$$

3.2.7 Design of Voltage Source Inverter

The motor is driven using a two-level three-phase VSI consisting of 6 IGBT switches, as shown in Figure 3.1. Overloading of these switches can lead to inverter failure. Therefore, the capacity of these switches should be carefully selected to prevent such a failure. To accommodate transients likely to occur in the inverter switches, as suggested in [43], a voltage safety factor of 1.4 and a current safety factor of 1.3 are considered. Therefore, the required voltage rating (V_{VSI}) and current rating (I_{VSI}) of each IGBT switch are calculated as:

$$\begin{aligned} V_{VSI} &= 1.4 \times V_{dc} = 1.4 \times 240 = 336\, V \\ I_{VSI} &= 1.3 \times I_{mot(FL)} = 1.3 \times 11.82 = 15.37\, A \end{aligned} \tag{3.25}$$

Thus, the Volt-Ampere (VA) rating of the IGBT switches is estimated as:

$$(VA)_{VSI} = V_{VSI} \times\ I_{VSI} =\ 336 \times 15.37 = 5.16\, kVA \tag{3.26}$$

3.3 Control Strategy

The control technique employed in the proposed model mainly focusses on the extraction of maximum power from the SPV array through MPP operation for all weather and atmospheric conditions, establishment of constant voltage across the DC link capacitor despite variations in source and load conditions, and sensorless electronic commutation of the motor followed by its closed-loop speed control.

3.3.1 MPPT Control

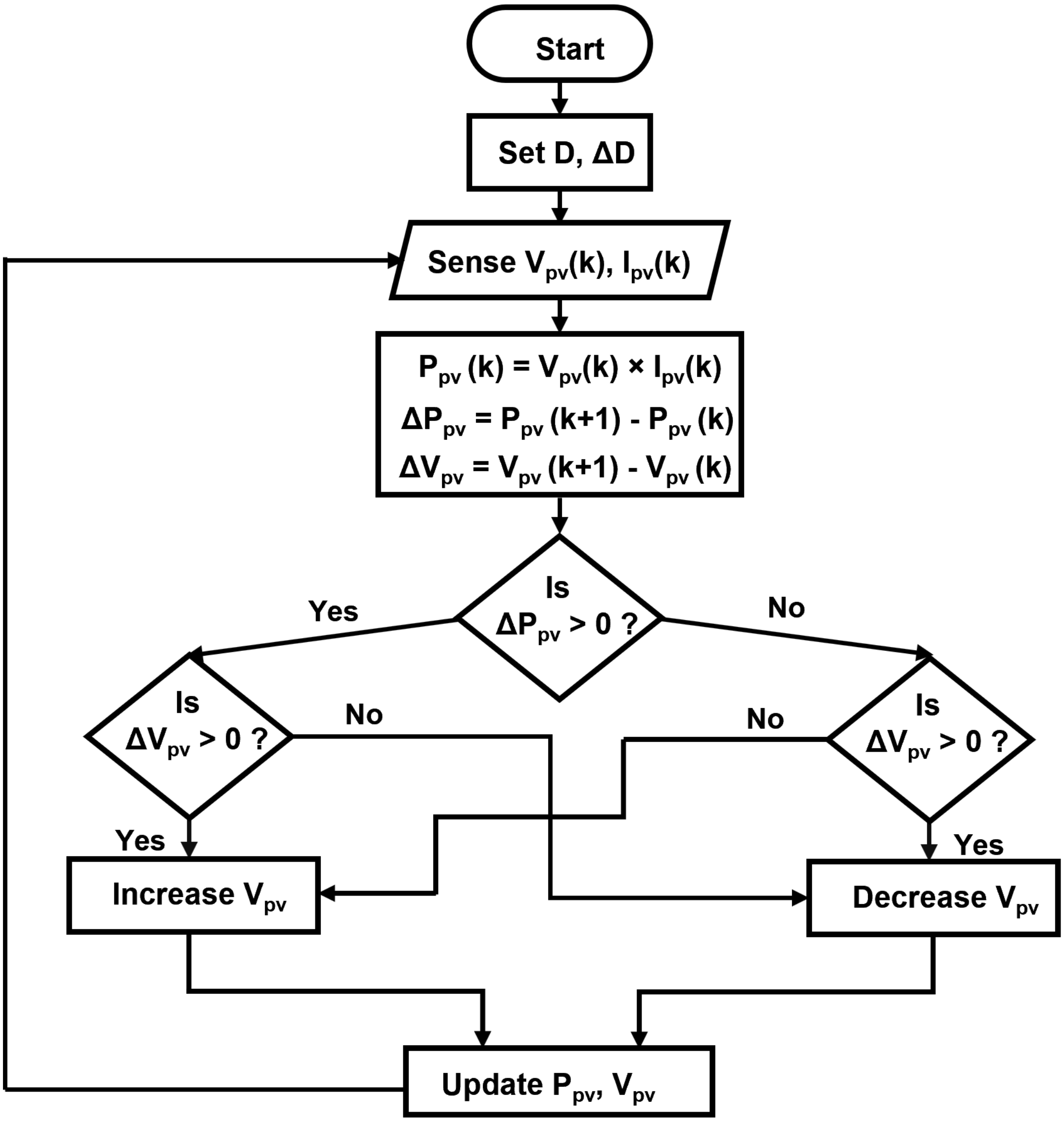

Figure 3.3: Flowchart of conventional P&O MPPT algorithm

To set the operating point at or near the actual MPP suppressing power oscillations due to rapid changes in working conditions of the SPV array and step perturbation size of the control parameter, a modified VOR based P&O

algorithm [34] is used. In the conventional P&O algorithm illustrated in Figure 3.3, the duty ratio is used as the control parameter to adjust the solar voltage to affect the output power. The voltages and currents are measured and sampled at appropriate time intervals and are multiplied to get the power output (P_{pv}). The difference in current and previous power output (dP_{pv}) is calculated and based on the positivity or negativity of dP_{pv}, an appropriate decision is made whether to increase or decrease the voltage. However, this algorithm leads to slow convergence and power oscillations at the optimal point of operation. The proposed VOR based P&O algorithm is supposed to overcome the issues that have been discussed by ignoring very small changes in measured power but reacting very quickly to any considerable shift in the optimal operating point due to sudden changes in temperature or irradiance.

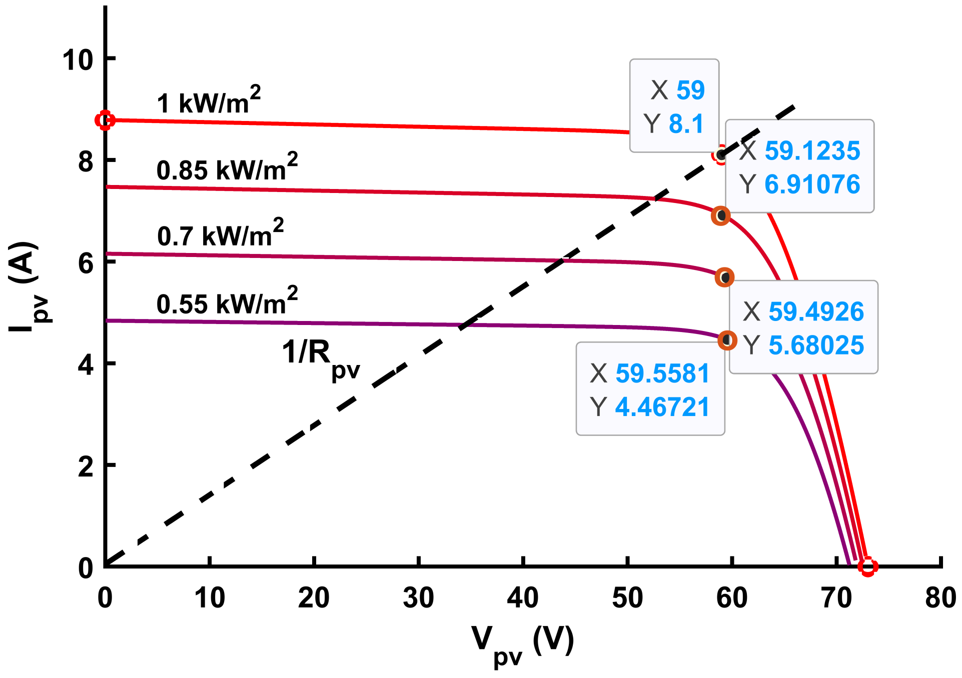

Figure 3.4: Shift in MPP of SPV module under varying irradiance

The MPPT control algorithm is initialised by setting the operating point close to the MPP point based on the standard test conditions where $V_{pv} = 0.8 \times V_{pv(oc)}$ and $I_{pv} = 0.9 \times I_{pv(sc)}$. The method proposed first measures the array voltage V_{pv} and current I_{pv}, followed by the computation of power as $P_{pv} =$

$V_{pv} \times I_{pv}$. In addition to this, the method also computes the ratio of the array voltage to current, resulting in a value called input resistance ($R_{pv} = V_{pv}/I_{pv}$). This is the virtual resistance as seen by the array unit across its terminals. Under constant irradiance and temperature conditions, the increment (or decrement) in this input resistance leads to an increment (or decrement) in the operating voltage. This can be verified from the i-v characteristics curve shown in Figure 3.4 of the solar module, where the current decreases with an increase in voltage. Thus, input resistance can be treated in some way as a monotonic function of the voltage and, therefore, can be used as a control variable instead of voltage. Moreover, the figure clearly explains that under varying irradiance, the change in operating voltage is much less sensitive to the shift in MPP, whereas the change in current is more. In other words, the input resistance is more sensitive than the voltage to the change in irradiance. Hence, the other advantage of using virtual input resistance as a control parameter to replace the voltage is that it offers faster convergence in dynamic conditions.

After computing the power and resistance in the current step, the difference between the power in the current step and the power of the previous step (dP_{pv}) is calculated. If $r > 0$ represents a small positive step change in the input resistance (i.e. perturbation in resistance), then the difference in the resistance in the current step and the resistance in the previous step ($dR_{pv} = \pm r$) is known. The following two cases arise based on the previous step actions.

Case 1: $dR_{pv} > 0$
If $dP_{pv} > 0$, R_{pv} is further increased to $R_{pv} + dR_{pv}$.
If $dP_{pv} < 0$, R_{pv} is decreased to $R_{pv} - dR_{pv}$

Case 2: $dR_{pv} < 0$
If $dP_{pv} > 0$, R_{pv} is further decreased to $R_{pv} - dR_{pv}$.
If $dP_{pv} < 0$, R_{pv} is increased to $R_{pv} + dR_{pv}$

The change in resistance is realized through an emulator, and its effect is monitored. The resulting output voltage of the array is used to compute the new duty ratio required for the converters. The resistance is a hidden control parameter as there exists no such physical resistance in the system architecture. The virtual resistance is, however, useful in computing the duty ratio and thereby adjusting it to an appropriate value, ensuring MPPT control.

3.3.2 DC-link Voltage Control

The smooth control of the speed of the motor, as well as the charging of the battery, is only possible through the control of the DC-link voltage. The battery charge controller controls the charging and discharging of the battery depending on the state of charge (SoC) level of the battery to regulate the DC bus voltage. The purpose of a battery charge controller is to monitor the SoC level of the battery and decide when to charge and when to discharge based on predefined rules. The battery is neither allowed to charge to the fullest limit nor allowed to completely discharge in order to enhance the cycle life of the battery. Thus, the upper limit of the permissible SoC is set to 95 %, and the lower limit is set to 35 %, allowing DoD range of only 60 %. If the battery SoC level is greater than or equal to 95 %, then the discharging mode is initiated; else, if it is less than or equal to 35 %, then the charging mode starts. The bidirectional converter operates in boost mode while the battery is discharging to drive the motor along with the SPV array and operates in buck mode while it is being charged from the SPV array. During boost mode operation, the gate signal G_9 is generated, which makes the shunt IGBT switch functional and during the buck mode operation, gate signal G_{10} is generated that triggers the series IGBT switch.

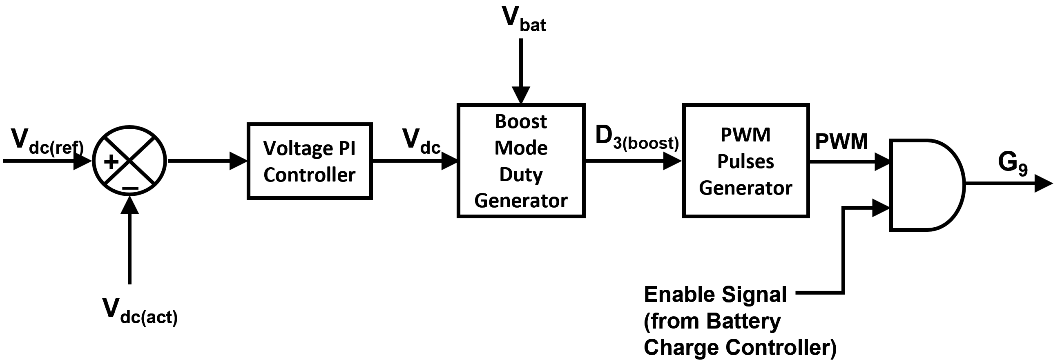

Figure 3.5: DC-link voltage controller for discharging mode

The battery, along with the support of the DC-link capacitor, is supposed to mitigate any voltage fluctuations across the DC bus due to sudden changes in motor load and solar power injection. Two different voltage control loops with complementary action are proposed. One of them is functional during the battery charging mode, whereas the other one operates during the battery discharging mode. However, the objective of both control loops is to stabilise the DC bus voltage to a fairly constant value as per the requirement. At first, the voltage control loop presented in Figure 3.5 for battery discharging mode is discussed. The reference voltage is the desired voltage level which is generated by the speed controller. The control scheme compares the measured speed with the reference speed to produce some error, which is then processed by a proportional integral (PI) controller. The output of the PI controller is converted to an equivalent duty ratio through a mathematical function which implements the relation described by the equation (3.13) to compute the required duty ratio $d_{3(boost)}$ and feeds to the PWM generator block. The PWM generator block generates the equivalent PWM signal G_9, which is used for triggering the shunt switch of the bidirectional converter.

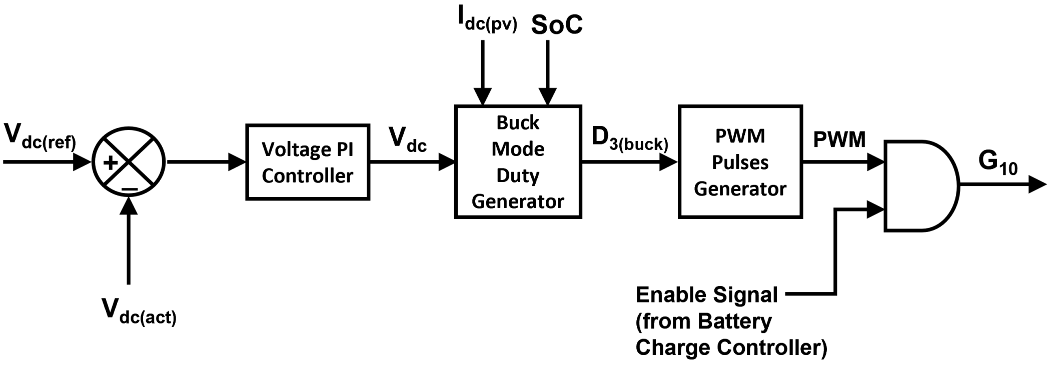

Figure 3.6: DC-link voltage controller for charging mode

Figure 3.6 shows the DC-link voltage controller for the battery charging mode. Unlike the other control loop for battery discharging mode, this control loop always takes a fixed value of 240 V as the reference DC bus voltage. The purpose of this is to set the DC bus voltage at its standard level ($V_{dc} = 240\,V$) despite the increase in SoC and the terminal voltage of the battery over time during the charging process. The reference V_{dc} is compared with the actual V_{dc}, and the error (difference) is processed through a PI controller. A mathematical function block derived from the electrical characteristics of the battery is used to produce the appropriate duty ratio for the charging action. The inputs to the block are battery SoC, current injected into the DC bus (i.e. $I_{dc(pv)}$) and the output of the PI controller. The output duty ratio is then converted to an equivalent PWM signal G_{10} to trigger the action of the series IGBT switch of the bidirectional converter. A mathematical model to explain how the duty ratio is generated by exploiting a mathematical model of the battery is discussed below.

Ignoring battery charge dynamics, thermal and ageing effects, a battery can be modelled such that the battery EMF (E_{bat}) is a function of SoC and has the following relationship [44]:

$$E_{bat} = E_{bat(max)}(SoC - \beta(1 - SoC)) \tag{3.27}$$

where, SoC is the ratio of current charge capacity to rated battery capacity, $E_{bat(max)}$ is the maximum battery EMF when fully charged, and β is a constant whose value lies between 0 and 1 and decides the droop in battery voltage with charge.

Let, $R_{bat(chg)}$ represent the battery charging resistance which is typically lower than its discharging resistance. Then, the battery terminal voltage (V_{bat}) can be related to the battery EMF E_{bat} and charging current ($I_{bat(chg)}$) using the following relationship.

$$V_{bat} = E_{bat} + I_{bat(chg)}R_{bat(chg)} \tag{3.28}$$

Since V_{bat} and $I_{bat(chg)}$ are the output voltages and currents of the bidirectional converter during boost mode operation, substituting $V_{bat} = d_{3(buck)}V_{dc}$ and $I_{bat(chg)} = \frac{I_{dc(pv)}}{d_{3(buck)}}$ in (3.28) and solving we get the equation quadratic in $d_{3(buck)}$ as:

$$V_{dc}d^2_{3(buck)} - E_{bat}d_{3(buck)} - I_{dc(pv)}R_{bat(chg)} = 0 \tag{3.29}$$

On solving ((3.29) and considering only positive solution,

$$d_{3(buck)} = \frac{E_{bat} + \sqrt{E^2_{bat} + 4V_{dc}I_{dc(pv)}R_{bat(chg)}}}{2V_{dc}} \tag{3.30}$$

(3.13), (3.27) and (3.30) are the equations which are realised inside the duty generator block for battery charging mode to produce the appropriate duty ratio. The duty ratio thus generated ensures a constant DC bus voltage, as well as a steady and safe battery voltage when the battery is charging.

3.3.3 Sensorless Speed Control

A. Sensorless Commutation

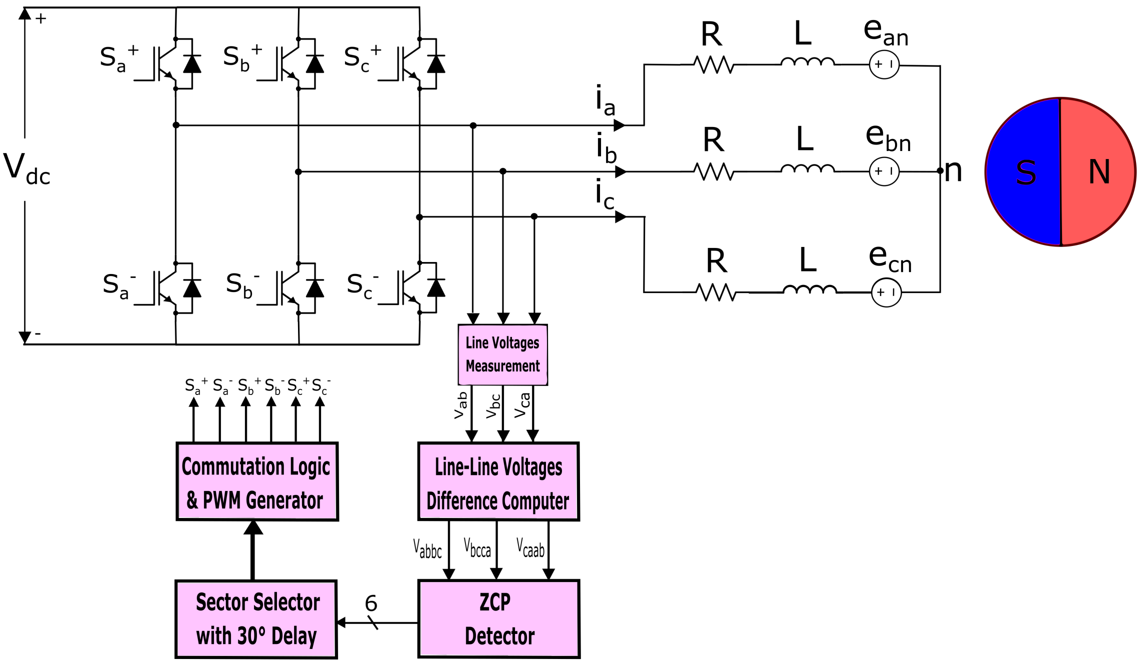

Figure 3.7: Schematic of proposed sensorless commutation of BLDC motor drive

In this research, we propose a straightforward method to estimate the rotor position by detecting the ZCPs of the trapezoidal (ideal) BEMFs induced across the stator windings for a three-phase star-connected permanent magnet BLDC motor. Figure 3.7 presents the schematic of the proposed sensorless commutation method. The method does not require neutral potential, since it involves measurement of the line voltages instead of the phase voltages and estimates the BEMF with respect to the negative terminal of the DC source. Also, the method is easy to implement since it does not involve mathematical steps like derivatives or integrations. Unlike suggested in [37], the use of low-pass filters is not required, since the ripples in the BEMF waveforms are mitigated by utilising PWM switches (IGBTs) with Snubbers. The filters would otherwise introduce some considerable delay and, therefore, the system would require compensation for those delays introduced. The proposed model requires the introduction of a 30° commutation delay for a phase current right after the zero-crossing instant of the respective phase back-EMF. Also, a relatively very small delay should be introduced by the sample and hold circuit for zero-crossing detectors to perform as needed. However, the effect of these very small delays is later neutralised while introducing the 30 ° phase commutation delay.

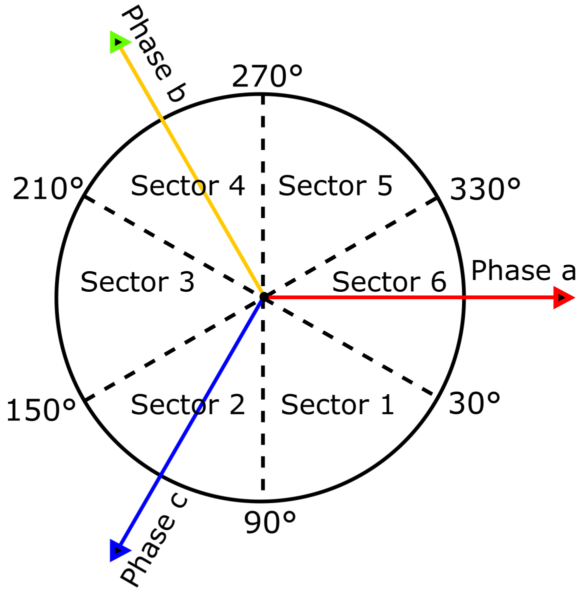

Figure 3.8: Segmentation of the circular path described by rotor

Figure 3.8 shows the 60 ° segmentation of the circular path described by the rotor, which is useful in locating the actual rotor position. Figure 3.9 describes the ideal waveforms of the motor line/phase current and the phase BEMFs against the different rotor angles. The figure also illustrates the inverter switches to be turned on following different segments describing the position of the rotor.

From the equivalent circuit of the stator windings shown in Figure 3.7, the stator phase voltage equations can be expressed as

$$\begin{bmatrix} v_{an} \\ v_{bn} \\ v_{cn} \end{bmatrix} = \begin{bmatrix} R & 0 & 0 \\ 0 & R & 0 \\ 0 & 0 & R \end{bmatrix} \begin{bmatrix} i_a \\ i_b \\ i_c \end{bmatrix} + \begin{bmatrix} L & 0 & 0 \\ 0 & L & 0 \\ 0 & 0 & L \end{bmatrix} \frac{d}{dt} \begin{bmatrix} i_a \\ i_b \\ i_c \end{bmatrix} + \begin{bmatrix} e_{an} \\ e_{bn} \\ e_{cn} \end{bmatrix} \tag{3.31}$$

where, v_{an}, v_{bn} and v_{cn} are the three-phase to neutral voltages, i_a, i_b and i_c are the stator phase currents, e_{an}, e_{bn} and e_{cn} are the phase to neutral BEMFs, R

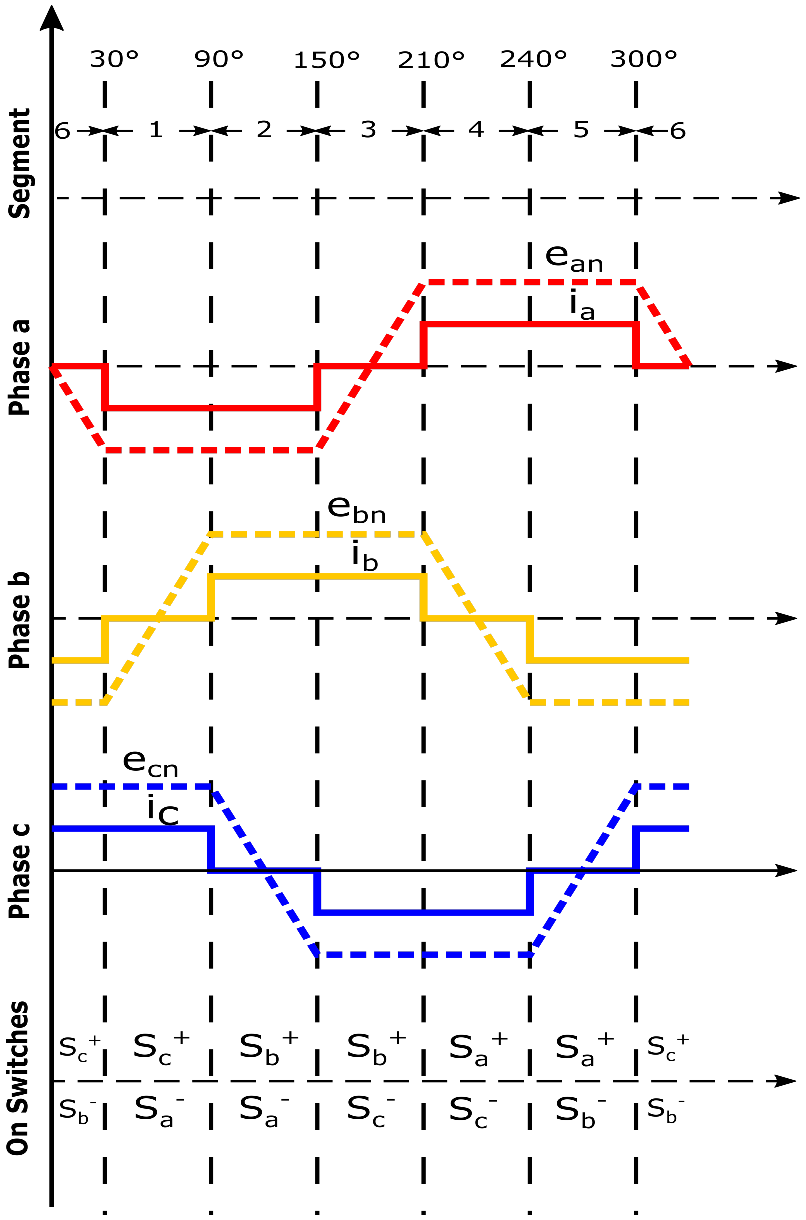

Figure 3.9: Ideal line current and BEMF waveforms of BLDC motor

is the stator phase resistance and L is the phase inductance. Using (3.31) and subtracting v_{bn} from v_{an}, v_{cn} from v_{bn} and v_{an} from v_{cn} gives the following line voltage equations:

$$v_{ab} = v_{an} - v_{bn} = R\left(i_a - i_b\right) + L\frac{d\left(i_a - i_b\right)}{dt} + e_{an} - e_{bn} \tag{3.32}$$

$$v_{bc} = v_{bn} - v_{cn} = R\left(i_b - i_c\right) + L\frac{d\left(i_b - i_c\right)}{dt} + e_{bn} - e_{cn} \tag{3.33}$$

$$v_{ca} = v_{cn} - v_{an} = R\left(i_c - i_a\right) + L\frac{d\left(i_c - i_a\right)}{dt} + e_{cn} - e_{an} \tag{3.34}$$

Subtracting (3.33) from (3.32), (3.34) from (3.33) and (3.32) from (3.34), yields the following equations:

$$\begin{aligned} v_{abbc} &= v_{ab} - v_{bc} \\ &= R\left(i_a - 2i_b + i_c\right) + L\frac{d\left(i_a - 2i_b + i_c\right)}{dt} + e_{an} - 2e_{bn} + e_{cn} \end{aligned} \tag{3.35}$$

$$\begin{aligned} v_{bcca} &= v_{bc} - v_{ca} \\ &= R\left(i_b - 2i_c + i_a\right) + L\frac{d\left(i_b - 2i_c + i_a\right)}{dt} + e_{bn} - 2e_{cn} + e_{an} \end{aligned} \tag{3.36}$$

$$\begin{aligned} v_{caab} &= v_{ca} - v_{ab} \\ &= R\left(i_c - 2i_a + i_b\right) + L\frac{d\left(i_c - 2i_a + i_b\right)}{dt} + e_{cn} - 2e_{an} + e_{bn} \end{aligned} \tag{3.37}$$

Consider the time interval throughout which the rotor lies in sector 6. From Figure 3.9, it can be observed that during this time interval, $e_{bn} = -e_{cn}$, $i_b = -i_c$ and $i_a = 0$ while e_{an} transitions from a negative value to a positive value crossing zero. This condition occurs when phase c is connected to the positive terminal of the DC source, phase b is connected to the negative terminal of the DC source, while phase a is kept open. Thus, when the rotor is in sector 6, (3.37) can be reduced to (3.38) as

$$v_{caab} = -2e_{an}, \quad for\ \theta \in\ Sector\ 6\ and\ Sector\ 3 \tag{3.38}$$

The condition described by (3.38) also holds when the rotor lies in sector 3. However, during this time interval, e_{an} transitions from a positive value to a negative value, crossing zero as connections to phases b and c are reversed. Similarly, (3.35) can be reduced to (3.39) when the rotor lies in sectors 1 and 4. Also, (3.36) can be reduced to (3.40) when the rotor lies in sectors 2 and 5.

$$v_{abbc} = -2e_{bn}, \quad for\ \theta \in\ Sector\ 1\ and\ Sector\ 4 \tag{3.39}$$

$$v_{caab} = -2e_{an}, \quad for\ \theta \in\ Sector\ 2\ and\ Sector\ 5 \tag{3.40}$$

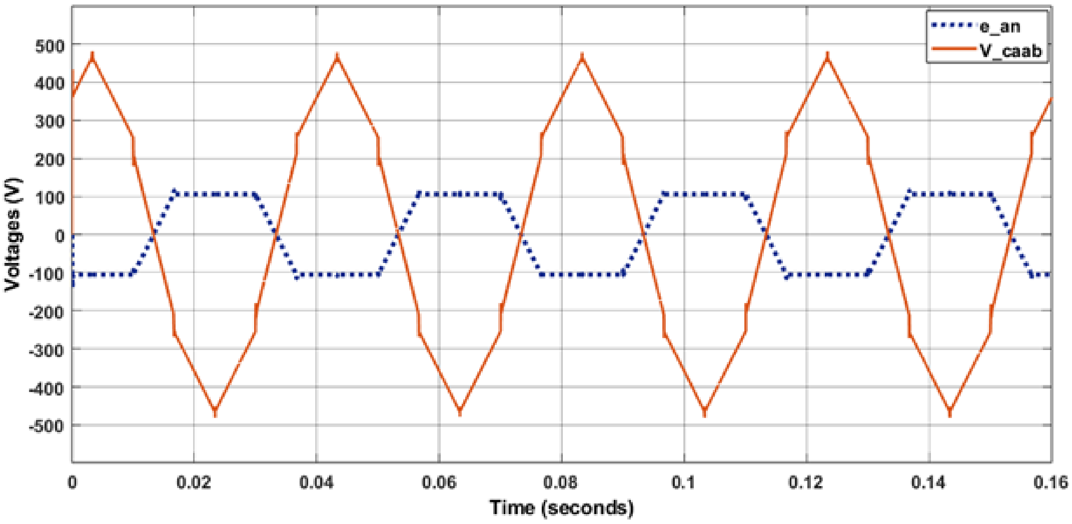

Figure 3.10: Line-line voltage difference V_{caab} and back-emf e_{an}

Therefore, the BEMF waveform of each phase crosses zero twice in an electrical cycle. Further, from (3.38) - (3.40), it can be concluded that during the commutation intervals, the line-to-line voltage difference is of the opposite polarity to the corresponding BEMF undergoing transitions and is scaled by a factor of 2. These relations have been validated using the waveforms of v_{caab} and e_{an} as presented in Figure 3.10 and are applied afterwards to accurately decide the rotor position and generate appropriate switching signals. Table 3.4 presents the future rotor position information in terms of sectors based on the zero-crossing detection of line-line voltage differences and the corresponding switching states to be applied after a 30° electrical interval. The symbols $\uparrow$ and $\downarrow$ are used to denote the zero-crossings when a line-line voltage difference transitions from negative to positive polarity (positive zero-crossing) and from positive to negative polarity (negative zero-crossing), respectively.

In this way, the information of zero-crossing of any line-voltage difference is availed to produce the correct combination of switching pulses for the inverter. However, the rate at which these pulses are generated should adapt to the speed of the rotor otherwise, the system might become unstable due to loss in synchronization of switching frequency with motor speed. Therefore, the motor requires a dynamic adjustment of the switching delay period as per rotor speed. For instance, during the starting period, the pulse width of both stator currents and BEMFs are longer, indicating low speed (frequency), which gradually gets shorter with time as the motor speeds up, indicating an increase in switching frequency. This requirement for dynamically adapting to the changing speed is met by incorporating a time delay adjustable as per the measured speed.

Table 3.4: Rotor position estimation and switching states

Zero-crossing line-line voltage difference	**Next Rotor Position (after 30° delay)**	**Next Switches to turn on (after 30° delay)**
v_{caab} (↓)	Sector 1	S_c^+, S_a^-
v_{abbc} (↑)	Sector 2	S_b^+, S_a^-
v_{bcca} (↓)	Sector 3	S_b^+, S_c^-
v_{caab} (↑)	Sector 4	S_a^+, S_c^-
v_{abbc} (↓)	Sector 5	S_a^+, S_b^-
v_{bcca} (↑)	Sector 6	S_c^+, S_b^-

B. Speed Control

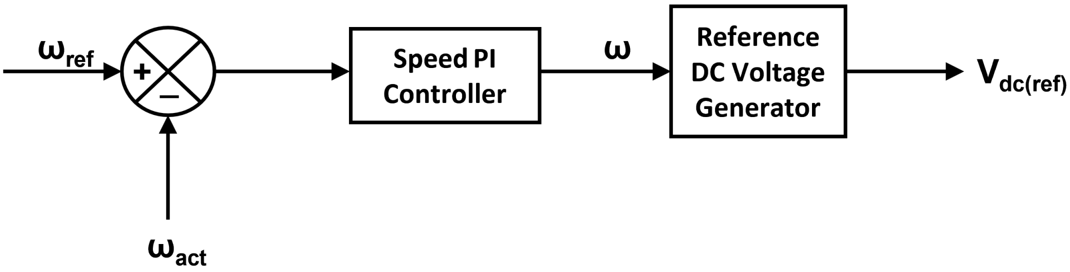

Figure 3.11: Closed loop speed controller

Speed control of the BLDC motor is achieved through the armature voltage control method applicable to a wide speed range below base speed. A closed-loop speed controller shown in Figure 3.11 is used to attain any speed below the rated (base) speed of 1500 rpm. The actual speed can be measured either directly through speed sensors or indirectly by counting the number of BEMF pulses that have passed per unit time. Thus, the information of rotor positions with respect to time is sufficient to compute the motor speed without requiring any physical speed sensors. The desired (reference) speed is compared with the actual (measured) speed, and the resulting error is processed through a PI controller. The output signal of the PI controller is used by a reference DC voltage generator which is a mathematical function block that contains equations describing the mathematical model of the motor drive system. The controller acts to reduce the difference between the reference speed and the actual speed so as to reach a steady state with the desired motor speed in the minimum time possible. The output of the controller at a steady state is the reference DC bus voltage ($V_{dc(ref)}$), which serves as the input to DC-link voltage controller during battery discharging operation.

The fundamental steady-state voltage equation for a DC motor is expressed as:

$$V_{dc} = E_{eq} + IR_{eq} \tag{3.41}$$

where, E_{eq}, I and R_{eq} represent the average back-emf, DC motor current and effective resistance. Since at any time instant, any two of the three phases are conducting, $R_{eq} = 2R$ where R is the resistance per phase. Also, the average back-EMF is related to the angular speed by the relation $E_{eq} = k_m\omega$. The EMF constant k_m is defined by considering the back EMFs across two phases. On substituting in (3.41), we get,

$$V_{dc} = k_m\omega + 2IR \tag{3.42}$$

In our case, the load torque being considered is a friction torque (speed proportional component), which is a purely passive torque. Consideration of traction torques (gravitational torques), useful in the study of regenerative braking, lies outside the scope of this research and is thus ignored. Thus, in balanced condition, ignoring all sorts of losses, where developed torque (τ_{dev}) is equal to load torque (τ_{load}) following relations hold:

$$\begin{aligned} \tau_{dev} &= \tau_{load} \\ \text{or, } k_m I &= B\omega \\ \text{or, } I &= \frac{B\omega}{k_m} \end{aligned} \tag{3.43}$$

where, B is the coefficient of friction that defines the load torque acting on the shaft of the motor. Substituting I from (3.43) to (3.42), we obtain,

$$V_{dc} = \omega(k_m + \frac{2BR}{k_m}) \tag{3.44}$$

The mathematical block generates the reference voltage for the inner voltage control loop, exploiting the relations between DC link voltage and angular speed of the motor described by (3.44).

CHAPTER FOUR: SIMULATIONS

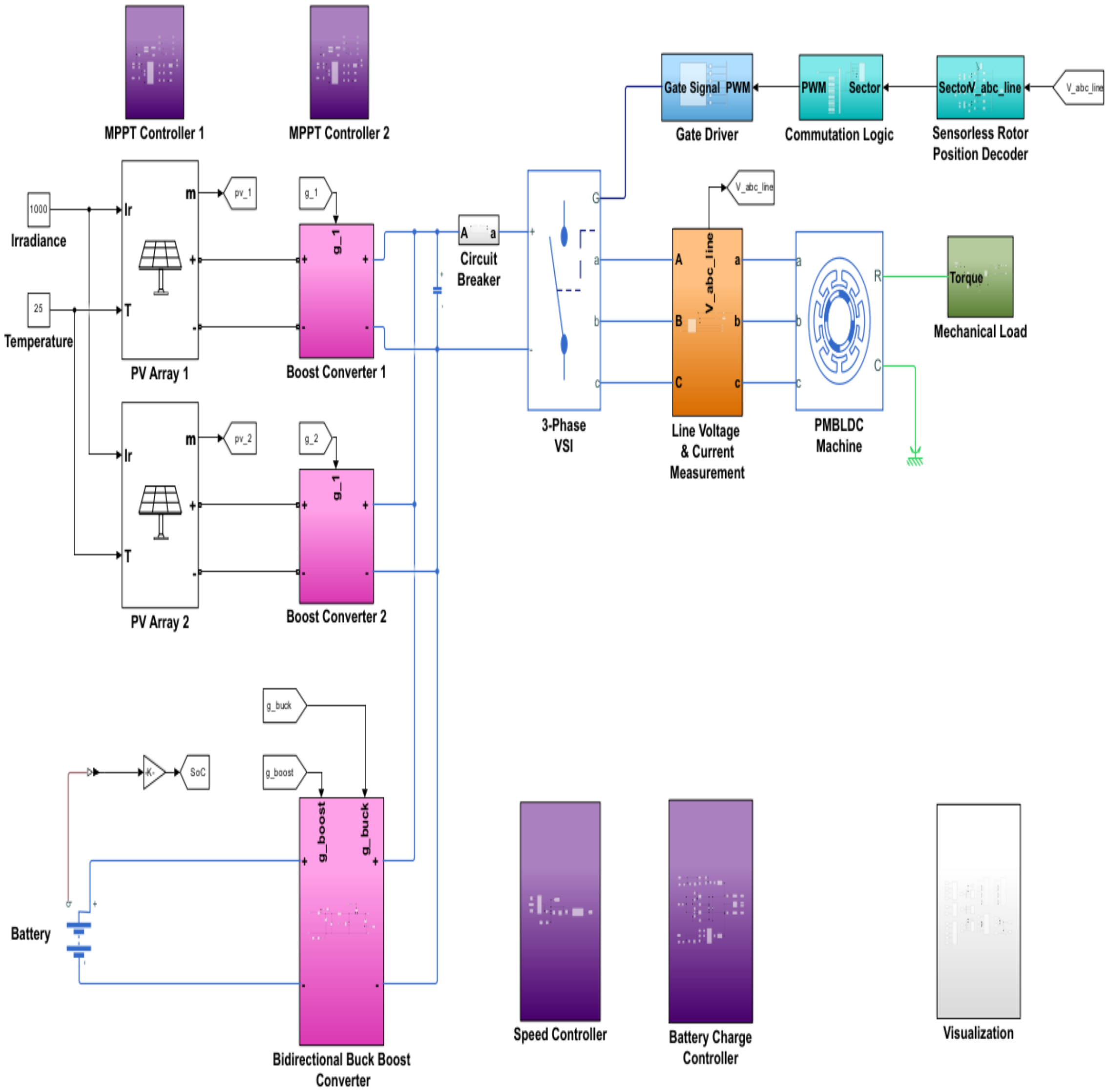

Figure 4.1: Simulink model of overall System

Simulations of the proposed model were done in the MATLAB Simulink environment. The effectiveness of the presented system model was tested by splitting the entire model into several subsystems and blocks and observing their individual performance and behaviour. Once the performance described by the outputs of the individual block and subsystem met the required standards, the block/subsystem was integrated into the main model. All the parameters required for the major components like BLDC motor, battery bank, SPV array units, DC-DC converters, VSI were set as per the design calculations and assumptions done in Section 3.2 to accurately examine the performance and working of the overall model. Furthermore, the validation of control techniques introduced in Section 3.3 was tested by simulating them exactly in the form described. An emphasis was placed on studying the behaviour of the system under different circumstances to examine the robustness and flexibility of the system. Figure 4.1 shows the overall Simulink model designed according to the proposed architecture.

4.1 SPV Array and MPPT Control Models

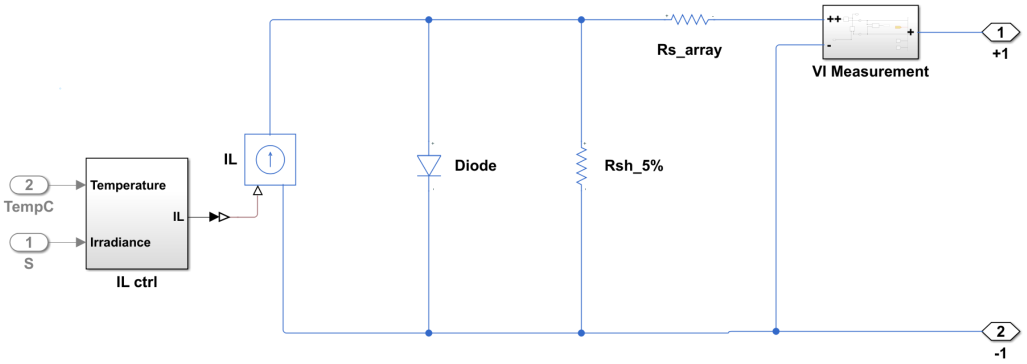

Figure 4.2: Simulink model of SPV array unit

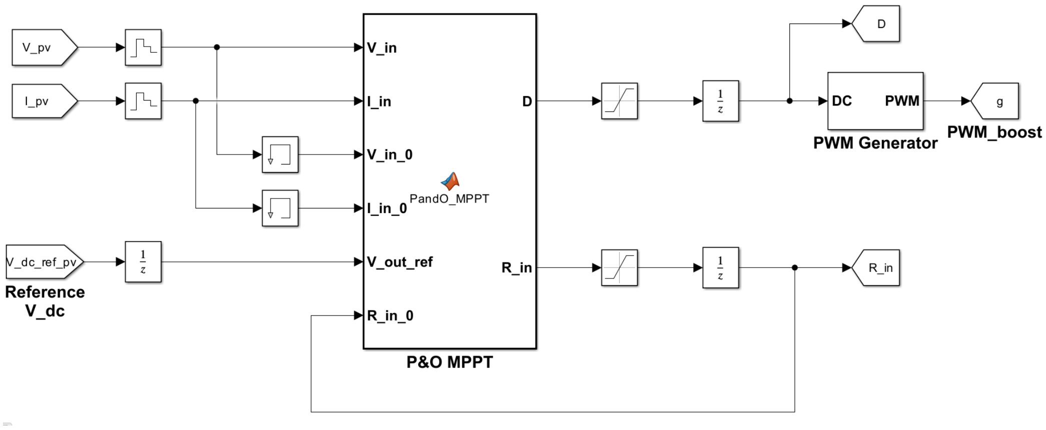

Figure 4.3: Simulink model of MPPT Controller

The SPV array model used for the simulation is shown in Figure 4.2. The model was designed according to the specifications described in Table 3.3. The inputs to the array model were temperature (in $^{\circ}C$) and irradiance (in Wm^{-2}). The outputs were voltages and currents fed to the DC bus through a boost converter. The duty ratio for the boost converter required to ensure MPP operation was generated through the MPPT control model shown in Figure 4.3. Array currents and voltages were sampled, and measurements were passed to the MPPT block at discrete time intervals through zero-order hold blocks. For computing changes in voltage, power, and input resistance, their previous values need to be stored in the memory. As displayed in the figure, the block executes VOR based P&O MPPT algorithm to output a suitable duty ratio. It also accepts a reference DC voltage generated by the speed controller block to adjust the duty ratio (or input resistance) instead of taking the actual DC bus voltage. This enables quick settlement of the DC bus voltage during load fluctuations to the desired level and also reduces the dependency of the SPV array units on the battery.

4.2 DC Bus Voltage Control Model

As can be observed in Figure 4.4, the DC bus voltage controller model works in integration with the battery charge controller to decide its mode of operation. The battery charge controller takes the measured SoC of the battery as input and compares it with the predefined upper and lower permissible limits of SoC to decide whether to charge or discharge the battery. The two antiparallel NOT gates are for resetting the other switch when one of the switches is triggered due to SoC touching the predefined limit. The design enables the complementary action of the shunt and series switches used in the bidirectional converter and ensures that neither of them is turned on simultaneously.

In simulation time, the DC link voltage controller subsystem for discharging mode took the desired DC bus voltage generated by the outer speed controller subsystem as reference input and the actual DC bus voltage measured through the voltage sensor as feedback. It then computed the required duty ratio based on the output of the voltage PI controller 1 and the battery terminal voltage that it received as the additional input. Based on the duty ratio, the PWM signals required for the boost operation of the bidirectional converter were generated. The signal was ANDed with one of the control signals from the battery charge controller and served as gate pulses to the shunt switch of the bidirectional converter.

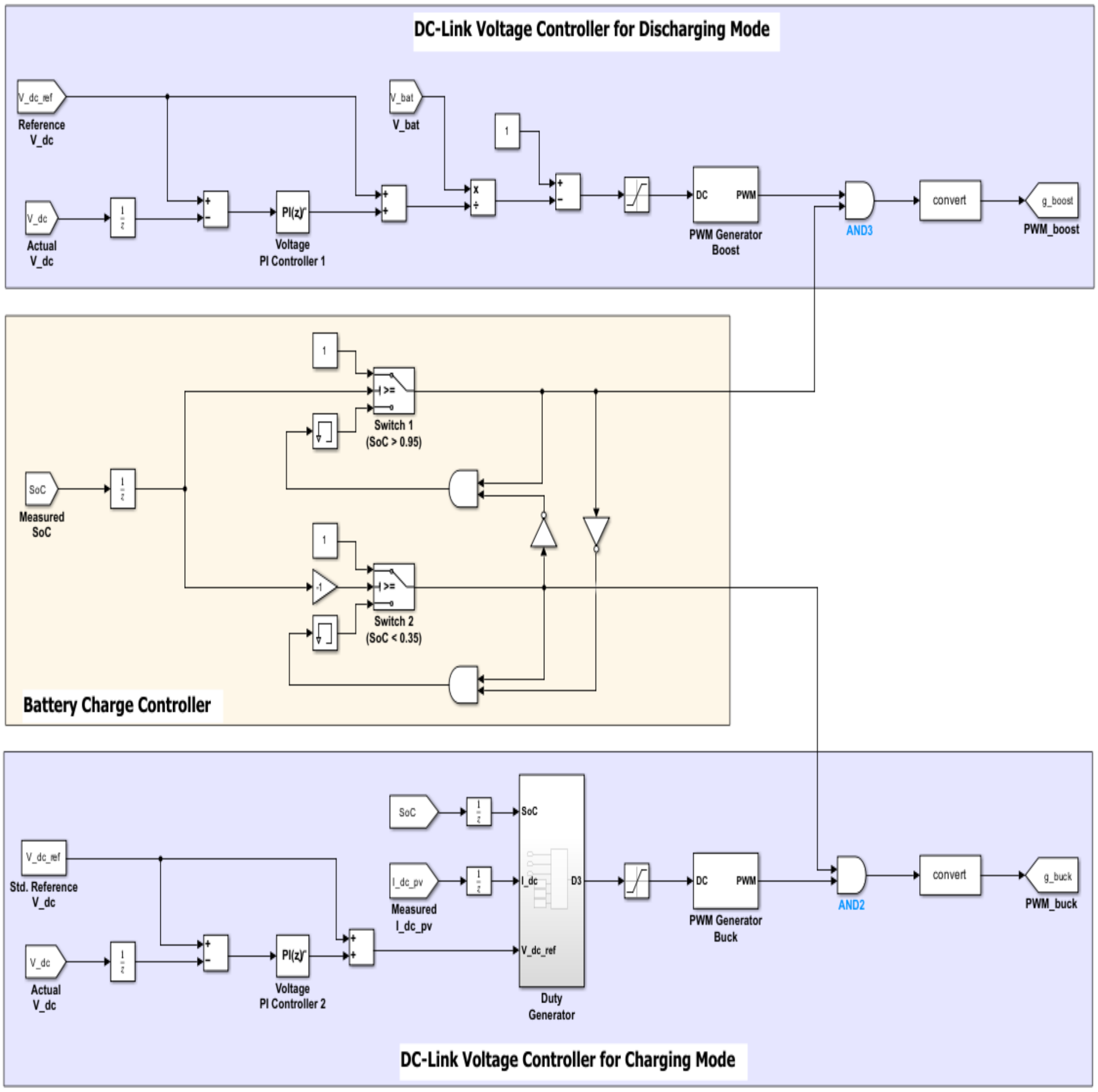

Figure 4.4: Simulink model of DC bus voltage controller

The operation of the DC link voltage controller subsystem for the charging mode was almost similar to that for discharging mode. However, it took additional inputs such as the DC-bus current and SoC of the battery. Also, the reference was set to a fixed standard value of 240 V. As a battery cannot endure varying voltage at its terminals, it is necessary to suppress voltage fluctuations caused by changes in solar power or sudden disconnection of the motor. To meet such a requirement, a precise mathematical model of the battery that described its electrical characteristics was realised in the duty generator block so as to produce the appropriate duty ratio, and thereafter the PWM signals for the buck mode operation of the bidirectional converter were generated. Again, this signal was ANDed with the other control signal before using it as gate pulses to trigger the series switch of the converter.

4.3 Sensorless Speed Control Model

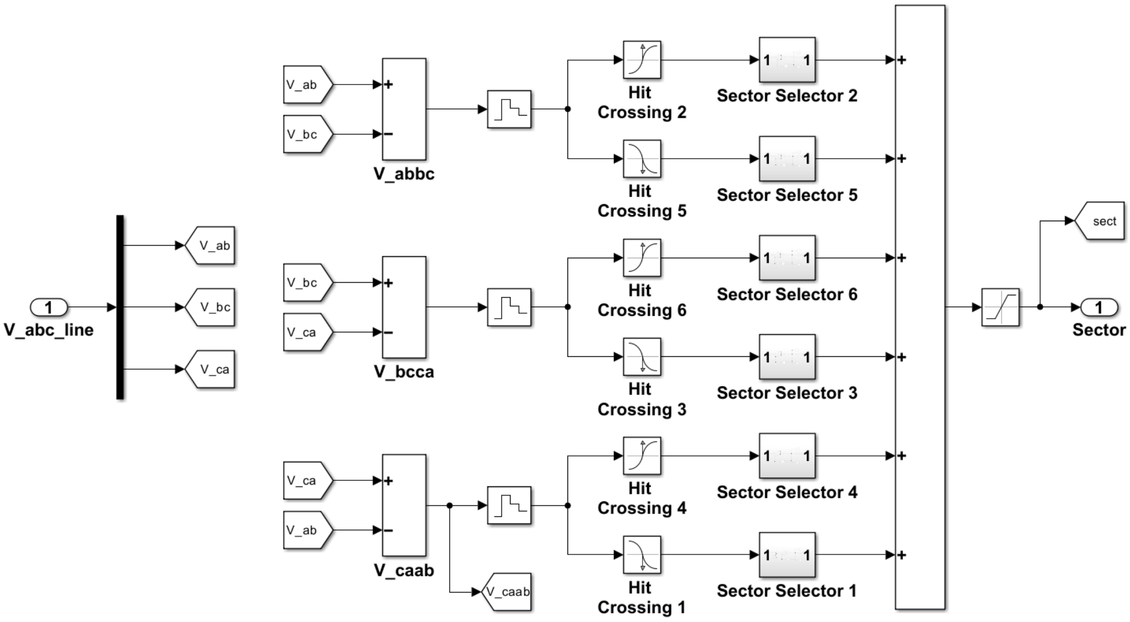

Figure 4.5: Simulink model of BEMF ZCPs detector and rotor segment selector

The motor parameters selected for simulating and testing the proposed model for sensorless speed control are mentioned in Table 3.1. Figure 4.5 presents the Simulink model to realise sensorless commutation. First, the line terminal voltages were measured, and their differences were sampled and fed to the zero-crossing detectors. Each zero-crossing detector senses the ZCPs (positive and negative) and generates pulses. Each of the six different ZCPs is uniquely associated with a sector that defines the current and next (after 30°) rotor positions. Based on the next rotor position defined by the sector selector block and according to Table 3.4, the pulse generator generated the required switching pulses. These switching pulses served as PWM pulses to drive the inverter. The mechanism of dynamically adjusting the time delay for selecting and holding a particular sector was implemented inside the sector selector blocks by taking the measured speed as feedback. This ultimately framed a closed-loop system, thereby making position-sensorless speed control possible.

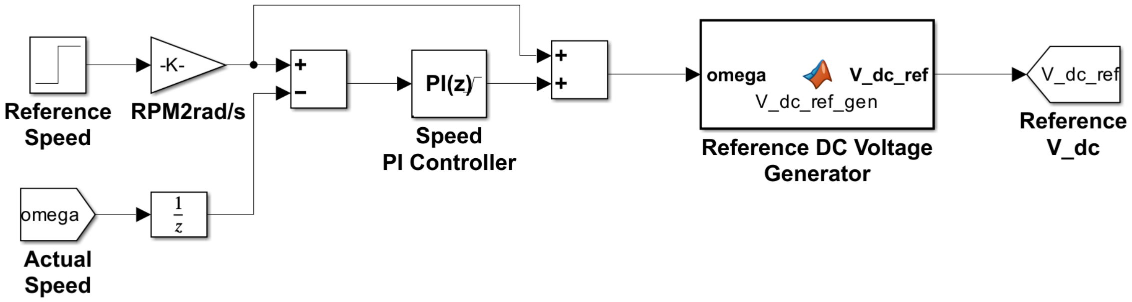

Figure 4.6: Simulink model of speed controller

The Simulink model of the BLDC motor speed controller is shown in Figure 4.6. It is a closed-loop PI based controller. Compared to the DC-bus voltage controller, this controller is slow-acting. It serves by setting a reference DC-link voltage for the inner voltage controller loop that is functional during battery discharge mode. The desired motor speed was compared with the actual speed to generate an error signal, which was then handled by the PI controller. The PI controller's command was a speed signal. The reference DC voltage generator block used was a mathematical block that related the speed of the motor to its armature voltage and resulted in the desired DC-link voltage.

CHAPTER FIVE: RESULTS

5.1 MPPT Control

The effectiveness of the MPPT control model of the SPV arrays was tested against varying working conditions (temperature and irradiance). Since both array units belonged to the same SPV model, shared the same control architecture, but differed only in size, the study of the output of only one unit was sufficient to test the validation of the model. To effectively test the model, its performance was evaluated first under varying irradiance and then under varying temperature. In both cases, the motor was operated at full load with the rated speed. Since changes in irradiance and temperature are naturally slow processes, their impact on the SPV parameters was studied by choosing a relatively longer simulation time.

5.1.1 Irradiance Variation

Keeping the temperature of the SPV arrays constant, irradiance (Irr) was varied in 3 phases for different time durations. Figure 5.1 shows the impact of varying irradiance on the performance of the system in terms of different output parameters such as (b) voltage (V_{pv}), (c) current (I_{pv}) and (d) power (P_{pv}). The dashed lines indicate the reference MPP output parameters, which were evaluated based on the SPV inputs (irradiance and temperature) and its mathematical model. The solid lines indicate the actual outputs. In the first phase (from $t = 0\,s$ to $t = 50\,s$), the irradiance is set at its standard level of $1000\,Wm^{-2}$. In the second phase (from $t = 50\,s$ to $t = 150\,s$), the irradiance is reduced to $600\,Wm^{-2}$ and then increased to $800\,Wm^{-2}$ in the third phase (from $t = 150\,s$ to $t = 250\,s$). Since the system was initialised from a point very close to the MPP at $1000\,Wm^{-2}$ and $25\,°C$, the controller took no time to track the optimal power point from the very beginning. From the figure, it is evident that the controller can quickly respond to any changes in irradiance and track the shift in MPP with negligible errors. The figure reports a negligible impact of irradiance variation on output voltages; however, changes in current and, thus, on power are considerable.

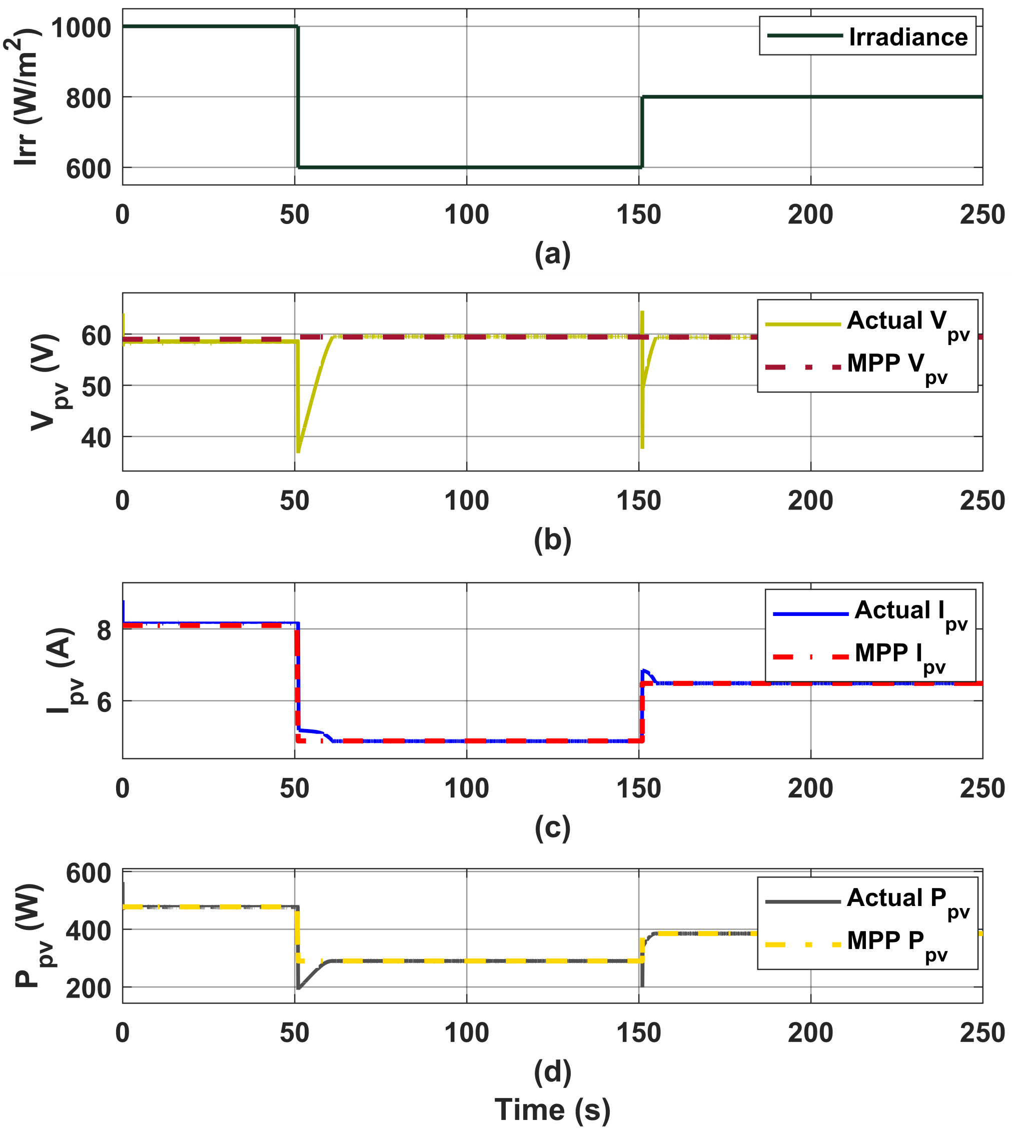

Figure 5.1: SPV array outputs under variable irradiance: a) irradiance, b) voltage, c) current, and d) power vs time

5.1.2 Temperature Variation

The effect of temperature variation was also studied in 3 distinct phases of different time durations, keeping irradiance fixed at 1000 Wm^{-2} as shown in Figure 5.2. In the first phase (from $t = 0\,s$ to $t = 50\,s$), temperature is set to 25 $^\circ C$ and in each successive phases (from $t = 50\,s$ to $t = 150\,s$ and $t = 150\,s$ to $t = 250\,s$), the temperature is increased by 5 $^\circ C$. This leads to a noticeable decrease in solar voltage (V_{pv}) and power (P_{pv}) at each phase, although almost no change is reflected in terms of current (I_{pv}). Like irradiance variation, the controller is able to track any changes in temperature of the SPV array units

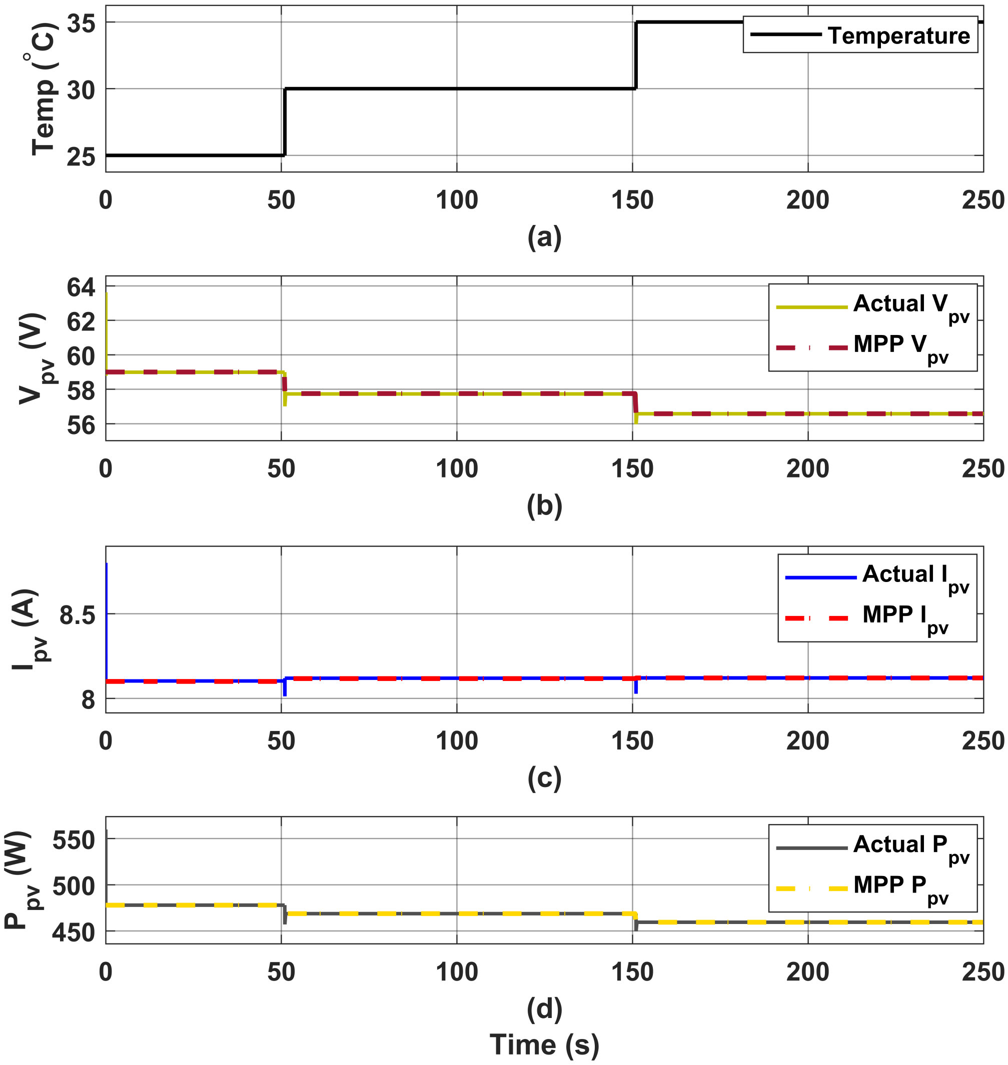

Figure 5.2: SPV array outputs under variable temperature: a) temperarture, b) voltage, c) current, and d) power vs time

in a very short time with minimal error. Moreover, the flat solid lines indicate almost no power oscillations while operating in the steady state. Thus, the effectiveness of the proposed MPPT model against power oscillations and rapid input fluctuations was endorsed by the results obtained.

5.2 Sensorless Speed Control

5.2.1 Sensorless Commutation

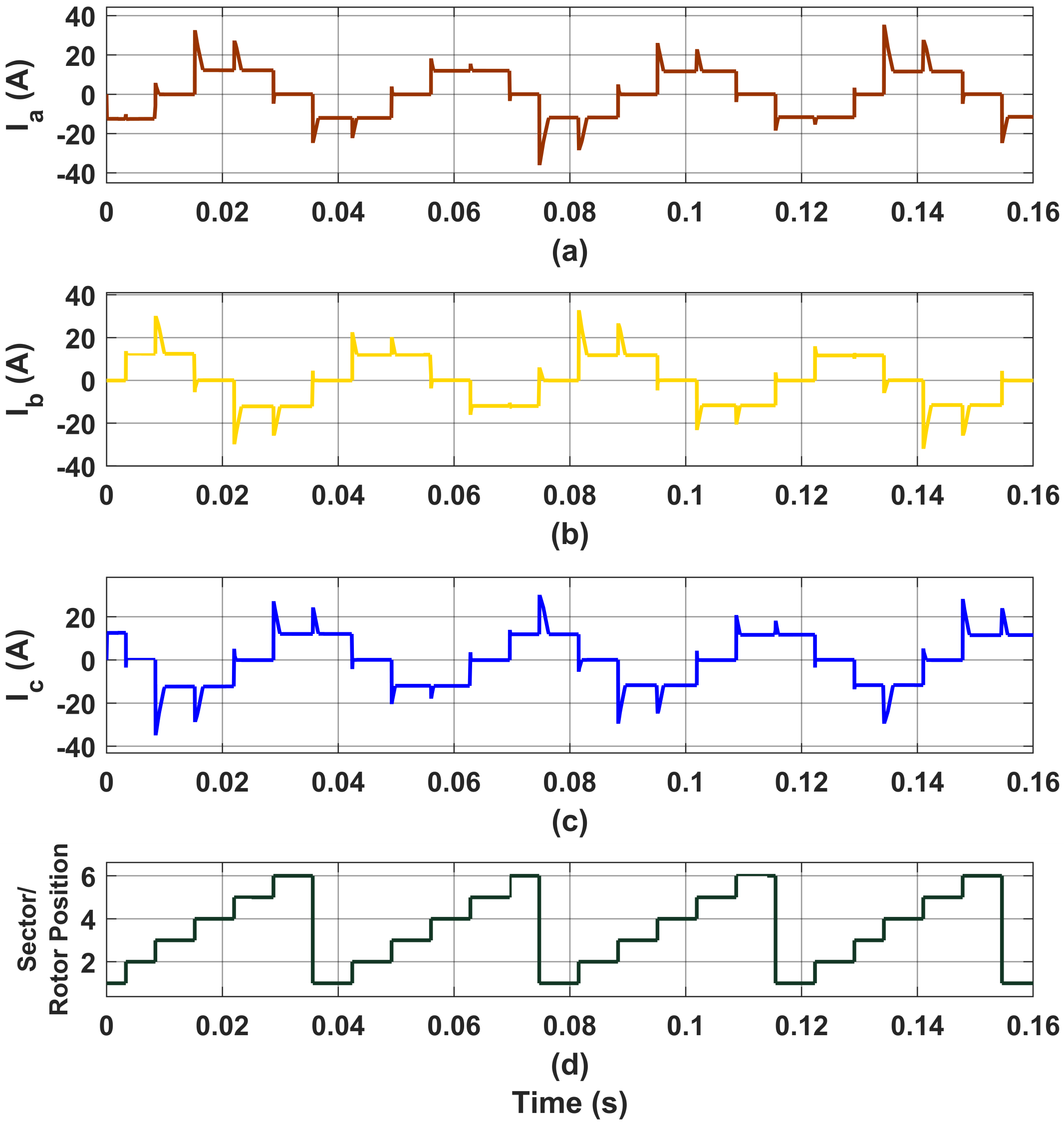

Figure 5.3: Commutation of motor: a) phase 'a' current, b) phase 'b' current, c) phase 'c' current, and d) rotor position vs time

Electronic commutation of the BLDC motor without using any position sensor was validated through its current and line voltage waveforms. These waveforms were generated during the steady state operation of the motor for the rated speed of 1500 rpm. Figure 5.3 presents the phase/line current waveforms and rotor positions in terms of sector number at different time intervals for a total time duration of 0.16 s (4 cycles). The phase currents roughly take the quasi-square wave shape and are mutually displaced by electrical 120 °. The ripple contents in the current, which depend on stator resistance, inductance, and switching frequency, are dominant during the commutation (or phase switching) instants. The figure shows that the phases are being switched in a sequence at the end of every sector, resulting in a successful commutation. The time gaps corresponding to every sector are uniform, implying a constant rotor speed. At rated speed, the motor draws an average source current of 11.8 A, which is evident from the flat-topped region of the current waveforms.

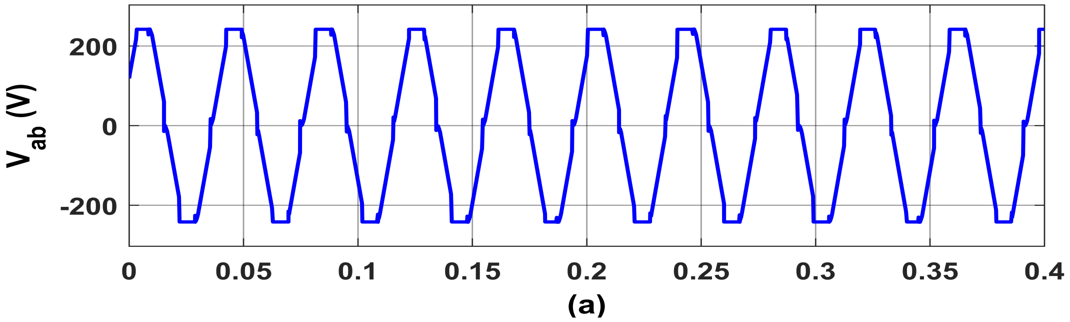

(a)

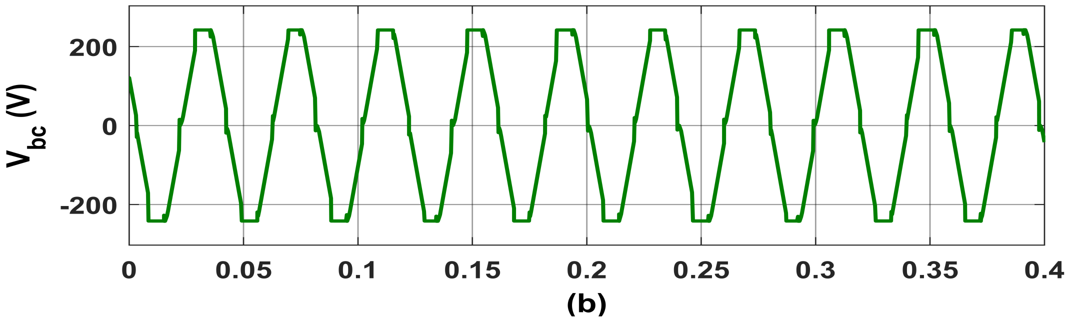

(b)

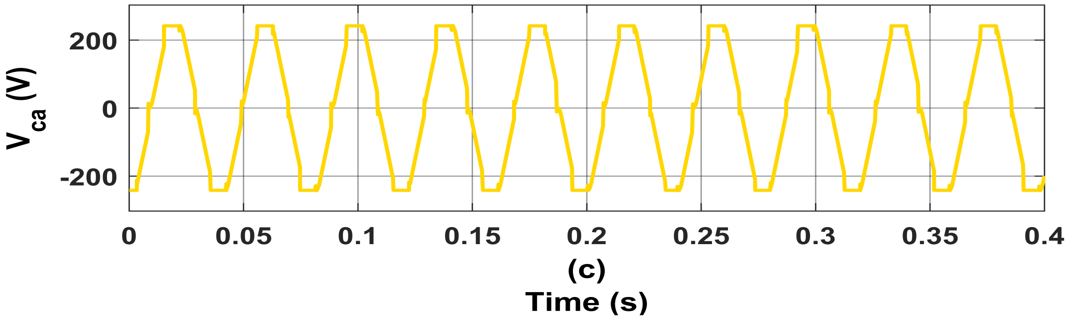

(c)

Figure 5.4: Commutation of motor: a) line voltage V_{ab}, b) line voltage V_{bc}, and (c) line voltage V_{ca} vs time

Figure 5.4 portrays the waveforms of the motor line voltages V_{ab}, V_{bc} and V_{ca}, for a total time duration of $0.4\ s$ (10 cycles), which were used in the detection of ZCPs of the back-EMFs. The shape of the line voltages is roughly trapezoidal, as expected, with a peak value of $240\ V$, same as the magnitude of the standard DC bus voltage for rated conditions. This is because any two out of the three phases keep conducting together for a duration of electrical $60\,^{\circ}$. In this duration, the full DC bus voltage appears across these two phases, resulting in a flat-topped region in the wave shape for a $60\,^{\circ}$ interval.

5.2.2 Speed Control

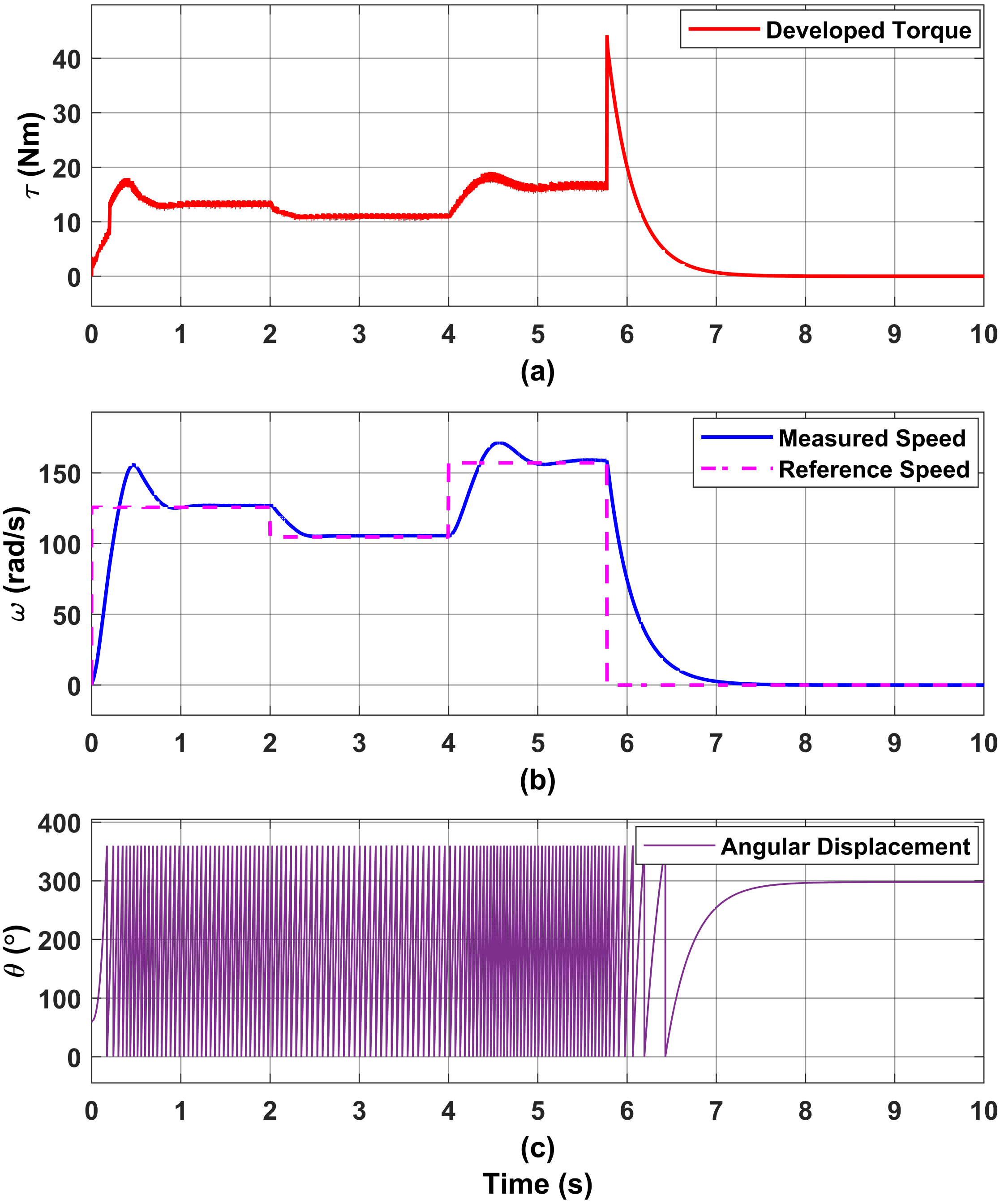

Figure 5.5: Motor mechanical outputs: a) torque b) speed, and c) angular displacement vs time

Keeping the irradiance and temperature of SPV arrays fixed at standard conditions, the speed control of the motor was realised. The results of the battery charging operation (with different phases of speed variations) and the discharging operation are demonstrated in a single frame in Figures 5.5 and 5.6. During the battery discharging mode, the motor was disconnected from the DC bus, and braking was applied to bring it to rest.

Figure 5.5 depicts the variations in mechanical outputs of the motor ((a)torque, (b) speed and (c) angular displacement) over time as per requirements. The dashed line in the speed vs. time curve indicates the reference speed set by the speed controller, whereas the solid line represents the actual speed. The reference speed is varied in three different stages, each with a span of 2 seconds. In the first phase (from $t = 0\,s$ to $t = 2\,s$), the motor reference speed is set to 1200 rpm ($\approx$ 126 rad/s). In the second phase (from $t = 2\,s$ to $t = 4\,s$), the speed is reduced to 1000 rpm ($\approx$ 105 rad/s). Again, in the third phase (from $t = 4\,s\ to\ t = 6\,s$), it increases to 1500 rpm ($\approx$ 157 rad/s). The actual speed clearly seems to be tracking the reference speed in all the cases within a very short time duration, thereby validating the effectiveness of the speed controller. The magnitude of the speed overshoot and undershoot depends on the range of variation. For example, the speed increment range is highest 1200 rpm in the first (starting) phase, and therefore the overshoot is maximum in this phase. The angular displacement (plot (c)) varies from 0 to 360° in each cycle as the motor runs, starting from 60° initial angular orientation of the rotor. The plot (a) represents the motor torque. The ripple content in the torque is due to ripples in the current, as the torque developed is directly proportional to the phase current magnitude. For a high-inertia motor, the ripple in the torque is not a problematic issue since it does not affect the speed much and thus has very little contribution to vibration and noise. However, for a low-inertia motor used, especially in position control, ripples in the torque may be a critical issue to address.

In the last phase of motor control ($t = 5.8\,s$ to $t = 10\,s$), the circuit is opened to isolate the motor from the DC bus and the braking torque is applied to quickly bring it to rest. This is demonstrated by the exponential decay in the rotor speed. Moreover, this is the instant when battery charging is initiated (because SoC reached its lower limit) and continued unless SoC reaches its maximum limit. In Figure 5.6, the variation in the magnitude of the motor line currents is demonstrated over time in different phases of speed control. In the initial starting phase, the line current magnitude is very high because of the low speed and high starting torque. The magnitude of the current waveforms gradually decreases as the motor gains speed due to an increase in BEMF that opposes the current. Also, it can be figured out that the width of the line current waveforms also reduces with increasing speed, indicating the synchronisation of the inverter switching frequency with motor speed. However, when the line currents at steady state for different motor speeds are relatively compared, then the magnitude and frequency of the line currents are found to increase with the increase in speed and vice versa.

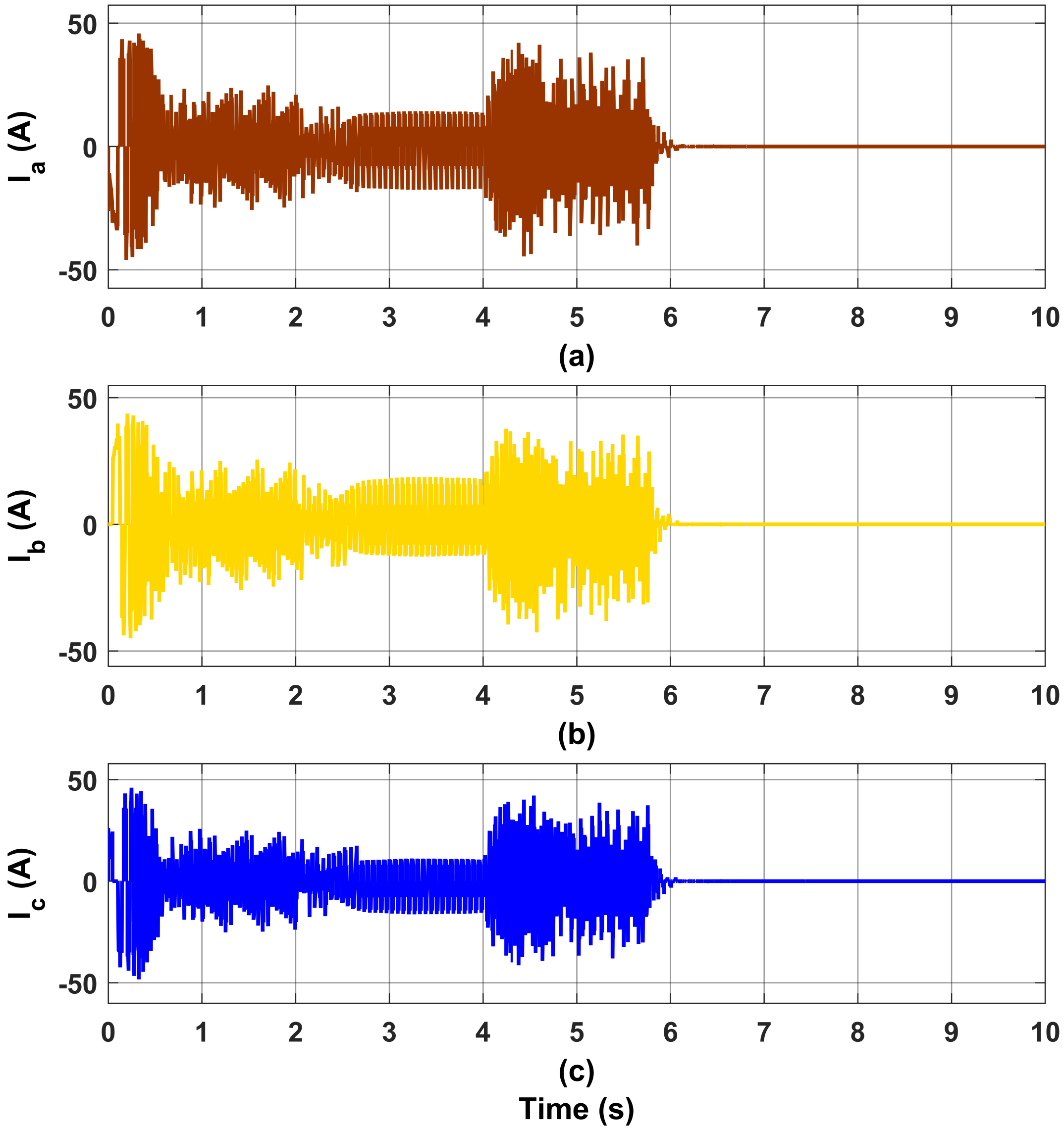

Figure 5.6: Motor line currents: a) phase ‘a’ current, b) phase ‘b’ current, and c) phase ‘c’ current vs time

5.3 DC-link Voltage Control

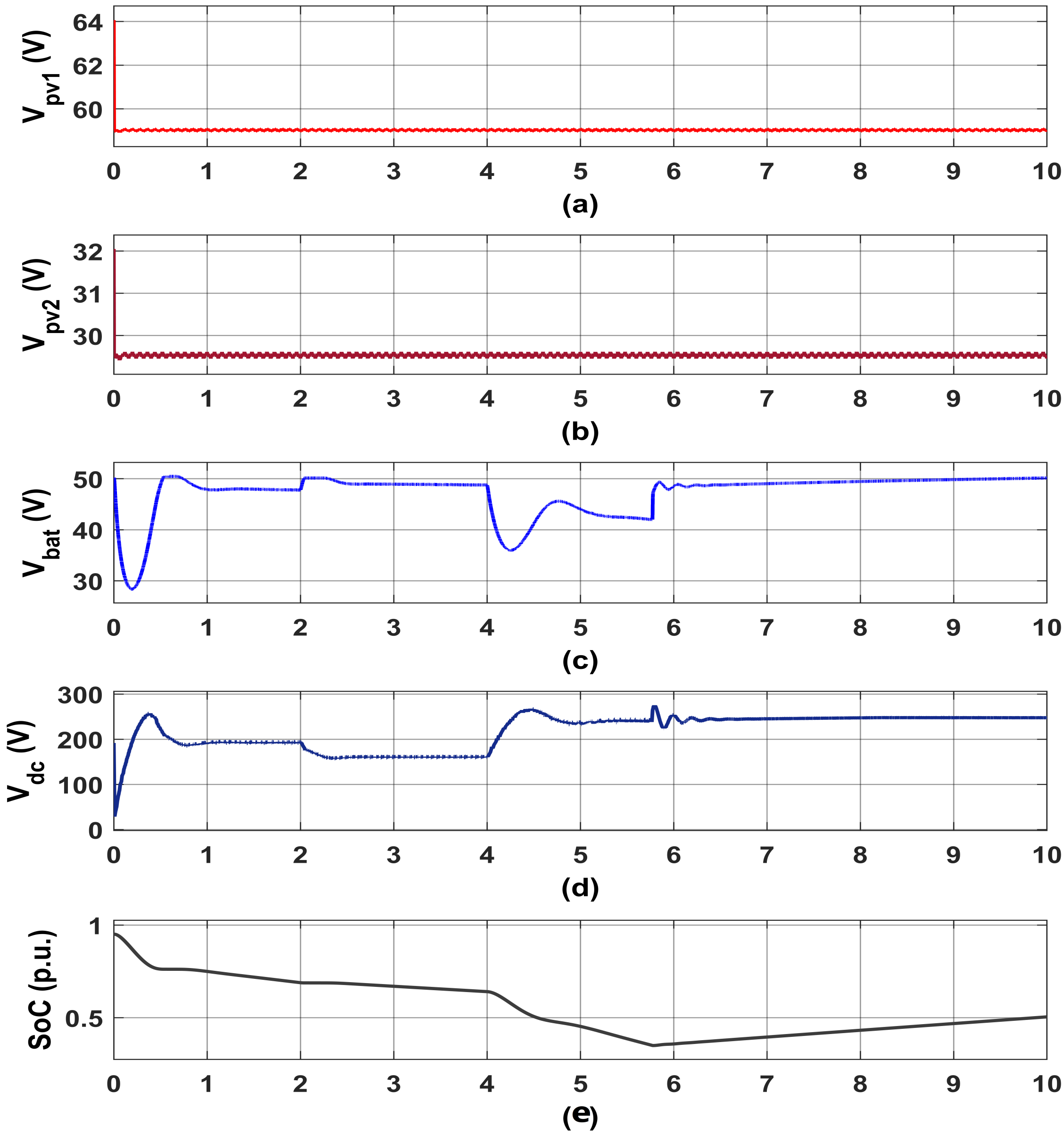

Figure 5.7: Voltages across different units: a) SPV array 1, b) SPV array 2, c) battery, and d) DC bus vs time; e) SoC vs time

Figure 5.7 illustrates the variation in voltages with respect to time across all major components such as SPV arrays, battery and DC link capacitor in addition to battery SoC throughout the battery discharging phase (speed control) and charging phase. In fact, to control the speed, adjustment of the DC bus voltage to a desired level is a must when following an armature voltage control approach. Thus, the figure depicts adjustment of the bus voltage proportional to the reference speeds indicated by the dashed line in Figure 5.5 (b) during battery discharge mode and to the standard voltage level of 240 V during battery charge mode. This was achieved through a DC link voltage controller. During discharge mode, from Figure 5.7, it is notable that although battery voltage (V_{bat}) and SoC declined over time, the controller, as expected, was able to maintain a fairly constant DC bus voltage level according to the speed requirement. This verifies the essence of the DC bus voltage controller. Besides, it should be noted that despite the changes in load conditions, the voltages across the SPV array units (V_{pv1} and V_{pv2}) were held constant. This implies that the MPP operation is always maintained by the respective MPPT controller despite variations in battery and load conditions. In addition, the reason for the large drop in battery voltage in the starting phase was due to the high starting current drawn by the motor, resulting in a high internal resistive drop (IR) of the battery. In fact, the drop is proportional to battery current, which in our case constituted roughly 80 % of the motor current. Thus, whenever the range in speed variation is high, the change in battery current is high, resulting in an overshoot/undershoot in battery voltage roughly proportional to that range.

The waveforms of the voltages in the last phase are associated with the battery charging mode. Some critical changes are made before switching to battery charging mode, which include motor disconnection, braking, and a change in reference DC voltage magnitude. Since the motor got isolated by the breaker, the current that was being fed by the SPV arrays to the motor diverted towards the battery to initiate battery charging. Thus, the converters, which initially were operating in parallel, started to operate in series with the reversal of current (power flow) in the battery and the bidirectional converter. This critical condition got reflected in the form of DC bus voltage oscillations that lasted for a few cycles starting at t = 5.8 s as shown in Figure 5.7 (d). Although these oscillations appear apparent, they actually contribute to the oscillation of the battery terminal voltage to a certain degree, which is not desirable. From the figure, it is evident that the voltage oscillations across both the DC bus and the battery during the transient phase were suppressed to a considerable extent, thereby justifying the appropriateness of the converter and controller design. The shape of the battery voltage curve is supported by the battery current curve, which is illustrated in Figure 5.8. The figure also describes the

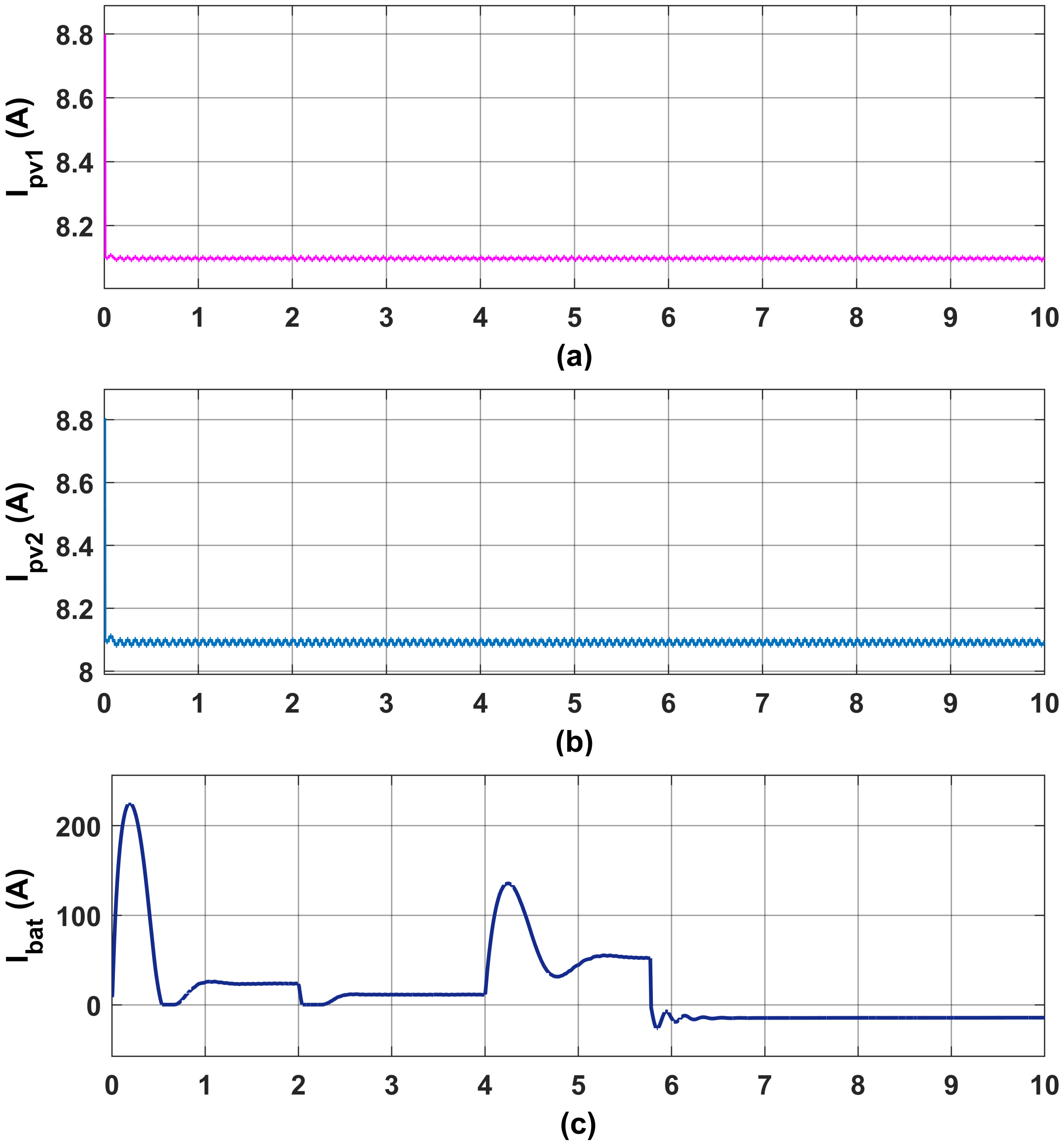

Figure 5.8: Current shared by different units: a) SPV array 1, b) SPV array 2, and c) battery vs time

current outputs of the array units and the total DC bus current over time for the different working phases discussed earlier. The high current requirement of the motor during the starting phase was met by the battery, which explains why the starting battery current was high. The peak inrush current of the motor typically ranges from 2 to 7 times the full load current. Figure 5.8 shows the full load battery current (at the standard operating condition of SPV arrays) to be around 44 A and the starting battery current to be around 250 A, which seems obvious theoretically. However, in practice, to deal with such high currents, thick conductors are required. This battery current can increase slightly more during low irradiance conditions or autonomous operation. The overshoots in battery currents can be lowered by gradually increasing the load, taking more time. The other way of reducing high starting current is to gradually increase the DC-link voltage instead of slamming the full voltage across the input terminals of the inverter. Regarding the currents of the array units, since the MPP operation is not affected by changes in load, the current profile remains fairly flat unless temperature and irradiance vary.

CHAPTER SIX: CONCLUSION

A model of the solar-powered BLDC motor drive, especially applicable to low-power electric vehicles, was presented, and its design and control methods were discussed in detail. The integration of two SPV array units and a battery bank with appropriately selected and designed DC-DC converters to power the motor at the required speed was validated. The simulation result justified the suitability of the proposed design and the accuracy of the control approaches adopted against the varying source power and load conditions.

The proposed virtual resistance-based P&O MPPT control technique performed well as expected, resulting in much less oscillation of the operating point and yielding a very quick and accurate response under dynamic working conditions. The findings of the in-depth study of the mechanical characteristics of the BLDC motor drive and the electrical characteristics were used to appropriately design the voltage and speed controllers, followed by a proper tuning of the respective PI controller parameters. As a result, remarkable accuracy and fast response of the speed and voltage controllers were noticed. In addition, the work featured an improved model of position sensorless electronic commutation system for the motor to dynamically adapt to the varying speed. Denying the need for low-pass filters and delay compensation circuits, and without relying on mathematical steps such as integrations and derivatives, the model could easily and accurately sense ZCPs of the BEMFs. This was successfully validated, though slightly increased ripple levels in currents and torque were observed.

The proposed MPPT model and the speed control model justified the energy efficiency and smooth operation of the drive under varying working conditions, such as irradiance and temperature, as well as under variable speed requirements for the load. The battery charge controller and DC bus voltage controller ensured safe operation, flexibility, and robustness in the control system. The sensorless commutation scheme depicted reduced redundancy in the motor drive system. In this way, the overall contribution of the work lies in enhancing the energy efficiency and reliability of solar powered BLDC motor drives.

Although this research provides valuable insights into improving the efficiency and performance of the solar-driven EVs, several limitations should be acknowledged. One of the limitations is the increased torque ripple that is likely to increase the noise and vibrations in the drive system. The other challenge is the poor duty cycle of the battery and its slow charging (often taking several hours to days) due to the low power available from the photovoltaic arrays. This results in reduced driving range and more charging bills. Also, the proposed model was evaluated in a simulated environment, which may not fully represent real-world conditions, since experimental validation is lacking.

This research lays the groundwork for further exploration in minimising ripple torques observed in sensorless control by different means. The proposed model could be extended further to harness the traction torques in terms of regenerative braking that helps to increase the battery duty cycle to some extent. An additional topology has to be integrated into the existing system to connect it to the power grid that facilitates in rapid battery charging. The next research step should focus on the practical implementation of the proposed model through experimental validation.

REFERENCES

[1] P. Plötz, C. Moll, G. Bieker, and P. Mock, “From Lab-to-Road: Real-World Fuel Consumption and CO2 Emissions of Plug-in Hybrid Electric Vehicles,” *Environmental Research Letters*, vol. 16, no. 5, p. 054078, 2021. [HypRef]. (13)

[2] S. Gnanavendan, S. K. Selvaraj, S. J. Dev, K. K. Mahato, R. S. Swathish, G. Sundaramali, O. Accouche, and M. Azab, “Challenges, Solutions and Future Trends in EV-Technology: A Review,” *IEEE Access*, vol. 12, pp. 17 242–17 260, 2024. [HypRef]. (13)

[3] D. Zhao, M. Zhou, J. Wang, T. Zhang, G. Li, and H. Zhang, “Dispatching Fuel-cell Hybrid Electric Vehicles Toward Transportation and Energy Systems Integration,” *CSEE Journal of Power and Energy Systems*, vol. 9, no. 4, pp. 1540–1550, 2023. [HypRef]. (14)

[4] D. Mohanraj, R. Aruldavid, R. Verma, K. Sathiyasekar, A. B. Barnawi, B. Chokkalingam, and L. Mihet-Popa, “A Review of BLDC Motor: State of Art, Advanced Control Techniques, and Applications,” *IEEE Access*, vol. 10, pp. 54 833–54 869, 2022. [HypRef]. (14)

[5] C. Chan, K. Chau, J. Jiang, W. Xia, M. Zhu, and R. Zhang, “Novel permanent magnet motor drives for electric vehicles,” *IEEE Transactions on Industrial Electronics*, vol. 43, no. 2, pp. 331–339, 1996. [HypRef]. (15)

[6] M. S. N. Krishna konijeti and M. Bharathi, “Extraction of Maximum Power from Solar with BLDC Motor Driven Electric Vehicles Based HHO Algorithm,” *Advances in Engineering Software*, vol. 170, p. 103137, 2022. [HypRef]. (16)

[7] N. R. Raipure, R. T. Ugale, and B. N. Chaudhari, “Solar Powered BLDC Motor Drive for Wide Speed Range Electric Vehicle Application,” in *2018 IEEE International Conference on Power Electronics, Drives and Energy Systems (PEDES)* IEEE, 2018, pp. 1–6. [HypRef]. (16)

[8] P. Kumar, D. V. Bhaskar, U. R. Muduli, A. R. Beig, and R. K. Behera, "Iron-Loss Modeling With Sensorless Predictive Control of PMBLDC Motor Drive for Electric Vehicle Application," *IEEE Transactions on Transportation Electrification*, vol. 7, no. 3, pp. 1506–1515, 2021. [HypRef]. (16)

[9] P. Mandre, S. Gupta, and S. Nema, "BLDC Motor Driven By ANN-Based Solar-PV And Battery Fed EV System With Regenerative Braking," in *2023 IEEE Renewable Energy and Sustainable E-Mobility Conference (RESEM)* IEEE, 2023, pp. 1–6. [HypRef]. (16)

[10] S. S. Rauth and B. Samanta, "Comparative Analysis of IM/BLDC/PMSM Drives for Electric Vehicle Traction Applications Using ANN-Based FOC," in *2020 IEEE 17th India Council International Conference (INDICON)* IEEE, 2020, pp. 1–8. [HypRef]. (16)

[11] G. de Cesare, D. Caputo, and A. Nascetti, "Maximum Power Point Tracker for Portable Photovoltaic Systems with Resistive-like Load," *Solar Energy*, vol. 80, no. 8, pp. 982–988, 2006. [HypRef]. (21, 25)

[12] M. A. Elgendy, B. Zahawi, and D. J. Atkinson, "Assessment of Perturb and Observe MPPT Algorithm Implementation Techniques for PV Pumping Applications," *IEEE Transactions on Sustainable Energy*, vol. 3, no. 1, pp. 21–33, 2012. [HypRef]. (21, 25)

[13] N. Karami, N. Moubayed, and R. Outbib, "General Review and Classification of Different MPPT Techniques," *Renewable and Sustainable Energy Reviews*, vol. 68, pp. 1–18, 2017. [HypRef]. (22, 25)

[14] Ö. F. Tozlu and H. Çalık, "A Review and Classification of Most Used MPPT Algorithms for Photovoltaic Systems," *Hittite Journal of Science and Engineering*, vol. 8, no. 3, pp. 207–220, 2021. [HypRef]. (22, 25)

[15] K. S. Tey and S. Mekhilef, "Modified Incremental Conductance MPPT Algorithm to Mitigate Inaccurate Responses under Fast-Changing Solar Irradiation Level," *Solar Energy*, vol. 101, pp. 333–342, 2014. [HypRef]. (22, 25)

[16] A. Hudec, R. Ondica, R. Ravasz, and V. Stopjakova, “Constant Voltage Maximum Power Point Tracking Method for Fully Integrated Solar-Powered Energy Harvester,” in *2024 27th International Symposium on Design & Diagnostics of Electronic Circuits & Systems (DDECS)*, 2024, pp. 152–155. [HypRef]. (22, 25)

[17] A. W. Leedy, L. Guo, and K. A. Aganah, “A Constant Voltage MPPT Method for a Solar Powered Boost Converter with DC Motor Load,” in *2012 Proceedings of IEEE Southeastcon*, 2012, pp. 1–6. [HypRef]. (22, 25)

[18] X. Li, H. Wen, Y. Hu, and L. Jiang, “A Novel Beta Parameter Based Fuzzy-Logic Controller for Photovoltaic MPPT Application,” *Renewable Energy*, vol. 130, pp. 416–427, 2019. [HypRef]. (22, 25)

[19] M. S. Ngan and C. W. Tan, “A Study of Maximum Power Point Tracking Algorithms for Stand-Alone Photovoltaic Systems,” in *2011 IEEE Applied Power Electronics Colloquium (IAPEC)*, 2011, pp. 22–27. [HypRef]. (22, 25)

[20] S. Messalti, A. Harrag, and A. Loukriz, “A New Variable Step Size Neural Networks MPPT Controller: Review, Simulation and Hardware Implementation,” *Renewable and Sustainable Energy Reviews*, vol. 68, pp. 221–233, 2017. [HypRef]. (22, 25)

[21] D. Verma, S. Nema, A. Shandilya, and S. K. Dash, “Maximum Power Point Tracking (MPPT) Techniques: Recapitulation in Solar Photovoltaic Systems,” *Renewable and Sustainable Energy Reviews*, vol. 54, pp. 1018–1034, 2016. [HypRef]. (22, 25)

[22] B. L. Mathur and R. Ramaprabha, “Intelligent Controller based Maximum Power Point Tracking for Solar PV System,” *International Journal of Computer Applications*, vol. 12, no. 10, pp. 37–42, 2011. [HypRef]. (23, 25)

[23] C. Larbes, S. Aït Cheikh, T. Obeidi, and A. Zerguerras, “Genetic Algorithms Optimized Fuzzy Logic Control for the Maximum Power Point Tracking in Photovoltaic System,” *Renewable Energy*, vol. 34, no. 10, pp. 2093–2100, 2009. [HypRef]. (23, 25)

[24] N. Priyadarshi, S. Padmanaban, M. Sagar Bhaskar, F. Blaabjerg, and A. Sharma, "Fuzzy SVPWM-based Inverter Control Realisation of Grid Integrated Photovoltaic-Wind System with Fuzzy Particle Swarm Optimisation Maximum Power Point Tracking Algorithm for a Grid-Connected PV/Wind Power Generation System: Hardware Implementation," *IET Electric Power Applications*, vol. 12, no. 7, pp. 962–971, 2018. [HypRef]. (23, 25)

[25] P.-C. Cheng, B.-R. Peng, Y.-H. Liu, Y.-S. Cheng, and J.-W. Huang, "Optimization of a Fuzzy-Logic-Control-Based MPPT Algorithm Using the Particle Swarm Optimization Technique," *Energies*, vol. 8, no. 6, pp. 5338–5360, 2015. [HypRef]. (23, 25)

[26] A. Mohapatra, B. Nayak, P. Das, and K. B. Mohanty, "A Review on MPPT Techniques of PV System under Partial Shading Condition," *Renewable and Sustainable Energy Reviews*, vol. 80, pp. 854–867, 2017. [HypRef]. (23, 25)

[27] Z. A. Alexakis, A. T. Alexandridis, and G. C. Konstantopoulos, "Direct MPP tracking of PV by estimating the Virtual Optimal Resistance," in *2022 30th Mediterranean Conference on Control and Automation (MED)*, 2022, pp. 1024–1029. [HypRef]. (23)

[28] K. Iizuka, H. Uzuhashi, M. Kano, T. Endo, and K. Mohri, "Microcomputer Control for Sensorless Brushless Motor," *IEEE Transactions on Industry Applications*, vol. IA-21, no. 3, pp. 595–601, 1985. [HypRef]. (26, 28)

[29] J. Shao, D. Nolan, M. Teissier, and D. Swanson, "A novel microcontroller-based sensorless brushless DC (BLDC) motor drive for automotive fuel pumps," *IEEE Transactions on Industry Applications*, vol. 39, no. 6, pp. 1734–1740, 2003. [HypRef]. (26, 28)

[30] T.-H. Kim and M. Ehsani, "Sensorless control of the BLDC motors from near-zero to high speeds," *IEEE Transactions on Power Electronics*, vol. 19, no. 6, pp. 1635–1645, 2004. [HypRef]. (26, 28)

[31] G.-J. Su and J. McKeever, "Low-cost sensorless control of brushless DC motors with improved speed range," *IEEE Transactions on Power Electronics*, vol. 19, no. 2, pp. 296–302, 2004. [HypRef]. (26, 28)

[32] R. Becerra, T. Jahns, and M. Ehsani, “Four-quadrant sensorless brushless ECM drive,” in *[Proceedings] APEC ’91: Sixth Annual Applied Power Electronics Conference and Exhibition*, 1991, pp. 202–209. [HypRef]. (26, 28)

[33] S. Ogasawara and H. Akagi, “An approach to position sensorless drive for brushless DC motors,” *IEEE Transactions on Industry Applications*, vol. 27, no. 5, pp. 928–933, 1991. [HypRef]. (26, 28)

[34] J. Shen and S. Iwasaki, “Sensorless control of ultrahigh-speed PM brushless motor using PLL and third harmonic back EMF,” *IEEE Transactions on Industrial Electronics*, vol. 53, no. 2, pp. 421–428, 2006. [HypRef]. (26, 27, 28, 40)

[35] J. Shen, Z. Zhu, and D. Howe, “Sensorless flux-weakening control of permanent-magnet brushless machines using third harmonic back EMF,” *IEEE Transactions on Industry Applications*, vol. 40, no. 6, pp. 1629–1636, 2004. [HypRef]. (26, 27, 28)

[36] B. Terzic and M. Jadric, “Design and implementation of the extended Kalman filter for the speed and rotor position estimation of brushless DC motor,” *IEEE Transactions on Industrial Electronics*, vol. 48, no. 6, pp. 1065–1073, 2001. [HypRef]. (27, 28)

[37] P. Damodharan and K. Vasudevan, “Sensorless Brushless DC Motor Drive Based on the Zero-Crossing Detection of Back Electromotive Force (EMF) From the Line Voltage Difference,” *IEEE Transactions on Energy Conversion*, vol. 25, no. 3, pp. 661–668, 2010. [HypRef]. (27, 45)

[38] A. A. Pesaran, “Lithium-Ion Battery Technologies for Electric Vehicles: Progress and challenges,” *IEEE Electrification Magazine*, vol. 11, no. 2, pp. 35–43, 2023. [HypRef]. (32)

[39] K. Nguyen, T. Taufik, R. N. Hasanah, and T. Nurwati, “Multiple Input Single Output Converter with MPPT for Renewable Energy Applications,” in *2020 10th Electrical Power, Electronics, Communications, Controls and Informatics Seminar (EECCIS)*, 2020, pp. 81–86. [HypRef]. (34)

[40] A. Tomar, S. Mishra, and C. N. Bhende, “Modified MISO DC-DC Converter Based PV Water Pumping System,” in *2016 IEEE 7th Power India International Conference (PIICON)*, 2016, pp. 1–6. [HypRef]. (34)

[41] N. Mohan, T. M. Undeland, and W. P. Robbins, *Power Electronics: Converters, Applications, and Design* John Wiley & Sons, 2003. (35, 36, 37)

[42] S. Jadhav, N. Devdas, S. Nisar, and V. Bajpai, “Bidirectional DC-DC converter in Solar PV System for Battery Charging Application,” in *2018 International Conference on Smart City and Emerging Technology (ICSCET)*, 2018, pp. 1–4. [HypRef]. (35, 36, 37)

[43] R. Kumar and B. Singh, “Grid Interactive Solar PV-Based Water Pumping Using BLDC Motor Drive,” *IEEE Transactions on Industry Applications*, vol. 55, no. 5, pp. 5153–5165, 2019. [HypRef]. (38)

[44] P. Ramadass, B. Haran, R. White, and B. N. Popov, “Mathematical Modeling of the Capacity Fade of Li-ion Cells,” *Journal of Power Sources*, vol. 123, no. 2, pp. 230–240, 2003. [HypRef]. (44)

APPENDICES

Appendix A: Publications

Title	Authors	Year	Journal/ Conference	Comments
Multi-Input Single-Output Topology with BWO MPPT for Efficient Solar-Powered BLDC Motor Drives in SCVs	Aashish Acharya, D.V. Bhaskar, Snehil Verma, Alok Ranjan	2025	IEEE Conference	Accepted
Sensor-less Commutation of Brushless DC Motor Based on Zero- Crossing Detection of Line Voltage Differences	Aashish Acharya, D.V. Bhaskar, Jeetendra Chaudhary, Madhusudan Nyaupane	2025	IOEGC	Accepted

Appendix B: Plagiarism Test Result

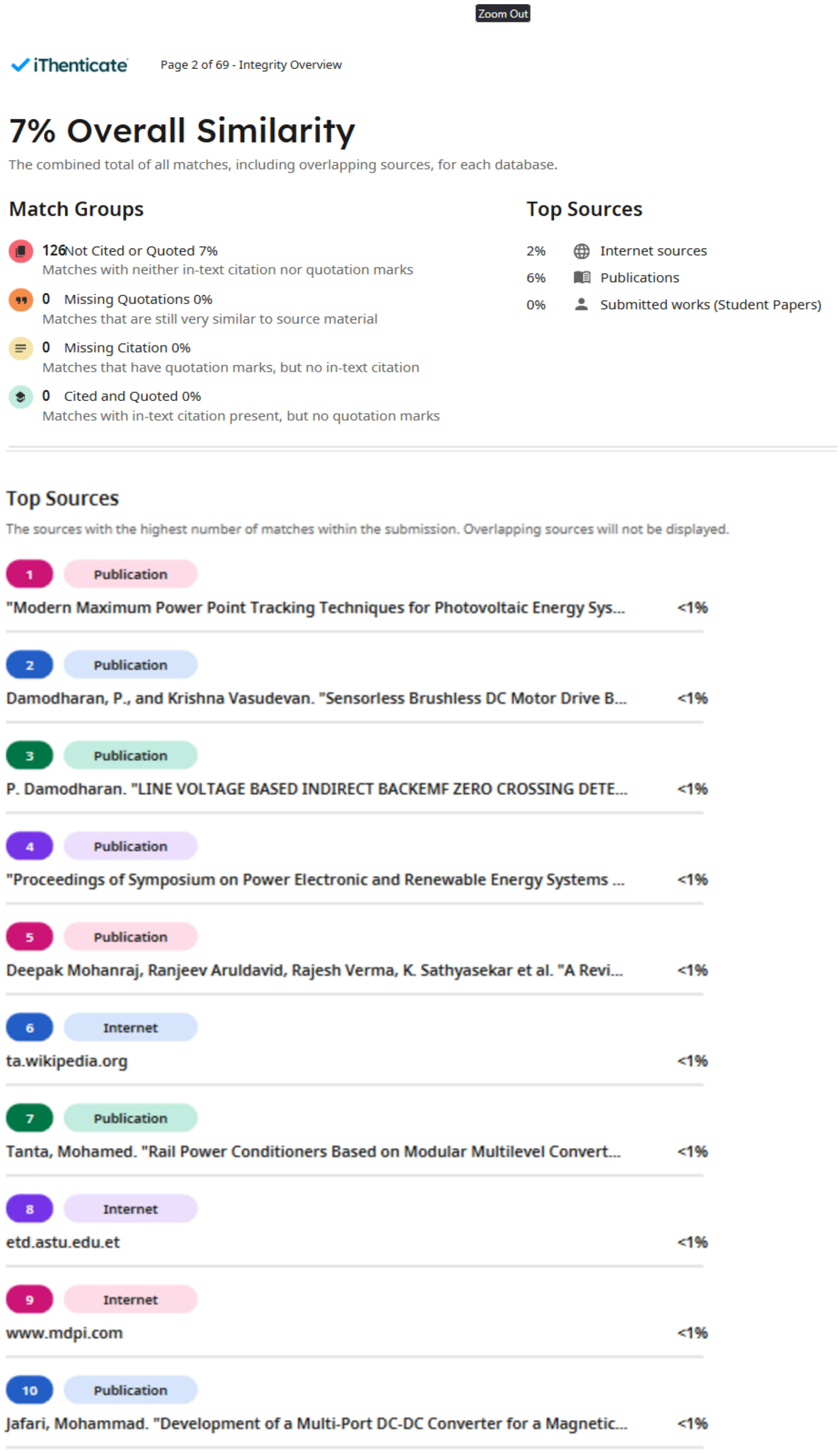

Page 2 of 69 - Integrity Overview

7% Overall Similarity

The combined total of all matches, including overlapping sources, for each database.

Match Groups

126 Not Cited or Quoted 7%
Matches with neither in-text citation nor quotation marks

0 Missing Quotations 0%
Matches that are still very similar to source material

0 Missing Citation 0%
Matches that have quotation marks, but no in-text citation

0 Cited and Quoted 0%
Matches with in-text citation present, but no quotation marks

Top Sources

2%	Internet sources
6%	Publications
0%	Submitted works (Student Papers)

Top Sources

The sources with the highest number of matches within the submission. Overlapping sources will not be displayed.

1	Publication	"Modern Maximum Power Point Tracking Techniques for Photovoltaic Energy Sys...	<1%
2	Publication	Damodharan, P., and Krishna Vasudevan. "Sensorless Brushless DC Motor Drive B...	<1%
3	Publication	P. Damodharan. "LINE VOLTAGE BASED INDIRECT BACKEMF ZERO CROSSING DETE...	<1%
4	Publication	"Proceedings of Symposium on Power Electronic and Renewable Energy Systems ...	<1%
5	Publication	Deepak Mohanraj, Ranjeev Aruldavid, Rajesh Verma, K. Sathyasekar et al. "A Revi...	<1%
6	Internet	ta.wikipedia.org	<1%
7	Publication	Tanta, Mohamed. "Rail Power Conditioners Based on Modular Multilevel Convert...	<1%
8	Internet	etd.astu.edu.et	<1%
9	Internet	www.mdpi.com	<1%
10	Publication	Jafari, Mohammad. "Development of a Multi-Port DC-DC Converter for a Magnetic...	<1%

Multi-Input Single-Output Topology with BWO MPPT for Efficient Solar-Powered BLDC Motor Drives in SCVs

Aashish Acharya
Electrical Engg. Department
Institute of Engineering
Pulchowk Campus, Nepal
aashishacharya555@gmail.com

Devara Vijaya Bhaskar
Electrical Engg. Department
IIT Dhanbad
Jharkhand, India
devara@iitism.ac.in

Snehil Verma
Electrical Engg. Department
IIT Dhanbad
Jharkhand, India
23MT0395@iitism.ac.in

Alok Ranjan
Electrical Engg. Department
IIT Dhanbad
Jharkhand, India
alokr9918@gmail.com

***Abstract*—This paper presents a multiple inputs single output (MISO) DC-DC converter-based model of an energy efficient solar-powered brushless DC motor drive for small commercial vehicles. Energy efficiency of the system is ensured by extracting maximum power available from the solar photo-voltaic (SPV) arrays at different working conditions using a novel Black Widow Optimization (BWO) based Maximum Power Point Tracking (MPPT) algorithm. For smooth and reliable operation of the drive a battery bank is integrated to the system that operates in parallel with the SPV arrays to establish a constant dc bus using a bidirectional converter as an interface to the bus. The effectiveness of the system under varying scenarios of temperature and irradiance is validated through Simulation results.**

***Index Terms*—Small Commercial Vehicles (SCVs), Solar photovoltaic (PV), Black Widow Optimization (BWO), BLDC Motors (Brushless DC Motors).**

I. INTRODUCTION

The extraction and exploitation of non-renewable energy sources has been increasing exponentially every year with increase in world population. This has not only led to rapid depletion of such energy sources but has also resulted in serious impacts to the environment and the society. It has been reported that the transportation sector has one of the biggest carbon footprints contributing significantly to greenhouse gas emissions and resulting in a number of environmental issues [1]. It is now high time to lessen its carbon footprints due to pressing concerns like pollution, global warming, ozone layer depletion, and the health risks these issues pose [2].

Efforts are being put to transform the transportation sector from fossil fuel-based technology to clean and green technology with the integration of several renewable energy sources. Government of some countries with expanding automotive markets have made some promising attempts to address such issues by promoting more efficient and decarbonized electric vehicles (EVs) [3]. Especially, the demand of small commercial vehicles has rapidly grown in the recent years, enforcing the manufacturers to compete for maximizing performance and minimizing cost. Solar photovoltaic (SPV) system driven BLDC motor drives can be one of the compelling alternatives for improving energy efficiency of such vehicles with minimal emissions [4].

Despite limited literature available on SPV-integrated BLDC motors, many researchers have shown interest in extending the application of SPV arrays in SCVs driven by BLDC motors [5], [6]. This can potentially be the best substitute for the Induction Motor, the giant in industrial market, which will indeed reduce the size and weight of the vehicle [7]. However, the implementation of SPV system driven BLDC motor drive has to face several technical challenges. The first challenge is the irradiance and temperature dependence of solar power generation leading to fluctuation of power generation. In an electric vehicle, conditions such as shading and non-uniform irradiance on PV panels cannot be ignored due to several reasons such as vehicle orientation with respect to sunlight, design constraints, nearby trees and buildings, cloud coverage, smoke and fog etc. In conventional Single Input Single Output (SISO) dc-dc converter-based system, extraction of power from PV units is effective only when uniform irradiance throughout the panel surface is available. In such system, solar power generation while even working at MPPT is significantly reduced by partial shading and mismatching of series and parallel connected PV modules. Thus, if there are frequent changes in working conditions of SPV array then it will indeed impact the performance of the drive greatly. The second challenge is the slow convergence and power oscillations issues of the conventional MPPT control algorithms such as Perturb and Observe and Incremental Conductance that prevents the vehicles from achieving a good steady state and dynamic performance. The third challenge is the inherent shortcomings of electrolytic capacitor such as its poor lifespan, low-frequency operation and overweight as most of the conventional EVs are still found to operate using these capacitors as a dc link owing to their low cost. Lastly, there still lies a hassle of sophisticated control of the speed and torque of the vehicle for meeting the varying load requirements.

As proposed in some literatures [8], [9], Multi Input Single Output (MISO) dc-dc converter-based systems help in overcoming the sudden drop in power generation due to non-uniform irradiance and impedance mismatching of SPV arrays operating in parallel. Since each array unit will have its

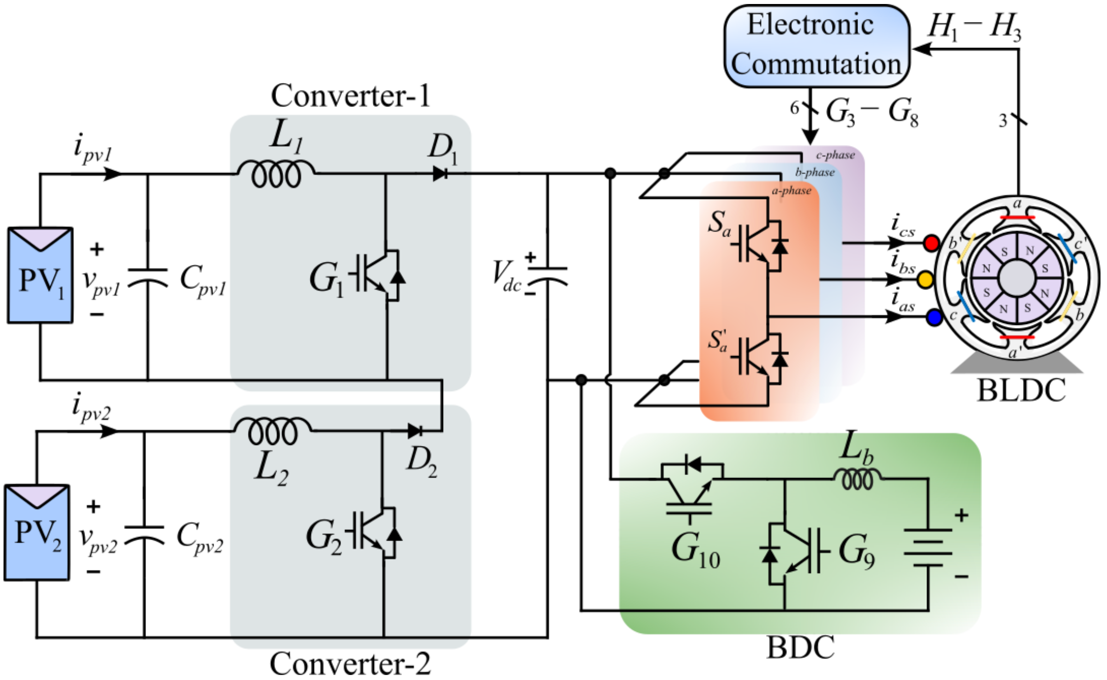

Fig. 1: Schematic configuration of presented system

own MPPT controller, the optimal power extraction from one array unit is unaffected by the change in operating conditions (irradiance and temperature) of the other units. Further, the battery bank working in parallel with SPV arrays can be used to establish a constant dc bus voltage and supply additional load current to the motor thereby fulfilling the load speed and torque requirements. To overcome the limitations of conventional MPPT control algorithms discussed above, a new nature inspired meta-heuristic algorithm called Black Widow Optimization (BWO) proposed in [10] and implemented in [11] can be used as a better alternative. The algorithm, being inspired from the unique mating behaviour of black widow spiders and their lifecycle, is well known for its fast convergence especially in dynamic conditions. As suggested in [12], [13], a film capacitor stands as a better substitute for the conventional electrolytic one despite its higher cost as a dc link interface. This is because of its superior characteristics like longer lifespan, wider operating temperature range, lower losses, better voltage surges and current ripple handling etc.

Based on the challenges and their potential solutions discussed above, the paper proposes a model of Multi Input Single Output (MISO) dc-dc converter-based BLDC motor drive system where two SPV arrays along with a battery bank, being used as the power sources, feed the BLDC motor through a common dc bus. One of the key features of proposed system is the implementation of the BWO based MPPT algorithm to control the power flow from MISO converters. A film capacitor is used to establish a dc bus which connects to the inverter terminals of the BLDC motor drive.

The organization of the paper is as follows. Section II presents the proposed system architecture and its design accompanying the calculations of various parameters to justify the design requirements. Section III discusses the control approaches of different components being used in detail such as MPPT control, battery charge control and speed control of BLDC motor. Section IV presents the simulation results under different circumstances that validate the proposal and Section V contains the conclusion.

II. SYSTEM ARCHITECTURE AND ITS DESIGN

The BWO-MPPT-based SPV-driven BLDC motor integrated with battery is illustrated in Fig 1. The system comprises an SPV array powering the BLDC motor through a boost converter and VSI, while also feeding the battery (during charging) via a boost converter and a bidirectional converter. BWO-MPPT generates the switching pulses for the boost converter. Meanwhile, Hall-sensor-based control strategy generates the pulses for VSI. The battery charging/discharging is governed by a Bidirectional Converter (BDC) controller.

TABLE I: PV Array Parameters

Parameter	**Symbol**	**Value**
Open-Circuit Voltage	V_{oc}	44.9 V
Short-Circuit Current	I_{sc}	8.88 A
Voltage at Maximum Power	V_{mt}	36.9 V
Current at Maximum Power	I_{mt}	8.41 A
Temperature Coefficient of V_{oc}	η_{oct}	-0.32 %/°C
Temperature Coefficient of I_{sc}	η_{sct}	0.058 %/°C

A. Design of SPV Array

Power rating of the SPV array is decided considering rated power output of the motor and losses that occur in different

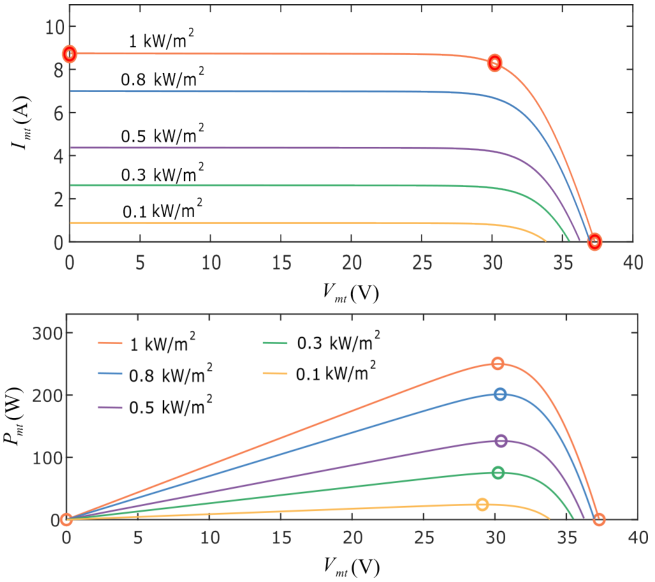

Fig. 2: I-V and P-V characteristics

parts of the system such as dc-dc converters, battery and VSI. For this, 2 SPV array units each with a peak power capacity Pm(arr) of 1.5 kW extractable at standard test conditions (1000 W/m^2 Irradiance; 25 °C cell temperature; 1.5 spectrum AM) is proposed. This is achieved using PV modules belonging to TATA Power Solar TP250 model with specifications as shown in Table I. Its I-V and P- V characteristics at different irradiance as depicted in Fig. 2. The maximum output voltage of the SPV arrays (Vm(arr)) is chosen based on the magnitude of constant DC-bus voltage (V_{bus}) and the topology of the interfacing converter selected as shown in Fig. 1. Thus, V^m_{arr1} is set to 91 V.

The maximum current of SPV array $I_{m(arr)}$ can be estimated as:

$$I^m_{arr1} = \frac{P^m_{arr1}}{V^m_{arr1}},\ I^m_{arr2} = \frac{P^m_{arr2}}{V^m_{arr2}} \tag{1}$$

where N_s and N_p represent the number of series connected PV modules per string and number of such strings connected in parallel respectively to form the array of desired power rating, then their values can be approximated as:

$$\begin{cases} N_{s1} = \dfrac{V^m_{arr1}}{V^m_{\text{mod 1}}},\ N_{s2} = \dfrac{V^m_{arr2}}{V^m_{\text{mod 2}}} \\ N_{p1} = \dfrac{I^m_{arr1}}{I^m_{\text{mod 1}}},\ N_{p2} = \dfrac{I^m_{arr1}}{I^m_{\text{mod 1}}} \end{cases} \tag{2}$$

where N_{s1} and N_{s2} are the number of series connected modules for SPV1 and SPV2 respectively. The N_{p1} and N_{p2} are the number of parallel connected modules for SPV1 and SPV2 respectively

Therefore, 2 strings each containing 3 series connected PV modules are required to form an SPV1 array of desired rating. Thus, at MPP the total solar power generation will be 3 kW at 182 V.

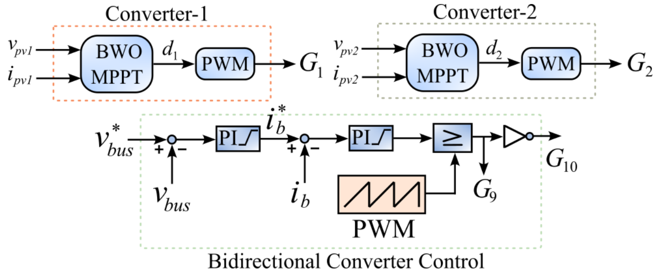

Fig. 3: Schematic block diagram of the system

B. Design of Boost Converter

The boost converter output is given as follows [14]:

$$V_{o1} = \left(\frac{1}{1-d_1}\right) V_{in},\ V_{o2} = \left(\frac{1}{1-d_2}\right) V_{in} \tag{3}$$

where, V_{o1}, $V_{o2}$and V_{in} are the output of SPV 1 and 2,and input voltage of the boost converter respectively and d_1 and d_2 are the duty ratio.

To determine the value of the inductor (L_l), duty ratio and switching frequency (f_{sw}) is required, f_{sw} is taken as 5 kHz and the duty ratio, which is integral to the design process, is subsequently determined using (3).

$$L_{l1} = \frac{d_1 \times V_{m(arr)}}{f_{sw} \times \Delta I_{L1}},\ L_{l2} = \frac{d_2 \times V_{m(arr)}}{f_{sw} \times \Delta I_{L2}} \tag{4}$$

Here, ΔI_L denotes the ripple in the inductor current, which is assumed to be 20% of the maximum inductor current ($I_L = I_{ma}$).

C. Design of BDC and BES

Fig 3 illustrates the bidirectional Buck-Boost converter circuit, which serves as the interface between the battery and the VSI. The converter must operate efficiently in buck and boost mode to ensure precise parameter determination. Considering this, the value of inductor (L_b) can be calculated using [14], [15]:

$$L_b = \frac{d \times (V_{bus} - V_b)}{f_{sw} \times \Delta I_b} \tag{5}$$

. The common DC-link capacitance will serve as output capacitance of the converter. To ensure optimal regulation of power flow and maintain reliable and efficient operation, it requires a sophisticated control scheme for both charging and discharging the battery which will be discussed in Section III.

To ensure reliable motor operation when SPV power is unavailable, Li-ion batteries are the optimal choice due to their superior energy density, which provides a prolonged driving range - vital for SCVs. Furthermore, their fast charging capabilities offer significant benefits to EV users.

D. Selection of TPTL Inverter

The motor is driven by using a TPTL VSI consisting of six IGBT switches. The overloading of these switches may lead to inverter failure. Therefore, the capacity of these switches should be carefully selected to prevent such failure. To accommodate transients likely to occur in the IGBT switches, as suggested in [15], voltage safety factor of 1.4 and current

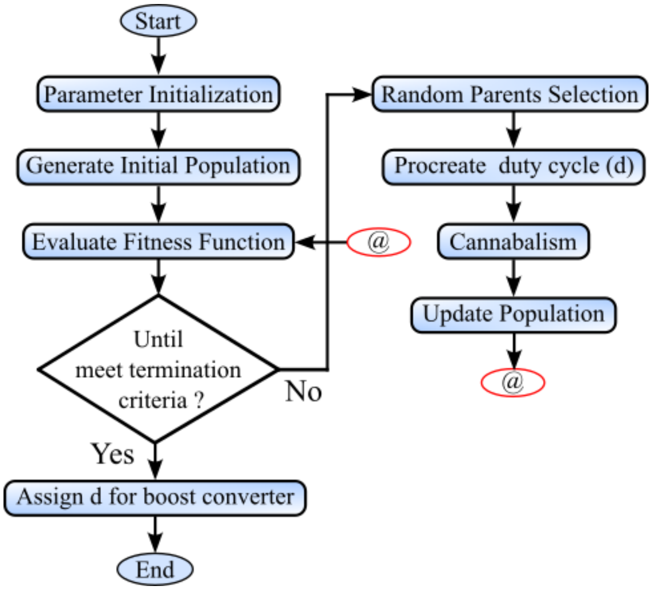

Fig. 4: BWO-based flow chart for MPP tracking

safety factor of 1.3 are considered. Therefore, the required voltage rating (V_{VSI}) and current rating (I_{VSI}) of each IGBT switch are calculated as:

$$\begin{cases} V_{vsi} = 1.4 * V_{bus} = 336 \text{ V} \\ I_{vsi} = 1.3 * I_{bus} = 15.37 \text{ A} \end{cases} \tag{6}$$

The VA rating of inverter can be calculated as $VA_{vsi}^{rating} = V_{vsi} * I_{vsi}$.

E. Selection of Common DC-Link Capacitor

A film capacitor is used as a DC-link capacitor due to its various advantages over electrolytic capacitors such as high current conduction capability, lower ESR (Equivalent series resistance), and can be operated at high frequency.

In a VSI, the DC link capacitor primarily serves two functions: 1) It provides a low impedance path for high-frequency currents, and 2) It stiffens the DC bus by decoupling the effects of stray inductance between the DC voltage source and VSI.

To mitigate the safety concerns associated with excessive capacitance for DC-bus, it's important to compute the correct capacitance which can be determined as follows [15].

$$C = \frac{V_{bus}}{32 L_s \Delta V_{bus} f_{sw}^2} \tag{7}$$

where, ΔV_{bus} is the ripple in the dc-bus voltage.

III. Proposed Control Approach

The control strategy focuses on optimizing LCV performance by integrating solar-powered BLDC motors with a battery system. It comprises BWO-based MPPT control, charging and discharging of battery, and speed control of BLDC motor. All these control strategies are evaluated across different cases to optimize overall energy management and boost vehicle performance.

TABLE II: BLDC Motor Parameters

Parameter	**Value**
Number of Phases	3
Number of Poles	8
DC Voltage (V_{bus})	240 V
Rated Power (P_{rated})	2.5 kW
Rated Flux (Φ_{rated})	0.175 Wb
Stator Resistance (R_s)	2.4 Ω
Stator Inductance (L_s)	8.5 mH
Moment of Inertia (J)	0.089 kg·m^2
Damping Coefficient (B)	0.001 Nm·s/rad
Sampling Time (T_s)	10 μs

A. MPPT Control Approach

The proposed model integrates the Black Widow Optimization (BWO) algorithm, esteemed for its fast convergence and superior attainment of optimized fitness values relative to alternative algorithms [10]. It incorporates a distinctive phase—cannibalism, which endows it with the capacity to expunge species with suboptimal fitness from the exploration domain.

Fig. 4 shows the BWO-based flow chart for MPP tracking. Initially, crucial parameters are defined such as Population size (N), Number of iterations (k), Mutation rate (α), and Cannibalism rate (β). Then the random duty cycle (d) is generated:

$$W = \{d_1^k, d_2^k, d_3^k, \ldots, d_N^k\}, \quad 0 \leqslant d_i^k \leqslant 0.95 \tag{8}$$

where, $0 \leqslant d_i^k \leqslant 0.95$, The fitness of a widow is determined by the evaluation of fitness function M:

$$\begin{cases} Max.\ M = V_{pv}(d_i^k) I_{pv}(d_i^k) \\ fitness = M\{W\} = M\{d_1^k, d_2^k, d_3^k, \ldots, d_N^k\} \end{cases}, \quad i \in [1, N] \tag{9}$$

After random selection of parents assuming d_1 and d_2, offspring d_{n1} and d_{n2} are produced using:

$$\begin{cases} d_{1,lm}^k = a \cdot d_l^k + (1-a) \cdot d_m^k \\ d_{2,lm}^k = a \cdot d_m^k + (1-a) \cdot d_l^k \end{cases}, \quad 1 \leqslant l, m \leqslant N, \ l \neq m \tag{10}$$

The optimal duty cycle obtained is then fed into the pulse generator shown in Fig. 3 to control the boost converter, ultimately facilitating maximum power extraction from SPV.

B. Charging and Discharging of Battery

In the proposed system, a Proportional-Integral (PI) control strategy is implemented to manage the battery charging and discharging processes. The BDC facilitates a flawless power transfer between the battery and the BLDC motor, efficiently managing any power deficits and surpluses. Fig 3 illustrates a sophisticated implementation of the Battery control. The BDC, equipped with an inductor (L_b) and switch S_7 (with gate pulse G_7) and S_8 (with gate pulse G_8) with anti-parallel diodes (D_1 and D_2), regulates the battery charging/discharging

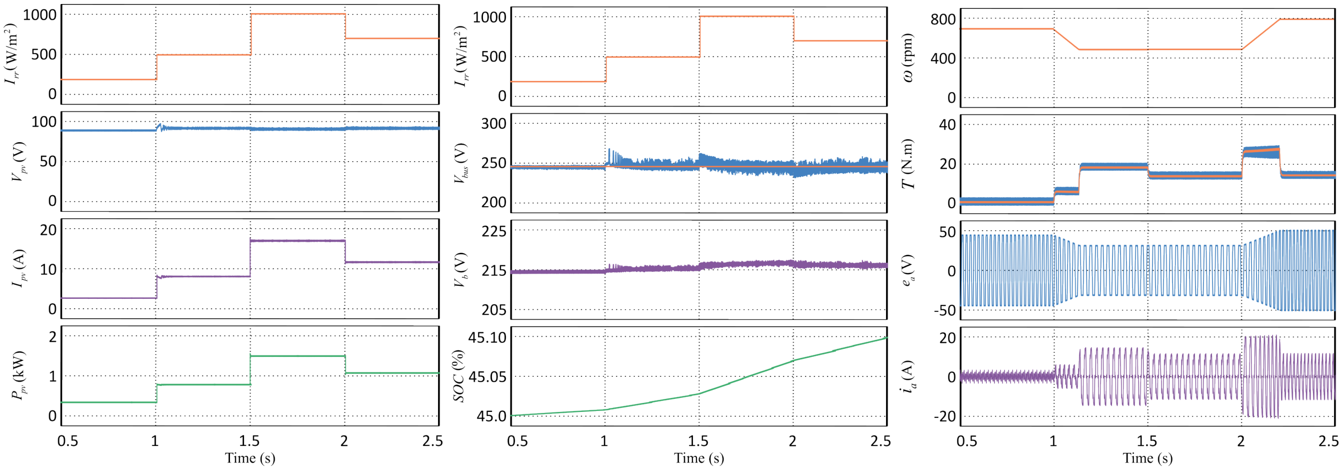

(a) (b) (c)

Fig. 5: System performance under irradiance variations (a) I_{rr}, V_{pv}, I_{pv} and I_{pv}, (b) I_{rr},V_{bus}, V_b, and SOC and (c) ω, T, e_a and i_a

current (I_b). The I_b^* can be calculated as follows:

$$I_b^* = \left(k_p + \frac{k_i}{s}\right)(V_{bus}^* - V_{bus}) \tag{11}$$

When the SPV power generation is not sufficient to run the motor, the battery discharges and the converter operates in boost mode with S_7 and D_1 active; conversely, in surplus conditions, it operates in buck mode with S_8 and D_2 active. The Battery control system regulates the dc-link voltage (V_{bus}) at a constant value, with any deviations promptly corrected by a PI controller, thereby ensuring smooth operation of the BLDC motor.

C. Speed Control of BLDC Motor

Fig. 1 shows the BLDC motor incorporating Hall effect sensors that detect the rotor position and provide essential feedback for precise control of speed and torque via efficient electronic commutation. The signals from the Hall sensors determine the switching sequence of the inverter's power electronic devices. The actual motor speed is perpetually compared with the reference speed, and the resultant error is fed into a proportional-integral (PI) controller which modulates the PWM pulses ($G_1 - G_6$) accordingly, ensuring that the motor adheres to the desired speed by fine-tuning the voltage applied to the motor. This adjustment facilitates optimal and seamless motor performance, even amidst varying load conditions.

IV. SIMULATION RESULTS AND DISCUSSIONS

The proposed system undergoes comprehensive simulation within the MATLAB environment, where its performance and behavior are evaluated under two distinct scenarios: (1) with varying irradiance and (2) with varying temperature. Furthermore, steady-state performance of the BLDC motor across various load conditions is examined. The simulation parameters utilized are detailed in Table I and II.

A. Under Varying Irradiance

Keeping the temperature of the SPV arrays constant, irradiance (I_{rr}) is varied in 4 phases, each with time interval of 0.5 seconds. Fig. 5 shows the impact of varying irradiance on the performance of the system in terms of different parameters. In the first phase (from 0.5 to 1 second), irradiance is set at 200 W/m^2 which initiates the charging process of the battery and is depicted by the gradual increase in its SoC. In the second phase (from t=1 to t=1.5 second) and the third phase (1.5 second to 2 seconds), the irradiance is further increased to 500 W/m^2 and 1000 W/m^2 respectively which causes the battery SoC to rise more steadily because of the increased photovoltaic current (I_{pv}). In the third phase, (from 2 to 2.5 seconds), SoC further keeps increasing but at lower rate than earlier, owing to decreased irradiance or current. The solar power (P_{pv}) being generated at any stage for the corresponding volage (V_{pv}) ensures MPP operation thereby proving the effectiveness of BWO-MPPT algorithm. The other key thing to notice is that though the battery voltage (V_b) keeps increasing as the battery charges with time, the DC bus voltage $(V_b us)$ is held fairly constant at approximately 240 V. This justifies the effectiveness of the controller associated with the bidirectional converter and the battery.

B. Under varying Temperature

The effect of temperature variation is also studied in 4 distinct phases each with time interval of 0.5 seconds keeping irradiance fixed at 700 W/m^2 as shown in Fig. 6. In the first phase (0.5 to 1 second), temperature is set to 25 °C and at each successive phases, the temperature is increased by 5 °C. This leads to a small decrement in solar voltage V_{pv} and power (P_{pv} in each phase however a very negligible impact is seen over solar current I_{pv} throughout the temperature variation steps. Since I_{pv} is not much affected, the battery continues to charge at a constant rate described by almost linear SoC curve. Further, the DC bus voltage is also held constant like in previous case irrespective of the battery voltage.

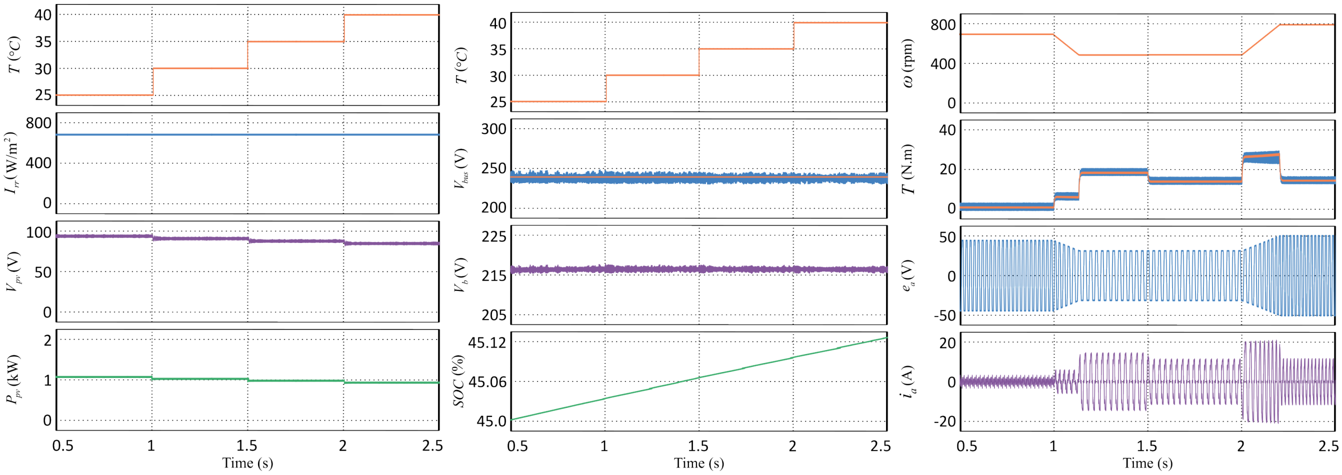

(a) (b) (c)

Fig. 6: Performance under temperature variations (a) T, I_{rr}, V_{pv} and I_{pv}, (b) T, V_{bus}, V_b, and SOC and (c) ω, T, e_a and i_a

The steady state performance of the motor as shown in Fig. 5(c) and Fig. 6(c) clearly validates the linear relationship of motor back-electromotive force (EMF) (e_a) with the motor angular speed (ω) and that of motor torque (T) with stator current (i_a). The shape of the motor back-EMF waveform is roughly trapezoidal as expected and that of stator current is like a quasi-square wave. Ripples in these waveforms is clearly visible which is due to commutation of stator current and depend on the stator resistance and inductances.

V. CONCLUSION

The paper proposes a model of the BWO MPPT based-solar-powered BLDC motor drive powered by two SPV arrays interfaced with MISO DC-DC converter and a battery bank interfaced with a bidirectional DC-DC converter to a common DC bus. It illustrates the selection and integration of the major components that form the system followed by their suitable control techniques that justifies energy efficiency and smooth operation of the drive under varying working conditions like irradiance and temperature. This is validated through the simulation results which ensures the effectiveness of the model and proves it to be a suitable alternative for driving SCVs. The next research step will be focused on practical implementation of the proposed model and its extension for dealing with dynamic load conditions.

REFERENCES

[1] P. Plötz, C. Moll, G. Bieker, and P. Mock, "From lab-to-road: Real-world fuel consumption and co2 emissions of plug-in hybrid electric vehicles," *Environmental Research Letters*, vol. 16, no. 5, p. 054078, 2021.

[2] S. Gnanavendan, S. K. Selvaraj, S. J. Dev, K. K. Mahato, R. S. Swathish, G. Sundaramali, O. Accouche, and M. Azab, "Challenges, solutions and future trends in ev-technology: A review," *IEEE Access*, 2024.

[3] D. Zhao, M. Zhou, J. Wang, T. Zhang, G. Li, and H. Zhang, "Dispatching fuel-cell hybrid electric vehicles toward transportation and energy systems integration," *CSEE Journal of power and Energy Systems*, vol. 9, no. 4, pp. 1540–1550, 2021.

[4] P. Kumar, D. V. Bhaskar, U. R. Muduli, A. R. Beig, and R. K. Behera, "Disturbance observer based sensorless predictive control for high performance pmbldcm drive considering iron loss," *IEEE Transactions on Industrial Electronics*, vol. 69, no. 6, pp. 5442–5452, 2021.

[5] ——, "Iron-loss modeling with sensorless predictive control of pmbldc motor drive for electric vehicle application," *IEEE Transactions on Transportation Electrification*, vol. 7, no. 3, pp. 1506–1515, 2020.

[6] P. Mandre, S. Gupta, and S. Nema, "Bldc motor driven by ann-based solar-pv and battery fed ev system with regenerative braking," in *2023 IEEE Renewable Energy and Sustainable E-Mobility Conference (RESEM)*. IEEE, 2023, pp. 1–6.

[7] E. E. A. Zahab, A. M. Zaki, and M. M. El-sotouhy, "Design and control of a standalone pv water pumping system," *Journal of Electrical Systems and Information Technology*, vol. 4, no. 2, pp. 322–337, 2017.

[8] K. Nguyen, T. Taufik, R. N. Hasanah, and T. Nurwati, "Multiple input single output converter with mppt for renewable energy applications," in *2020 10th Electrical Power, Electronics, Communications, Controls and Informatics Seminar (EECCIS)*. IEEE, 2020, pp. 81–86.

[9] A. Tomar, S. Mishra, and C. N. Bhende, "Modified miso dc-dc converter based pv water pumping system," in *2016 IEEE 7th Power India International Conference (PIICON)*. IEEE, 2016, pp. 1–6.

[10] V. Hayyolalam and A. A. P. Kazem, "Black widow optimization algorithm: a novel meta-heuristic approach for solving engineering optimization problems," *Engineering Applications of Artificial Intelligence*, vol. 87, p. 103249, 2020.

[11] N. Shobanadevi and M. PheminaSelvi, "Adaptive black widow optimization based mppt controller in high-gain non-isolated dc-dc converter for pv applications," 2023.

[12] J. Huo, N. Zhao, R. Gao, G. Zhang, G. Wang, and D. Xu, "Analysis and compensation of position estimation error for sensorless reduced dc-link capacitance ipmsm drives," *IEEE Transactions on Industrial Electronics*, vol. 70, no. 3, pp. 3213–3221, 2022.

[13] Y. Lu, B. Zhou, Y. Zhang, and Q. Chang, "Doubly salient electromagnetic motor-drive system with small dc-link capacitance," *IEEE Transactions on Industrial Electronics*, 2023.

[14] A. Ranjan, A. Prakash, and D. V. Bhaskar, "Comparative study of power factor correction converter topologies for pmbldc motor drives," in *2023 First International Conference on Cyber Physical Systems, Power Electronics and Electric Vehicles (ICPEEV)*, 2023, pp. 1–6.

[15] R. Kumar and B. Singh, "Grid interactive solar pv-based water pumping using bldc motor drive," *IEEE Transactions on Industry Applications*, vol. 55, no. 5, pp. 5153–5165, 2019.

Sensor-less Commutation of Brushless DC Motor Based on Zero-Crossing Detection of Line Voltage Differences

Aashish Acharya [a], Devara Vijaya Bhaskar [b], Jeetendra Chaudhary [c], Madhusudan Nyaupane [d]

[a] *Department of Electrical Engineering, Pulchowk Campus, IOE, Tribhuvan University, Nepal*
[b] *Department of Electrical Engineering, IIT (ISM) Dhanbad, Jharkhand, India*
[c] *Department of Electrical Engineering, Pulchowk Campus, IOE, Tribhuvan University, Nepal*
[d] *Department of Electrical Engineering, Pulchowk Campus, IOE, Tribhuvan University, Nepal*
✉ [a] aashishacharya555@gmail.com, [b] devara@iitism.ac.in, [c] jeetendra@ioe.edu.np, [d] nyaupanemadhusudan.hr@gmail.com

Abstract

In this paper, an electronic commutation strategy for Permanent Magnet Brushless DC motors without using position sensors is presented. Harnessing the difference of the line voltages measured across stator terminals, the proposed method precisely senses the zero-crossing instants of the back-electromotive forces indirectly by detecting their change in polarities with time as the motor rotates. This information is processed to generate appropriate switching pulses for the inverter switches, which in turn, facilitates electronic commutation without the need for position sensors. Furthermore, the method used omits the need for the motor neutral potential and does not involve mathematical steps such as derivatives and integrations. The validity of the method is examined in MATLAB Simulink where the results verify its accuracy and robustness describing the expected electrical and mechanical characteristics of the motor. The key contribution of the paper is proposing a less redundant design and improving the reliability of motor commutation through the replacement of the physical position sensors with virtual ones.

Keywords

Brushless DC (BLDC) motor, sensor-less commutation, back-electromotive force (EMF), zero-crossing point (ZCP), Pulse Width Modulation (PWM)

1. Introduction

Permanent magnet machines are widely used in applications such as industrial automation, domestic appliances, robotics, electric vehicles, aerospace, manufacturing processes, etc mainly because of their higher reliability and efficiency [1]. These machines are typically superior to conventional machines that usually contain windings on both rotor and stator, owing to their compact size, quiet operation and higher power-to-weight ratio. A BLDC motor is the simplest permanent magnet machine that replaces rotor windings with permanent magnets and mechanical commutation with electronic commutation. The function of the mechanical commutator and carbon brushes is achieved by using a Pulse Width Modulated (PWM) inverter and rotor position decoder. The rotor position decoder first senses the rotor position, decodes it, and accordingly generates appropriate switching pulses for the inverter. The electronic commutation thus achieved allows the rotor speed to synchronize with the inverter frequency.

Today, many BLDC motors are three-phase trapezoidal EMF-based equipped with Hall sensors as the rotor position decoder [2]. In such motors, the circle described by the rotation of the rotor can be divided into 6 distinct sectors each with an angular span of 60 electrical degrees. The rotor occupies any one of these sectors at any time instant. The three Hall sensors, which are ideally placed 120 electrical degrees apart, generate electric signals based on the Hall effect, unique to the rotor angular orientation. These signals are processed to develop appropriate switching pulses for the inverter via commutation logic that decides which phases to conduct and their duration of conduction. This is called electronic commutation. The goal of commutation is to establish a fairly constant angle close to 90 ° between the stator flux and the rotor flux, forcing the rotor to rotate continuously and developing maximum torque [3].

The inverter is generally operated either in 180° or 120° conduction mode. In the 180° conduction mode, each inverter switch conducts for 180° in one electrical cycle and thus all three phases are conducting at any time instant whereas, in 120° conduction mode, each switch conducts for 120° which causes any of the two phases to conduct at any time instant. Thus, the result is an increase in current continuity [4] and a higher power delivery [5] in the 180° conduction scheme compared to the 120° conduction scheme. However, the 120° conduction mode is still very common in several applications because the switching losses are relatively lower, and it assures approximate Maximum Torque per Ampere (MTPA) operation [6] despite reduced DC bus voltage utilization and discontinuous current.

There are several challenges and shortcomings associated with the BLDC motors that are based on position and speed sensors. Adding such sensors increases the design complexity and cost of the motor. Most of these sensors are sensitive to the temperature, vibrations and EMI and can lead to device failure thereby reducing the reliability of the machine. They may require frequent maintenance when operated in harsh environments. Constraints such as the volume and weight of the machine could be a big challenge for sensor-based motors. To avoid these challenges and shortcomings, several methods have been proposed in many works of literature that describe and validate the operation of BLDC motors without any position and speed sensors. These methods can be broadly categorized as:- back-EMF estimation methods [7, 8, 9], back-EMF integration methods [3, 10], freewheeling diode current detection methods [11], and third harmonic voltage component detection methods [12, 13].

The back-EMF estimation methods depend on detecting zero-crossing instants of the back-EMF across each phase harnessing the measured stator phase or line voltages. In [7], the terminal voltages are measured with respect to a virtual neutral point and low pass filters have been used to eliminate the higher-order harmonics. The limitations of this approach are the oscillation of the neutral point during PWM switching and delays introduced by the filters which does not make this approach suitable for a wide speed range. In [8], a method to estimate back-EMF indirectly without using true neutral or virtual neutral potential has been proposed. The technique used in [9] is defining a function to indicate the switching instants, that depends on measured voltages, currents and the derivatives of the currents. Though the EMF is sensed without the need for the true or virtual neutral point, the technique still relies on the complex computation of derivatives and could be affected by sensor noise. The back-EMF integration method used in [3] and [10] is based on integrating the back-EMF of the open phase. The integration is started right at the ZCP of the back-EMF and is stopped when the integration result attains a preset threshold value, which indicates the commutation instant. The benefit of this method is that it is less sensitive to noise and offers good performance at high speeds. The downside is that the method still requires neutral potential and may result in accumulated error, especially at low speeds due to the integrating operation.

Free-wheeling diode current detection methods [11] involve sensing the current in a free-wheeling diode connected across the open phase which facilitates knowing the rotor position. The method suits well for wide operating regions. However, the implementation of this method requires six comparators each with its own power source to detect the freewheeling currents. The third harmonic component of the back-EMF is obtained by adding all three terminal voltages [12, 13]. Integrating this component gives the third harmonic flux linkage whose zero crossing corresponds to the commutation instants. The limitation of this approach is that it requires the neutral point of the stator winding which is normally not provided by the manufacturer. Besides, the amplitude and phase of harmonic components could be affected by magnetic saturation thereby preventing the detection of true zero crossing instants. Apart from these methods, an Extended Kalman Filter (EKF)-based estimation method has also been proposed in [14]. The major challenge in applying the EKF method is the initialization of the covariance matrices which indicate uncertainties in measured and estimated parameters. Poorly initialized values may often lead to divergence and instability.

This paper proposes a straightforward method to estimate the rotor position by detecting the ZCPs of the trapezoidal (ideal) back-EMFs induced across the stator windings, for a three-phase star-connected permanent magnet BLDC motor. The method does not require the neutral potential since it involves measurement of the line voltages instead of the phase voltages and estimates the back EMFs with respect to the negative terminal of the DC source. The method is easy to implement since it does not involve mathematical steps like derivatives or integrations. Unlike suggested in [15], usage of low-pass filters is not required since the ripples in the back-EMF waveforms are mitigated by utilizing PWM switches (IGBTs) with Snubbers. The filters would otherwise introduce some considerable delay and therefore would require some compensation. Moreover, the effect of delays introduced in sample and hold circuits is compensated while introducing the 30-degree delay in switching (commutation) instant of a phase current, being measured from the zero-crossing instant of the back-EMF of the respective phase.

The paper is organized as follows. Section 2 illustrates the proposed sensor-less commutation strategy. Section 3 presents the MATLAB Simulink model of the proposed system. In Section 4, simulation results are presented with their interpretation to validate the proposal. Finally, conclusions are drawn regarding the effectiveness and future scope of the model in Section 5.

2. Proposed Sensor-less Commutation Method

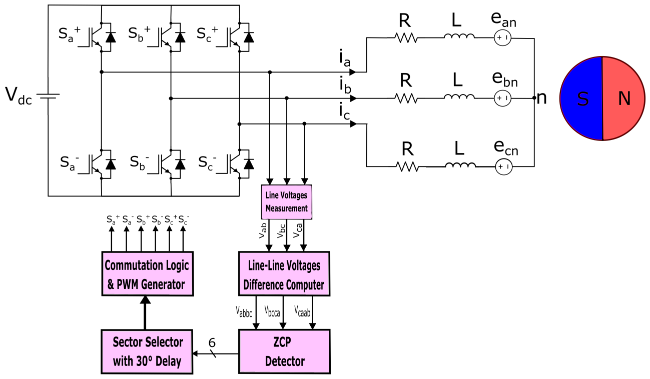

Figure 1: Schematic of proposed sensor-less commutation of BLDC motor drive

Schematic of the proposed model is shown in Figure 1. The BLDC motor being considered has a three-phase star-connected stator winding with permanent magnets mounted on the rotor that can generate an ideal trapezoidal back-EMF. It is driven through a 3-phase inverter (120° conduction mode operation) in which the switches are triggered based on the pulses derived from the commutation logic. In position sensor-equipped motors, the commutation logic typically receives 3 signals from the Hall sensors that have encoded rotor position information. However, the proposed back-EMF zero-crossing estimation method involves the measurement of terminal line voltages, followed by the calculation of their differences and detection of their ZCPs to decode the current sector where the rotor is lying. This information is used to generate appropriate switching pulses through the commutation logic for the next sector where the rotor should be positioned. These switching pulses decide the switching states of the inverter. The process is continuous and ensures smooth rotation of the motor without the need for position sensors. Figure 2 shows the segmentation of the circular path described by the rotor useful in its position detection. Figure 3 shows the ideal back-EMFs waveforms, current waveforms and switching states based on the clockwise angular displacement of the rotor.

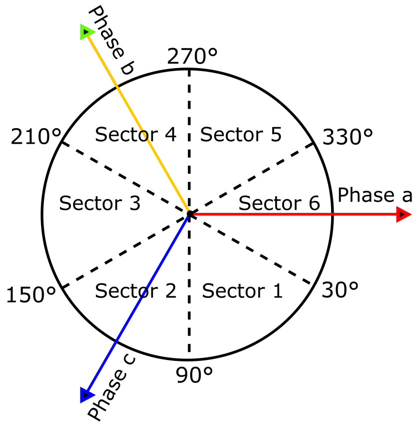

Figure 2: Segmentation of the circular path described by rotor

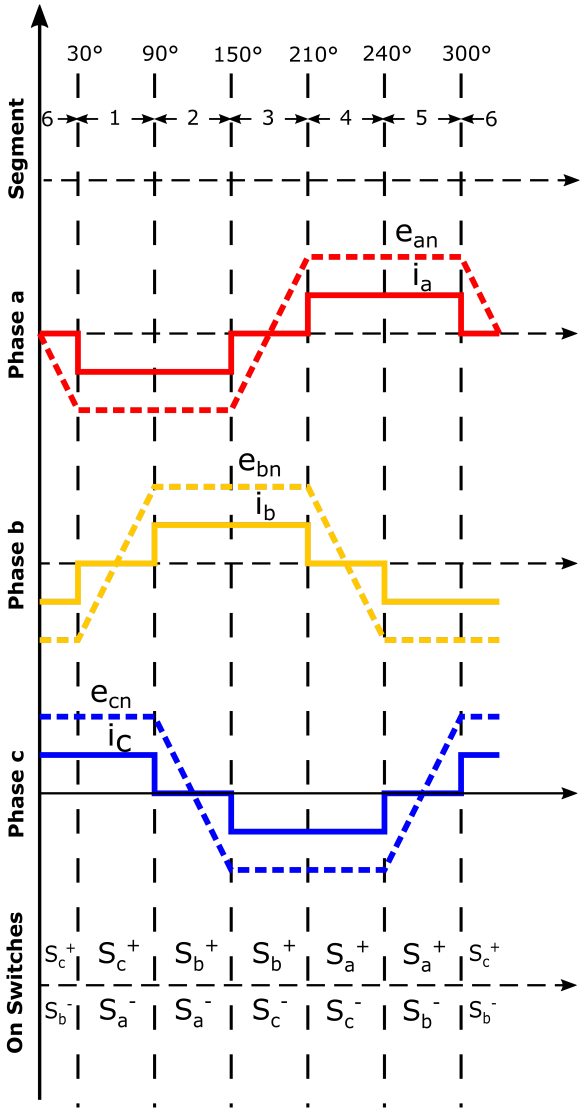

Figure 3: Ideal current and back-EMF waveforms

From the equivalent circuit of the stator windings shown in Fig. 1, the stator phase voltage equations can be expressed as

$$\begin{bmatrix} v_{an} \\ v_{bn} \\ v_{cn} \end{bmatrix} = \begin{bmatrix} R & 0 & 0 \\ 0 & R & 0 \\ 0 & 0 & R \end{bmatrix} \begin{bmatrix} i_a \\ i_b \\ i_c \end{bmatrix} + \begin{bmatrix} L & 0 & 0 \\ 0 & L & 0 \\ 0 & 0 & L \end{bmatrix} \frac{d}{dt} \begin{bmatrix} i_a \\ i_b \\ i_c \end{bmatrix} + \begin{bmatrix} e_{an} \\ e_{bn} \\ e_{cn} \end{bmatrix} \quad (1)$$

where, v_{an}, v_{bn} and v_{cn} are the three-phase to neutral voltages, i_a, i_b and i_c are the stator phase currents, e_{an}, e_{bn} and e_{cn} are the phase to neutral back-EMFs, R is the stator phase resistance and L is the phase inductance. Using equation 1 and subtracting v_{bn} from v_{an}, v_{cn} from v_{bn} and v_{an} from v_{cn} gives the following line voltage equations:

$$v_{ab} = v_{an} - v_{bn} = R(i_a - i_b) + L\frac{d(i_a - i_b)}{dt} + e_{an} - e_{bn} \quad (2)$$

$$v_{bc} = v_{bn} - v_{cn} = R(i_b - i_c) + L\frac{d(i_b - i_c)}{dt} + e_{bn} - e_{cn} \quad (3)$$

$$v_{ca} = v_{cn} - v_{an} = R(i_c - i_a) + L\frac{d(i_c - i_a)}{dt} + e_{cn} - e_{an} \quad (4)$$

Subtracting equation 3 from equation 2, equation 4 from equation 3 and equation 2 from equation 4, yields the following equations:

$$\begin{aligned} v_{abbc} &= v_{ab} - v_{bc} \\ &= R(i_a - 2i_b + i_c) + L\frac{d(i_a - 2i_b + i_c)}{dt} + e_{an} - 2e_{bn} + e_{cn} \end{aligned} \quad (5)$$

$$\begin{aligned} v_{bcca} &= v_{bc} - v_{ca} \\ &= R(i_b - 2i_c + i_a) + L\frac{d(i_b - 2i_c + i_a)}{dt} + e_{bn} - 2e_{cn} + e_{an} \end{aligned} \quad (6)$$

$$\begin{aligned} v_{caab} &= v_{ca} - v_{ab} \\ &= R(i_c - 2i_a + i_b) + L\frac{d(i_c - 2i_a + i_b)}{dt} + e_{cn} - 2e_{an} + e_{bn} \end{aligned} \quad (7)$$

Consider the time interval throughout which the rotor lies in sector 6. From Figure 3, it can be observed that during this time interval, $e_{bn} = -e_{cn}$, $i_b = -i_c$ and $i_a = 0$ while e_{an} transitions from a negative value to a positive value crossing zero. This condition occurs when phase c is connected to the positive terminal of the DC source, and phase b is connected to the negative terminal of the DC source while phase a is open. Thus, when the rotor is in sector 6, equation 7 can be reduced to equation 8 as

$$v_{caab} = -2e_{an}, \quad for\ \theta \in\ Sector\ 6\ and\ Sector\ 3 \quad (8)$$

The condition described by equation 8 also holds when the rotor lies in the sector 3. However, during this time interval, e_{an} transitions from a positive value to a negative value crossing zero as connections to phases b and c are reversed. Similarly, equation 5 can be reduced to 9 when the rotor lies in sectors 1 and 4. Also, equation 6 can be reduced to equation 10 when the rotor lies in sectors 2 and 5.

$$v_{abbc} = -2e_{bn}, \quad for\,\theta \in \; Sector\; 1\; and\; Sector\; 4 \tag{9}$$

$$v_{caab} = -2e_{an}, \quad for\,\theta \in \; Sector\; 2\; and\; Sector\; 5 \tag{10}$$

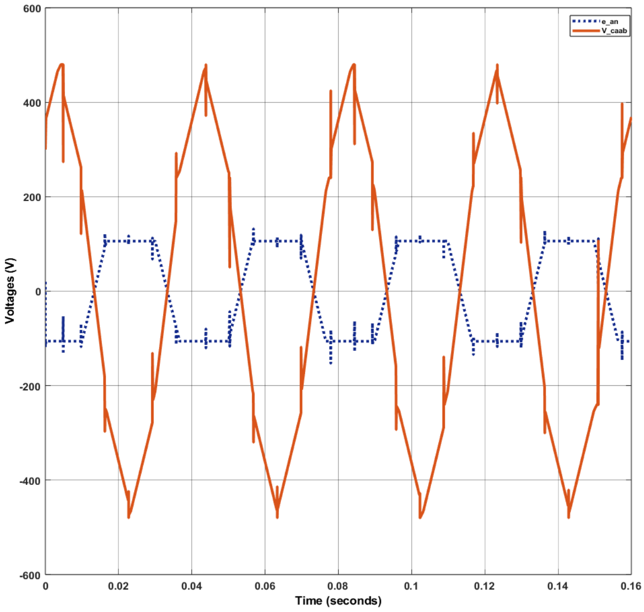

Figure 4: Line-line voltage difference V_{caab} and back-EMF e_{an}

Therefore, the back-EMF waveform of each phase crosses zero twice in an electrical cycle. Further, from equations 8 - 10, it can be concluded that during the commutation intervals, the line-to-line voltage difference is of the opposite polarity to the corresponding back-EMF undergoing transitions and is scaled by a factor of 2. These relations have been validated using the waveforms of v_{caab} and e_{an} as presented in Figure 4 and are applied afterwards to accurately decide the rotor position and generate appropriate switching signals. Table 1 presents the future rotor position information in terms of sectors based on the zero-crossing detection of line-line voltage differences and the corresponding switching states to be applied after a 30° electrical interval. The symbols ↑ and ↓ are used to denote the zero-crossings when a line-line voltage difference transitions from negative to positive polarity (positive zero-crossing) and from positive to negative polarity (negative zero-crossing) respectively.

Table 1: Rotor position estimation and switching states

Zero-crossing line-line voltage difference	Next Rotor Position (after 30° delay)	Switches to turn on next (after 30° delay)
v_{caab} (↓)	Sector 1	S_c^+, S_a^-
v_{abbc} (↑)	Sector 2	S_b^+, S_a^-
v_{bcca} (↓)	Sector 3	S_b^+, S_c^-
v_{caab} (↑)	Sector 4	S_a^+, S_c^-
v_{abbc} (↓)	Sector 5	S_a^+, S_b^-
v_{bcca} (↑)	Sector 6	S_c^+, S_b^-

3. Simulations

Table 2: BLDC motor specification

Parameters	Values
Number of phases	3
Number of poles	2
Rated Voltage	240 V
Rated Speed	1500 rpm
Rated Torque	15.9 Nm
Stator Resistance	1.2 Ω
Stator Inductance	8.5 mH
Moment of Inertia	0.08 kgm^2
Damping Coefficient	0.001 Nms/rad
Back-EMF constant	1.3468 Vs/rad

A 240 V, 2.5 kW, 1500 rpm BLDC motor is selected for simulating the proposed model. Other parameters of the selected motor are mentioned in Table 2. Figure 5 and Figure 6 show the MATLAB Simulink model of the proposed scheme. The line terminal voltages are measured and their differences are sampled and fed to the zero-crossing detectors. Each zero-crossing detector senses the zero-crossing points (positive and negative) and generates pulses. Each of the six different zero crossing points is uniquely associated with a sector that defines the current and next (after 30°) rotor positions. Based on the next rotor position defined by the sector selector block and according to Table 1, the pulse generator generates the required switching pulses. These switching pulses serve as PWM pulses to drive the inverter.

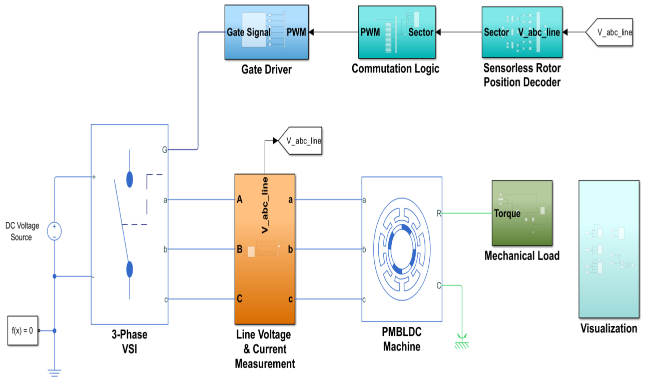

Figure 5: Simulink model of the overall system

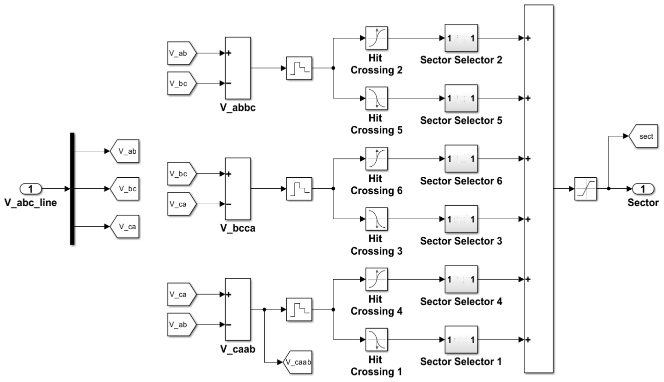

Figure 6: Simulink model of ZCP detector and sector selector

4. Results

The steady-state electrical and mechanical characteristics of the motor at full load speed of 1500 rpm (rated conditions) are studied and validated through simulation results. Under electrical characteristics, phase/line currents and line-line voltages are observed whereas under mechanical characteristics motor torque (τ) and angular speed (ω) are examined.

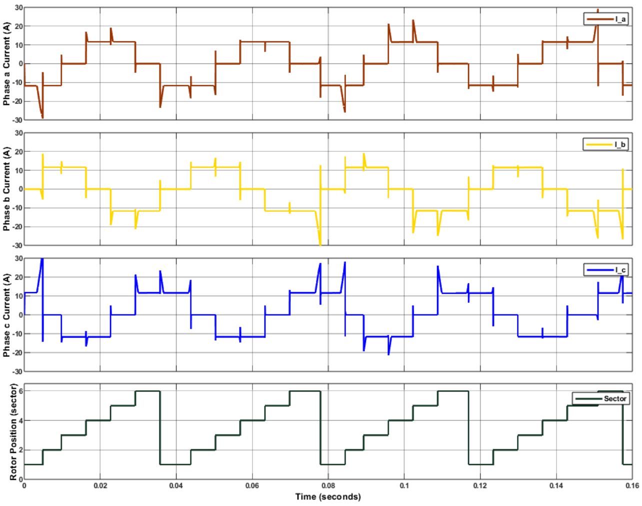

Figure 7: Commutation of motor (phase currents and rotor position)

Figure 7 shows the phase current waveforms of three phases and rotor positions in terms of sector number at different time intervals for a total time duration of 0.16 seconds (4 cycles). The phase currents roughly take the quasi-square wave shape and are mutually displaced by 120° electrical. The ripple contents in the current which depend on stator resistance, inductance and switching frequency, are dominant during the commutation (or phase switching) instants. The figure shows that the phases are being switched in a sequence at the mid-point of every sector, resulting in a successful commutation. The time gaps corresponding to every sector are uniform implying a constant rotor speed. At rated speed, the motor draws an average source current of 11.8 A which is evident from the flat-topped region of the current waveforms.

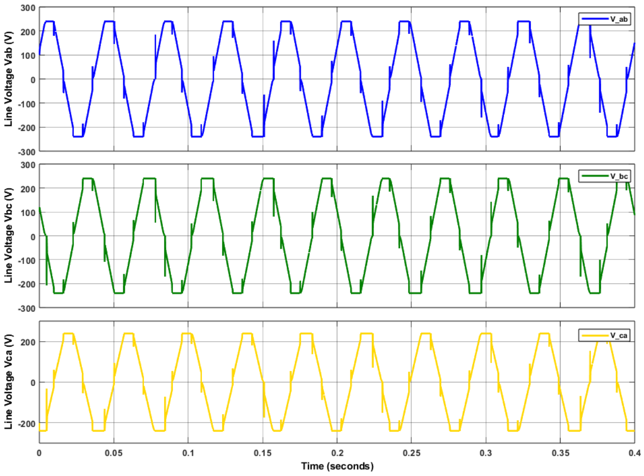

Figure 8: Motor line voltages

Figure 8 presents the waveforms of line voltages V_{ab}, V_{bc} and V_{ca}, for a total time duration of 0.4 seconds (10 cycles) which are used in the detection of ZCPs of the back-EMFs. The shape of the line voltages is roughly trapezoidal as expected with a peak value of 240 V same as the magnitude of the DC voltage source used. This is because any two out of three phases keep conducting together for a duration of 60° electrical. In this duration, full DC bus voltage appears across those two phases thus resulting in a flat-topped region in the wave shape for a 60° interval.

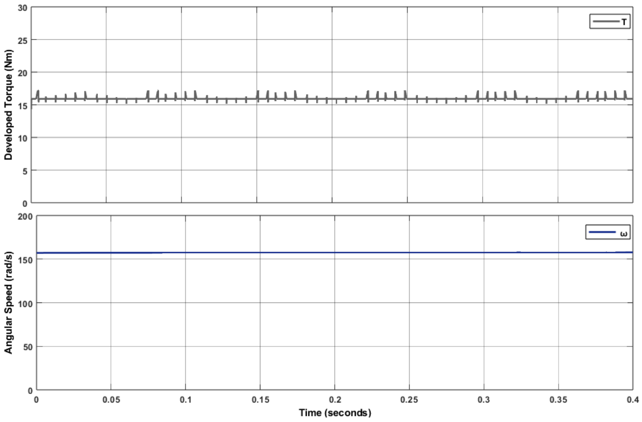

Figure 9: Motor torque and speed at steady state

It is evident from from Figure 9 that the motor is being operated at approximately 1500 rpm (157.08 rad/s) meeting the full load (rated) torque requirement of 15.9 Nm. The ripple in the torque is due to ripples in the current since the torque developed is directly proportional to the phase current magnitude. For a high inertia motor, the ripple in the torque is not a problematic issue since it does not affect the speed much and thus has very little contribution to vibration and noise. However, for a low inertia motor used especially in position control, ripples in the torque may be a critical issue to address. The speed and torque characteristics confirm a smooth and stable operation which is only possible due to successful commutation .

5. Conclusion

A position sensor-less commutation strategy is proposed that relies on the measurement of only line terminal voltages without the need for stator neutral potential. The method proposed does not use any low pass filters as the ripples in back-EMFs and currents are mitigated using inverters that employ switches with Snubbers. Therefore, the need for compensating delays in sensing the ZCPs that could have been introduced due to dedicated low-pass filters is omitted. The proposal has been validated through simulation in a much easier way without relying on mathematical steps such as integrations and derivatives. The results show that the motor runs smoothly with the position sensors being replaced by sensor-less commutation strategy depending on zero crossing detection of line-line voltage differences. Future work will involve the practical implementation of the proposed scheme and its applications in dynamic conditions with varying loads.

References

[1] Jianwen Shao. An improved microcontroller-based sensorless brushless dc (bldc) motor drive for automotive applications. *IEEE Transactions on industry applications*, 42(5):1216–1221, 2006.

[2] Pooya Alaeinovin and Juri Jatskevich. Hall-sensor signals filtering for improved operation of brushless dc motors. In *2011 IEEE International Symposium on Industrial Electronics*, pages 613–618. IEEE, 2011.

[3] Gui-Jia Su and John W McKeever. Low-cost sensorless control of brushless dc motors with improved speed range. *IEEE Transactions on power electronics*, 19(2):296–302, 2004.

[4] Paul C Krause, Oleg Wasynczuk, and Steven D Pekarek. *Electromechanical motion devices*, volume 90. John Wiley & Sons, 2012.

[5] Boyang Hu, Swamidoss Sathiakumar, and Yash Shrivastava. Sensorless drive of brushless dc motor with 180-degree commutation. In *2009 ISECS International Colloquium on Computing, Communication, Control, and Management*, volume 2, pages 579–582. IEEE, 2009.

[6] Jinhe Zhou, Jia Lu, Seyyedmilad Ebrahimi, and Juri Jatskevich. A compensation of commutation angle in hall-sensor-controlled brushless dc motors for maximum torque per ampere operation. In *2022 21st International Symposium INFOTEH-JAHORINA (INFOTEH)*, pages 1–6. IEEE, 2022.

[7] Kenichi Iizuka, Hideo Uzuhashi, Minoru Kano, Tsunehiro Endo, and Katsuo Mohri. Microcomputer control for sensorless brushless motor. *IEEE Transactions on Industry Applications*, (3):595–601, 1985.

[8] Jianwen Shao, Dennis Nolan, Maxime Teissier, and David Swanson. A novel microcontroller-based sensorless brushless dc (bldc) motor drive for automotive fuel pumps. *IEEE Transactions on Industry Applications*, 39(6):1734–1740, 2003.

[9] Tae-Hyung Kim and Mehrdad Ehsani. Sensorless control of the bldc motors from near-zero to high speeds. *IEEE Transactions on power electronics*, 19(6):1635–1645, 2004.

[10] RC Becerra, TM Jahns, and Mehrdad Ehsani. Four-quadrant sensorless brushless ecm drive. In *[Proceedings] APEC'91: Sixth Annual Applied Power Electronics Conference and Exhibition*, pages 202–209. IEEE, 1991.

[11] Satoshi Ogasawara and Hirofumi Akagi. An approach to position sensorless drive for brushless dc motors. *IEEE transactions on industry applications*, 27(5):928–933, 1991.

[12] JX Shen and S Iwasaki. Sensorless control of ultrahigh-speed pm brushless motor using pll and third harmonic back emf. *IEEE Transactions on Industrial Electronics*, 53(2):421–428, 2006.

[13] JX Shen, ZQ Zhu, and David Howe. Sensorless flux-weakening control of permanent-magnet brushless machines using third harmonic back emf. *IEEE Transactions on Industry Applications*, 40(6):1629–1636, 2004.

[14] Bozo Terzic and Martin Jadric. Design and implementation of the extended kalman filter for the speed and rotor position estimation of brushless dc motor. *IEEE Transactions on Industrial Electronics*, 48(6):1065–1073, 2001.

[15] P Damodharan and Krishna Vasudevan. Sensorless brushless dc motor drive based on the zero-crossing detection of back electromotive force (emf) from the line voltage difference. *IEEE Transactions on Energy Conversion*, 25(3):661–668, 2010.

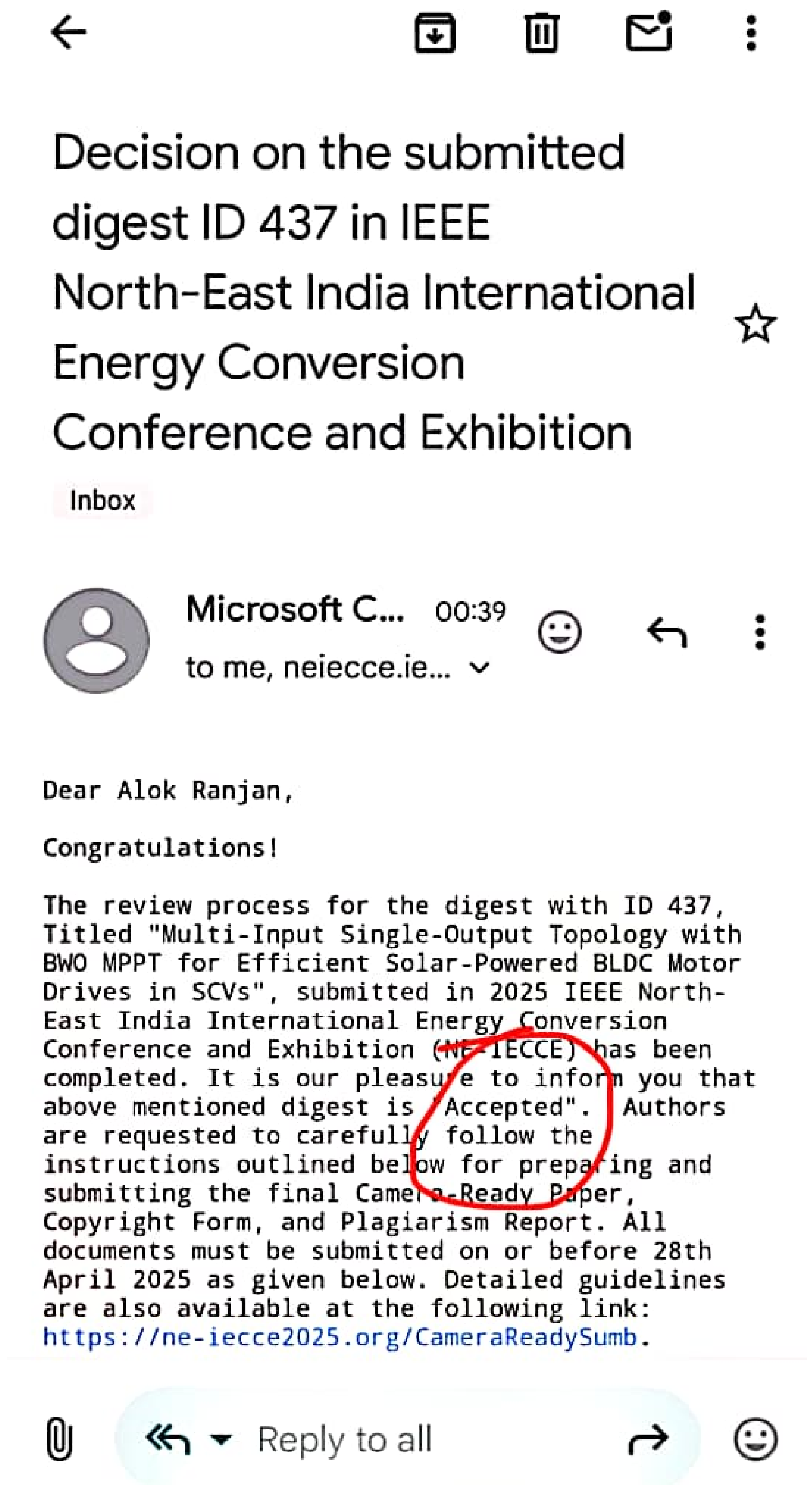

Decision on the submitted digest ID 437 in IEEE North-East India International Energy Conversion Conference and Exhibition

Microsoft C... 00:39
to me, neiecce.ie...

Dear Alok Ranjan,

Congratulations!

The review process for the digest with ID 437, Titled "Multi-Input Single-Output Topology with BWO MPPT for Efficient Solar-Powered BLDC Motor Drives in SCVs", submitted in 2025 IEEE North-East India International Energy Conversion Conference and Exhibition (NE-IECCE) has been completed. It is our pleasure to inform you that above mentioned digest is "Accepted". Authors are requested to carefully follow the instructions outlined below for preparing and submitting the final Camera-Ready Paper, Copyright Form, and Plagiarism Report. All documents must be submitted on or before 28th April 2025 as given below. Detailed guidelines are also available at the following link: https://ne-iecce2025.org/CameraReadySumb.

Gmail

Aashish <aashishacharya555@gmail.com>

[IOEGC16] Editor Decision

1 message

Suwarna Lingden <conference-noreply@ioe.edu.np> 29 March 2025 at 16:32
To: Aashish Acharya <aashishacharya555@gmail.com>, Jeetendra Chaudhary <jeetendra@ioe.edu.np>,
Madhusudan Nyaupane <nyaupanemadhusudan.hr@gmail.com>

Aashish Acharya, Jeetendra Chaudhary, Madhusudan Nyaupane:

We are pleased to inform you that your manuscript titled "Sensor-less Commutation of Brushless DC Motor Based on Zero- Crossing Detection of Line Voltage Differences " submitted to 16th IOE Graduate Conference is **Accepted** for presentation in the Conference as well as inclusion in the Peer-Reviewed Proceedings. Please note that inclusion in hard copy proceedings is contingent upon your timely response to further edits, if any, during the publication process.

With Warm Regards,
IOEGC-16 Editorial Team